UNIVERSITÀ DEGLI STUDI DI GENOVA

Department of Informatics, Bioengineering, Robotics and Systems Engineering

Biopolymeric microbeads as a 3D scaffold for soft tissue engineering

Doctoral Dissertation of:

Donatella Di Lisa

Supervisor: **Professor Laura Pastorino**

XXXII Cycle

This thesis is focused on the fabrication and characterization of biopolymeric microbeads and on their application in the field of micro-engineered soft tissues. The development of techniques to create and use micro-structured hydrogels (granular hydrogels) has enabled the generation of cell cultures with an in vivo like architecture. Specifically, the work has been focused on in vitro models of central nervous system (CNS). Chapter 1 describes the transition from 2D to 3D in vitro models, underlining the importance of 2D model as a gold standard for many patophysiological studies, and pointing out the advantages of a 3D model in order to better mimic the in vivo tissue. In particular, different techniques to fabricate microbeads and the advantages that make them well suited for clinical application are reported in this chapter. A detailed description of the brain extracellular matrix, the model of the development of a neuronal cell in a 2D standard culture and the importance to develop a 3D neuronal model, are provided in Chapter 2. In Chapter 3 it has been demonstrated that Chitosan possesses excellent processability, film forming properties and more importantly bioactivity towards all neuronal populations. In Chapter 4 the fabrication of chitosan microbeads by dripping technique, and their use to create a soft 3D scaffold able to support the development of a neuronal network with an in vivo like morphological and electrophysiological activities, is described. To validate chitosan microbeads as a proper candidate in tissue engineering of CNS, the degradation of chitosan microbeads-based scaffold coupled with neuronal cells was carried out and reported in Chapter 5. An alternative microbeads fabrication method, based on microfluidic approach, is provided in Chapter 6; in this chapter, an innovative method to convert protein-based GelMA microbeads into powders is described. This approach allowed to preserve physical and chemical properties of macromolecules, decreasing contamination, facilitating the shipment and decreasing processing energy and cost. On the overall, this thesis highlights that biopolymeric microbeads represent a great opportunity to create 3D hydrogel-based scaffold which support different types of cell cultures with more biological functionality and architecture, as concluded in chapter 8.

ABSTRACT

The increase of different types of cell cultures, which can be used for the *in vitro* studies of physiological and/or pathological processes, has introduced the need to improve culture techniques through the use of materials and culture media that promote growth, recreating a cellular micro-environment that can be asserted in *in vivo* condition. Therefore, it is important to design and develop new biologically sustainable methods, such as to contribute to the "closer-to-in vivo" condition.

In particular, the design of a 3D i*n vitro* model of neuronal culture is an important step to better understand the mechanisms of cell-cell communication, synaptogenesis and neurophysiological circuits. In order to mimic the ECM environment, a granular, porous and soft structure is preferred in the design of an artificial neural network. The granular structure is preferred due to the fact that CNS tissue seems to be organized as a greater proportion of the microscale tissue, that can be thought of as granular. For this reason, the thesis is focused on the production and characterization of bipolymeric microbeads as a 3D scaffold for soft tissue engineering.

The biopolymer Chitosan is presented as an alternative adhesion factor and support for 2D and 3D neuronal cell cultures. Chitosan is a copolymer of glucosamine and N-acetyl-glucosamine, obtained by the deacetylation of chitin; it is well known for its low-cost, biocompatibility, biodegradability, muco-adhesiveness, antibacterial activity as well as its bioaffinity. Chitosan backbone shows positive charges of primary ammines that favor the electrostatic interactions with the negatively charged cell membranes promoting cell adhesion and growth.

The standard studies focoused on the development of nervous system, have been performed using traditional monolayer culture onto supports modified by extracellular matrix components or synthetic biopolymers such as poly-ornithine and poly-lysine which are expressed at stages critical for neuronal differentiation in situ and are functional in neurite outgrowth *in vitro*, acting as adhesion proteins. Morphological and functional characterization of 2D neuronal culture grew up onto chitosan susbtrates

are carried out and compared with the gold standard reported in literature, in order to validate the ability of chitosan to support neuronal adhesion, networks development and the differentiation capacity. 3D cultured neurons on chitosan microbeads based-scaffold, showed a structural development of a functional network that are more representative of the *in vivo* environment. The studies reported in this thesis, successfully demonstrate the alternative use of the polysaccharide chitosan as adhesion factor and as a structural component for 2D/3D neuronal cultures. Definitely, thanks to its low cost and versatility, it could be easily functionalized for the fabrication of personalized of *in vitro* models.

In this thesis, a new technology to converts monodisperse microbead hydrogels to fine powders, is reported. Microengineered emulsion-to-powder (MEtoP) technology generates microgels with all the molecular, colloidal, and bulk characteristics of fresh microbeas upon resuspension in aqueous media. GelMA microbeads are fabricated by microfluidic technique, that is one of the most effective techniques, and allows precise tuning of the compositions and geometrical characteristics of microbeads.
Gelatin-methacryloyl (GelMA) is a semi-synthetic hydrogel which consists of gelatin derivatized with methacrylamide and methacrylate groups. These hydrogels provide cells with an optimal biological environment (e.g., RGD motifs for adhesion) and can be quickly photo-crosslinked, which provide shape fidelity and stability at physiological temperature.

MEtoP technology is based on protecting the dispersed phase of an emulsion to preserve its physical and chemical cues during harsh freezing and lyophilization procedures. This technology avoids the persistent problems of colloids, including difficulty in sterilization, bacterial and viral contamination, impaired stability, high processing costs, and difficult packaging and transportation.

Table of Contents

Chapter 1 *In vitro* model …………………………………………………………..…..1

1.1 Importance of *in vitro* models …………………………………………………….…2

1.2 From 2D to 3D *in vitro* models ……………………………………………..…….5

1.3 Hydrogel scaffolds ……………………………………………………….....…..8

1.4 Microbeads-based scaffolds ……………………………………………..…....10

1.5 Fabrication Methods ……………………………………………………………21

Chapter 2 Biomimicking the Extracellular Matrix of Central Nervous System ……….31

2.1 Extracellular matrix of soft tissues ………….………………….………………..……..32

2.2 CNS - extracellular matrix ………….…………………….………………….…….…..…35

2.3 *In vitro* models of CNS ………….……………….………………….…………..…...43

2.4 2D neuronal network ………….……………….………………….…………...…..44

2.5 3D neuronal network – microbeads ………….………………….………….……..…47

Chapter 3 Chitosan as adhesion factor for 2D neuronal networks …..………………..…….52

2.6 Bioactivity of chitosan ………….…………….……………….……………………..53

2.7 Aims ………….……………….………………….……………………………..55

2.8 Materials and Methods ………….……………….………………….……………..56

2.9 Results ………….……………….………………..……………………………...64

2.10 Discussion ………….……………….………………….………………………....79

2.11 Conclusion …………………………………………………………………83

Chapter 4 Chitosan– based microbead scaffold for 3D neuronal networks.……...84

4.1 Chitosan microbead scaffolds ……………………………………………...85

4.2 Aims …………………………………………………………………………..85

4.3 Materials and methods ………………………………………………………..86

4.4 Results ………………………………………………………..........................96

4.5 Discussion ……………………………………………………......................107

4.6 Conclusions …………………………………………………...................111

Chapter 5 Chitosan– based microbead scaffold enzymatic degradation …………112

5.1 Biodegradation of chitosan ………………………………………………….113

5.2 Aims ……………………………………………………..............................119

5.3 Materials and methods ……………………………………………………....120

5.4 Results ……………………………………………………............................121

5.5 Discussion ……………………………………………………......................126

5.6 Conclusion ……………………………………………………....................129

Chapter 6 GelMA-based microbead scaffold with tunable mechanical characteristics for different soft tissue models ……………………………………………..130

6.1 Granular hydrogel scaffold ………………………………………………….131

6.2 Aims ……………………………………………………..............................132

6.3 Materials and methods ……….……………….…………………………………........132

6.4 Results ……….……………….…………………………………................................138

6.5 Conclusions ……….……………….…………………………………..........................147

Chapter 7 General Conclusion ……….……………….…………………………………..........149

Chapter 8 Bibliography ……….……………….…………………………………......................152

List of Publications ……….……………….…………………………………...................................180

List of Figures

Figure 1.1 *(A) 2D cell culture, (B) 3D cell culture (Reprinted from Baker, B. M. & Chen, C. S [46]).*

Figure 1.2 *Different droplet production processes by dripping, spraying and microfluidic device. Simple dripping, electrostatic extrusion, coaxial flow, vibrating nozzle, jet cutting and spinning disk (Reprinted from Munmaya M. 2015 [72]).*

Figure 1.3 *Schematic illustration of emulsion techniques in microfluidic devices A) single (W/O), B) double (W/O/W) and C) triple (W/O/W/O) emulsions.*

Figure 1.4 *Schematic illustration of various channel geometries, A) cross-flow, B) co-flow, C) flow-focusing, D) step-emulsification channel arranged with four parallelized drop markers.*

Figure 2.1 *Distinct modulus of human tissues suggesting tissue-specific stiffness. Different tissues with their specific elastic modulus in the body are correlated with their functions (Reprinted from Cox et al., [100]).*

Figure 2.2: *Extracellular matrix in brain. The extracellular matrix (ECM) in the brain is divided into three major components. The basement membrane (basal lamina) which lies around the cerebral vasculature, the perinueonal net which surround neuronal cell bodies and dendrites, and the neural interstitial matrix which are diffusely distributed between cells in the parenchyma. The blue, purple, and yellow cells depict astrocytes, microglia, and neurons, respectively (Reprinted from Kim Y. et al, [103]).*

Figure 2.3 *Perineuronal nets (PNNs). Brain stained with microtubule-associated protein 2 (MAP2) (green) and Wisteria floribunda agglutinin (WFA) (red) (A). Model of PNNs (B). Hypothetical PNN ternary complex of tenascin, chondroitin sulfate proteoglycans (CSPGs) and hyaluronic acid (HA), (Reprinted from Bonneh-Barkay D et al, [101]).*

Figure 2.4 *Major brain proteoglycans. Proteoglycans consists of a protein core decorated with unbranched sulfated glycosaminoglycan sugar chains. CSPG core proteins are decorated with one or more chondroitin sulfate sugar chains. Based on the core protein they are classified into lecticans (which* *includes neurocan, brevican, versican, and aggrecan), phosphacan, and NG2. HSPGs are decorated with HS chains. Syndecans are transmembrane proteins, while glypicans are anchored to the cell membrane with a GPI linkage. Decorin is a secreted proteoglycan with dermatan sulfate side chains (Reprinted from George N et al, [104]).*

Figure 2.5 *Chemical structures of poly-ornithine and poly-lysine.*

Figure 2.6 *Stages of development of hippocampal neurons in culture (Reprinted from Dotti et al, [124]).*

Figure 2.7 *Schematic depiction of the neural environment. (a) Spatial arrangement of the brain tissue compartments (cyan cells = neurons, purple cells = astrocytes, zoom-in subplot: ECM = a net-like cover attached to the surface of neural cells. (b) Enlarged view of the zoom-in subplot of the brain ECM in (a). The net-like cover = hyaluronic acid (HA) secreted by cells acting as a trestle for the ECM net-like structure. The penniform objects crossing the gaps between the HA chains = glycoproteins. Orange triple-circle = tenascin linking glycoproteins up. Multicoloured single circles = components of interstitial fluid (ISF), e.g., water molecules (H2O), extracellular vesicles (EVs), matrix metallopeptidase (MMP), glucose (Glu), dopamine (DA), and tissue plasminogen activators (tPAs). This figure is reused and reprinted from Progress in Neurobiology, Lei and co-workers. (Reprinted from Mahumane G.D. et al, [154]*.

Figure 3.1 *Chemical structure of chitin and chitosan.*

Figure 3.2 *Banker's model, neuronal stages' development from 0 to 7 DIV* (Reprinted from Dotti et al, *[124]*.

Figure 3.3 *Set-up airbrush.*

Figure 3.4 *PLA mask, main parameters of PLA mask to obtain patterned film.*

Figure 3.5 *FT-IR spectra of CHITO samples neutralized in NaOH solution at different molarity, a) pure chitosan (blue), 2% CHITO in NaOH 0.8 M (red), 2% CHITO in NaOH 0.25 M (pink), 2% CHITO in NaOH 0.1 M (yellow). The spectrum of the reference KBr was subtracted from each samples.*

Figure 3.6 *FT-IR spectra of CHITO samples cross-linked with genipin; 1 % CHITO in NaOH 0.25 M (blue), 1% CHITO in NaOH 0.25 M cross-linked in genipin (red). The spectrum of the reference KBr was subtracted from each sample.*

Figure 3.7 *Optical images of 1% CHITO films obtained with different sprayed layers A) 1L, B) 3L, C) 6L and D) 10L; E-F) 1% chitosan-3L onto active area of MEA. Scale bar: 50 µm.*

Figure 3.8 *Optical contrast phase images of 2D neuronal network: (A) 2% CHITO film untreated with a. p. at DIV 15; (B) 2% CHITO film treated with a. p at DIV 15; (C) petri dish untreated with a. p. at DIV 15; (D) 2% CHITO untreated film labeled for Tubulin-bIII (green) and NeuN (red) at DIV 25; Scale bar: 50 µm.*

Figure 3.9 *(A) Neurons grown for 25 DIV on CHITO film marked for the pre-synaptic antibody vs Synapsin (green) and NeuN (red); Scale bar: 20 µm. (B) Neurons grown for 25 DIV on CHITO film marked for vesicular GABA transporter, VGAT (red) and vesicular glutamate transporter, VGLUT (green); Scale bar: 50 µm.*

Figure 3.10 *Optical contrast phase images of 2D films neuronal network at DIV 15, CHITO film untreated with adhesion proteins (a.p.), (left); CHITO-Genipin film untreated with a.p.(middle); CHITO membrane coated with a.p. (right); Scale bar: 50 µm.*

Figure 3.11 *Immunostaining for GFAP and NeuN to distinguish the two different populations. (A) The population of neuron and glia at DIV 3, 7, 15 and 21. (B) Percentage variation of glia vs neurons at DIV 3,7,15,21.*

Figure 3.12 *Optical images of hippocampal neurons at 4h and 24 on CHITO at 0.01% (A-B), 0.05 % (C-D), 0.1 % (E-F), 0.5% (G-H) and on PORN substrate (I-L) Scale bar: 30µm.*

Figure 3.13 *Plating efficiency, n° neurons adhered after 4h and 24h on different CHITO concentrations substrates and poly-ornithine. There is nt signgnificant statistical differences between the two substrates at different time points.*

Figure 3.14 *Stages of neuronal development, A-D) Optical images of hippocampal neurons at 4, 24, 48, 72 hours on spray coating 1% CHITO 1L and onto PORN (E-F). Scale bar: 50µm.*

Figure 3.15 *Time dependence of the effects of substrate-bound chitosan on neurite lengths. Cells were maintained for 4, 24, 48, 72hr in culture, and the length of all neurites of process-bearing cells was measured for neurons on the control substrate (PORN) and on chitosan (CHITO). Results show the number of neurites per cells (A), the average lengths of all neurites (B), the average lengths of major neurites per cell (C), the total lengths of minor neurites (C).*

Figure 3.16 *A-E) Hippocampal culture development on spray-coating chitosan staining for MAP-2 (green) and TAU (red) at 4, 24,72 hours 5 and 7 days in vitro; F-L) hippocampal culture development on PORN staining for MAP-2.*

Figure 3.17 *2D neuronal network on CHITO patterned film, Hippocampal culture development on spray-coating chitosan patterned film staining for MAP-2 (green) and GFAP (red). Scale bar:500 µm.*

Figure 3.18 *(A) Number of active electrodes (hippocampal culture), (B) number of active electrodes (cortical culture), (C) Neuronal culture development on CHITO substrate on MEA staining for MAP 2 (green) and NeuN (red) at DIV 24, scale bar: 20 µm; (D) Comparison of mean firing rate between 2D neuronal networks developed on CHITO and PORN substrates at DIV 22, (E) Comparison of mean bursting rate between 2D neuronal networks developed on CHITO and PORN substrate at DIV 22. (F) Neuronal culture development on CHITO substrate on HD-MEA staining for MAP-2 (green) and NeuN (red) at DIV 24, scale bar: 50 µm.*

Figure 3.19 *Spontaneous activity characterization of hippocampal cultures: (A) Raster plot showing 10 min of spontaneous activity of 2D network on CHITO substrates from DIV 19 to DIV 30.*

Figure 3.20 *Comparison of the effects of substrates, CHITO, PORN and poly-lysine on the length of major neurites.*

Figure 3.21 *Chemical structures of Chitosan, poly-ornithine and poly-lysine.*

Figure 4.21 *Nisco Encapsulation Unit VAR J30.*

Figure 4.22 *Covalent crosslinking of CHITO cross-linked with genipin.*

Figure 4.23 *Set-up configuration, (A) Micro-electrode arrays (MEAs) made up of 60 planar microelectrodes (TiN/SiN, 30 mm electrode diameter, 200 mm spaced) arranged over an 8 X 8 square grid with inserted PDMS (internal diameter 5 mm) constraint on the active area; (B) 3D CHTO scaffold macroscale assembly onto MEA labeled for MAP-2.*

Figure 4.24 *Characterization of CHITO microbeads, (A) Histogram of the distribution of 1% CHITO microbeads size; (B) Histogram of the distribution of 2% CHITO microbeads size; (C) Topography AFM image (second order flattened) of 15 X 15* mm^2 *of a single 2% CHITO microbeads in culture medium, the insert shows the profile of the raw data from a single line (blue line); (D) Stiffness values measured by AFM on 1% and 2% CHITO microbeads.*

Figure 4.25 *Three representative AFM force-distance curves taken on 1%, 2% CHITO microbeads, and a reference hard surface, respectively, using a the same tipless cantilever. Both approach-loading and retract-unloading portions of the curves are plotted (black and red lines, respectively). A rather constant slope in the region after contact can be clearly observed for all curves. The lower slope when pressing against a CHITO microbead indicates that the bead deforms under the applied load. Such deformation can be calculated at any given force as indicated in the graph.*

Figure 4.26 *FE-SEM images, (A) 1% CHITO microbead, scale bar: 20 μm; (B) 2% CHITO microbead, scale bar: 5 μm; (C) CHITO-genipin microbead, scale bar: 10 μm. (D) 1% CHITO microbeads, Scale bar: 100 μm; (E) zoom of 1% microbead surface, Scale bar: 2 μm; (F) 2% CHITO microbeads, Scale bar: 100 μm; (G) zoom of 2% microbead surface, Scale bar: 2 μm.*

Figure 4.27 *Low-mag TEM micrograph of a portion of chitosan scaffold with the neuronal network, (A) CHITO microbeads are marked with the asterisks, while cells appear darker, the dark arrow highlight a glial cell. (B) A neuron grown between two microbeads (1000x). The dark arrows indicate dendrites inside the chitosan. (C) A detail (2500x) of the interface cell-CHITO microbeads. Synapses are marked with the letter s. (D) High-mag (15000x) detail of dendrites taken far (15 mm) from the bead surface.*

Figure 4.28 *Confocal microscope images of 3D neural network at DIV 25: (A) 3D neural network on 2% CHITO microbeads (left), single 2% CHITO microbead surrounded by almost six neurons (middle) and a section of 3D neural network on 2% CHITO microbeads (right), MAP-2 (green) and Synapsin (red). (B) 3D neuronal network on glass microbeads (left), single glass microbead surrounded by five neurons (middle) and a section of 3D neural network on glass microbeads (right), MAP-2 (green and red). The blue arrows point the cell soma while the white one points neuritic fragmentation. (C) 3D neural network on 2% CHITO microbeads (left) labeled for MAP-2 (green), Tubulin βIII (red) and DAPI (blue), 3D neural network on 2% CHITO microbeads (right) labeled for Synapsin (green).*

Figure 4.29 *Optical images of glial cells labeled for GFAP (DIV 25): (A) 2D network on CHITO film; (B) 3D network on 2% CHITO microbeads; (C) 2D network on petri dish. The white arrows point CHITO microbeads.*

Figure 4.30 *Max intensity projection, Orthogonal View and Rendering 3D of population neurons network on the scaffold labeled (DIV 24) for MAP-2: Cross-sectioning along different axes XZ (A), XY(C), YZ (D); (B) Volumetric representation (XYZ) of neuronal networks from the same sample.*

Figure 4.31 *Spontaneous activity characterization, A) 10 s of raw data recorded from a single microelectrode. Raster plot showing 300 s of spontaneous activity of 3D network on (B) CHITO 1% microbeads and(C) on glass bead; (D) mean firing rate, (E) percentage of random spiking activity, (F) mean bursting rate, (G) mean burst duration, (H) network bursting rate, network bursts duration. (Kruskal-Wallis, *p* $< 10^{-3}$*).*

Figure 5.1 *Catalytic action of the chitosanase of subclass I.*

Figure 5.2: *Catalytic action of the chitosanase of subclass II.*

Figura 5.3 *Structure of GH46 (reprinted from Shoko Shinya et al. [215]).*

Figure 5.4 *β-Glucosidase action mechanism.*

Figure 5.5 *Optical images of 2% CHITO microbeads exposed to 25 µl of Chitosanase solution at (0.5 U/ml). A) 0h, B) 6h, C) 24h, D) 48h, E) 6 days. Scale bar: 100 µm.*

Figure 5.6 *Optical images of 2% CHITO microbeads exposed to 25 µl of Chitosanase solution at (1 U/ml). A) 0h, B) 6h, C) 24h, D) 48h, E) 6 days. Scale bar: 100 µm.*

Figure 5.7 *Optical images of 2% CHITO microbeads treated following the first protocol in three different conditions at the last step of the protocol (A) β-glucosidase (50 µl), (B) β-glucosidase (50 µl) + Chitosanases (25 µl), (C) β-glucosidase (25 µl) + Chitosanases (25 µl), at different time points 1) 0h, 2) 6h, 3) 12 h, 4)24 h and 5) 48h h. Scale bar: 100 µm.*

Figure 5.8 *Optical images of 2% CHITO microbeads treated following the first protocol in three different conditions: only β-glucosidase (50 µl), (B) Chitosanases (50 µl) and then β-glucosidase (50 µl), (C)) β-glucosidase (25 µl) + Chitosanases (25 µl), at different time points 1) 0h, 2) 6h, 3) 12 h, 4)24 h, 5) 48h. Scale bar: 100 µm.*

Figure 5.9 *Optical images of 2D neuronal network. A) 2D neuronal culture not exposed to enzymicatic solution; B) 2D neuronal culture immediately after the exposition to the enzymicatic solution; C) 2D neuronal culture exposed to enzymicatic solution after 20 DIV. Scale bar: 50 µm.*

Figure 5.10 *Optical images of 3D neuronal networks on CHITO microbeads based-scaffold exposed to enzymes solutions: A) not exposed to enzymicatic solution, B) 24h after the exposition to the enzymicatic solution, C) 48h the exposition to the enzymicatic solution and D) 72 h the exposition to the enzymicatic solution. Scale bar: 100 µm.*

Figure 5.11 *Time dependence of the effects of Chitosanase and β-Glucosidase solutions on CHITO microbeads. Microbeads were exposed for 12, 24, 48, 72hr and the number of the microbeads not degraded was measured. Results show the effect of 50 µl of chitosanase solution after 24h and 50 µl of* *β-Glucosidase solution after 48h (blue line), 25 µl of chitosanase solutions after 24h and 50 µl of β-Glucosidase solution after 48h (red line), and chitosanase + β-Glucosidase solution after 48h (black line).*

Figure 5.12 *Time dependence of the effects of Chitosanase and β-Glucosidase solutions on CHITO microbeads after 19 in incubator at 37°C. Microbeads were exposed for 12,24, 72hr and the number of the microbeads not degraded was measured. Results show the effect of the only 50 µl of β-Glucosidase solution (pink line), 25 µl of chitosanase + 25 µl of β-Glucosidase solutions after 24h (red line), and 50 µl of β-Glucosidase solution after 24h (blue line).*

Figure 6.1 *MEtoP technology to convert microfluidic-enabled hydrogel particle emulsions to powders. A) parallelized step emulsification device was used for the high-throughput fabrication of GelMA polymer microbeads. B) Procedure to convert emulsion microbeads in powder.*

Figure 6.2 *Comparison between the powders produced via the MEtoP technology and conventional freeze-drying. A) Schematic of individual beads produced via the MEtoP technology compared to those yielded through the conventional freeze-drying. C) The average size of GelMA aerogel beads obtained from the MEtoP technology showing that regardless of polymer concentration (7−20%), the bead size is uniform and depends only on the initial microgel size. SEM images of GelMA beads post conventional lyophilization (D) and MEtoP processing (E).*

Figure 6.3 *Effect of freeze-drying on GelMA microbeads converted to powders via the MEtoP method. Powder GelMA obtained from microgels including (A) 7% w/v, (B) 10% w/v, and (C) 20% w/v of polymer. The freezing process was conducted (1) at -80 °C followed by 5 min of liquid N_2-assisted freezing or (2) without the liquid N_2 freezing step.*

Figure 6.4 *Swelling recovery of beaded GelMA powders produced via the MEtoP technology compared with the conventional method. (A) The swelling time-lapse of powder particles obtained from the MEtoP and conventional methods. (B) The diameter of GelMA beads produced via the MEtoP method undergoing swelling in cold DI water versus incubation time.*

Figure 6.5 *Effect of freeze-drying on the swelling recovery of GelMA microbeads prepared via the MEtoP method. Panels show the rehydration dynamics of powder GelMA obtained from microgels including (A) 7% w/v, (B) 10% w/v, and (C) 20% w/v of polymer. The freezing process was conducted with or without liquid* N_2*-assisted post-freezing.*

Figure 6.6 *Annealing capability of hydrogel beads (GelMA) prepared using the MEtoP technology or conventional lyophilization. (A and C) Optical images of hydrogel beads prepared via the conventional method and MEtoP technology. (B- D) Exposure to UV light in the presence of a photoinitiator (PI).*

Figure 6.7 *Microstructure and mechanical strength of annealed hydrogels obtained from the MEtoP powders. Self-standing hydrogels may readily be constructed by annealing resuspended (A) 7, (B) 10, or (C) 20% GelMA beads, obtained from the METoP technology. Bright-field images of hydrogels in panels A−C are presented in panels D−F, respectively, which show packed structures made up of spherical beads. Two-dimensional (2D) slices of annealed beaded hydrogels obtained from confocal fluorescence microscopy show that regardless of the polymer concentrations (G: 7%, H: 10%, and I: 20%), the beads are able to make microporous structures. Analysis of 2D slices among the annealed beads with GelMA concentrations (J) ~7, (K) 10, and (L) 20%. (M) Median pore diameter of annealed beaded GelMA scaffolds versus pre-UV exposure incubation time. (N) Void space fraction for beaded GelMA scaffolds prepared using varying biopolymer concentration and precross-linking incubation time. (O) The compression moduli of beaded scaffolds. pValues lower than 0.05 (*p < 0.05), 0.01 (**p < 0.01), 0.001 (***p < 0.001), and 0.0001 (****p < 0.0001) indicated statistically significant differences.*

.

Tables

Table 1.1 *Advantages and disadvantages of hydrogels as tissue engineering matrices, Reprinted from Wasupalli G.K., Verma D. Polysaccharides as biomaterials [65].*

Table 2.1 *Extracellular matrix (ECM) components. Abbreviations: PNN = perineuronal net; CSPG = chondroitin sulfate proteoglycan; Abbreviations: PNN = perineuronal net; CSPG = chondroitin sulfate proteoglycan; GAG = glycosaminoglycan; CNS = central nervous system; GPI = glycosyl phosphatidylinositol; HSPG = heparan sulfate proteoglycan; FGF = fibroblast growth factor; VEGF = vascular endothelial growth factor; HB-GAM = heparin-binding growth-associated molecule; bFGF = basic fibroblast growth factor; TGFβ = transforming growth factor β; LTP = long*-term potentiation; *MMP = matrix metalloproteinase; TIMP = tissue inhibitors of metalloproteinase; tPA = tissue plasminogen activator; ADAMTS = A disintegrin and metalloproteinase with thrombospondin motifs; PDGF = platelet-derived growth factor; (Reprinted from Bonneh-Barkay D et al, [14]).*

Table 3.1 *Average growth rate in µm/h.*

Table 3.2 *Average growth rate in µm/d.*

Chapter 1

In vitro models

1.1 Importance of *in vitro* models

Tissue engineering (TE) was defined as “an interdisciplinary field which applies the principles of engineering and life sciences toward the development of biological substitutes that restore, maintain, or improve tissue function” [1]. The aim of TE is design, develop and fabricate an *in vitro* models of healthy or pathological tissues and organs, which can be employed for drug screening and the evaluation of new therapies, as well as the investigation of the complex phenomena regulating disease onset and progression.

The complexity of *in vivo* tissue organization allows cells to interact with each other and with the surrounding extracellular matrix (ECM). The extracellular matrix (ECM) is the non-cellular component of tissues and is comprised of a combination of polysaccharides, growth factors, and proteins including collagen, fibronectin, laminin, and elastin. The physico-chemical characteristics of the ECM play a fundamental role in regulating relevant physiological cellular processes and in different pathological situations [2, 3]. The TE idea is based on the combination of living cells with a natural, synthetic, or bioartificial support to develop a biological substitute or a 3D living construct that is structurally, mechanically, and functionally equal to a real tissue [4]. To date, most *in vitro* functional studies have been performed using oversimplified traditional monolayer cultures. However, in the last few years, a large number of research groups have been focusing on the setting up of cellular models which mimic the *in vivo* microenvironment [5, 6]. This approach has proven to be essential to gain information on pathological processes like cancer, where cell-cell and cell-microenvironment interactions play a major role [7]. The availability of 3D culture platforms, specifically designed to mimic different tissues towards the development of organ-on-a-chip [8], is expected to have a strong impact not only in the study of physiological and pathological processes, but also in drug screening and in toxicity assays [3, 9-13]. There are two different approaches for the design of tissue-engineered *in vitro* models: *top-down* (developmental/regenerative) and *bottom-up* (compartmentalized) approaches. *Top-down* or regenerative approaches involve encapsulation of cells within a substrate and allowing them to spontaneously form structures within the soft substrata in which the cells are able to degrade and reconstruct. Cells are cultured on scaffolds specifically designed to mimic the tissue to be modeled in terms of structure, composition, and mechanical properties. *Bottom-up* is the methodology that include firstly, the design of the scaffolding structure and then seeding it with the cells, adding biochemical components into the preformed structures. That is, all of the factors are assembled into specific spatial coordinates at specific time points. These modular scaffolds can be obtained through both microencapsulation and microfabrication techniques as well as employing traditional cell culture strategies [14]. The model should be properly designed to recapitulate the particular conditions that are intended to be mimicked. Mimic a tissue is extremely complex since several aspects must be taken into account and each single tissue has different features. In this context, the fundamental elements that should be considered are (I) *scaffolds*, (II) *cell sources*, and (III) *chemical and physical stimuli*.

The basic requirements for designing *scaffolds* based on polymeric components are as follows:

1. The surface should permit cell adhesion, promote cell growth, and allow the retention of differentiated cell functions
2. The scaffolds should be biocompatible, neither the polymer nor its degradation by-products should provoke inflammation or toxicity in vivo
3. High porosity with adequate surface area and pore size distribution. This porous architecture allows cells migration also in the inner part of the 3D construct and permits nutrient/oxygen diffusion and waste removal [15]
4. Biodegradability with the rate of degradation corresponding to the rate of neotissue regeneration
5. Reproducibility, the material should be processable into three-dimensional structure and mechanically strong.

The choice of the most appropriate *cell source* is a challenge in the design and further development of a tissue-engineered model. In fact, the development of representative *in vitro* tissue/organ models depends on the availability of tissue-specific cellular phenotypes, able to recapitulate *in vitro* the characteristics of normal or pathological natural tissues. Moreover, the number of cells to be included in the model should be carefully considered to guarantee a physiologically relevant 3D replica of the tissue functional unit [16]. The *in vivo* environment guarantees the presence of fundamental molecular cues that direct cell behavior, while the vascularization provides nutrient supply and waste removal. In the design of a 3D model, it should be considered that cells in the middle of the construct could behave differently from cells growing on the surface, depending on nutrients concentration gradient. During the design and the development of 3D tissue model, the main problem for the diffusive transport of nutrients is the thickness of the 3D structure. To avoid local concentrations and overcome the diffusion limits, that affect cell behavior, chemical, and mechanical signals should be coupled [17]. In particular, cells respond to dynamic cues, such as electric fields, osmotic and hydrostatic pressure, stress, strain, fluid flow, and streaming potential, by modifying the surrounding ECM [18]. Mechanical stimuli are usually provided to tissue-engineered constructs by bioreactors specifically designed to reproduce the *in vivo* conditions. In particular, bioreactors provide mechanical or electrical stimuli and allow a fine modulation of culture conditions to reach tissue maturation [19,20]. The choice of the most suitable biomaterial for scaffold fabrication is a key element for the model design, since it strongly influences cellular functions; should be carefully selected depending on the modeled tissue/organ, acting as a synthetic ECM that interacts with cells at the molecular level, influencing cell functions and driving the complex cellular processes that lead to the development of a valid *in vitro* engineered tissue model. To replicate *in vitro,* the architecture of the native tissue, i.e., its ECM framework to let cells to adhere, spread, proliferate, differentiate, maturate, and produce ECM, similarly to what they do *in vivo.* Natural gels are typically formed of proteins and extracellular matrix (ECM) components, this makes them inherently biocompatible, bioactive, biodegradable, low cytotoxic, injectable and possibly suitable for many biomedical applications as they promote many cellular functions. Naturally derived hydrogels can be classified in 3 groups: *protein-based materials, polysaccharide-based materials*, including collagen, silk fibroin, hyaluronic acid, chitosan, alginate and those derived from *decellularized tissue*. Three-dimensional culture systems for *in vitro* development of tissue, employing a wide range of scaffold types including hydrogels, solid porous polymers, fibrous materials and decellularized tissues as well as microfluidic devices and lab-on-a-chip systems. These different types are prepared by different methods, which makes it more suitable for the application intended for it, including gas foaming, [21,22] fiber extrusion and bonding, [23] three-dimensional printing, [24] phase separation, [25,26] emulsion freeze-drying, [27] and porogen leaching. [28,29], hydrogel microbeads [30,31].

The introduction of these models in the biomedical field may lead to numerous advantages, such as the reduction of animal use as well as the overcoming of the limits associated with traditionally employed models and the achievement of more reproducible data, thanks to the possibility to tightly control the experimental parameters, with lower cost and less time.

1.2 From 2D to 3D *in vitro* models

The culture of mammalian cells *in vitro* provides a defined platform for investigating cell and tissues physiology and pathophysiology. Traditionally, this has been done by culturing single cell populations on two dimensional (2D) substrates. Experiments whit 2D cell cultures have provided the base for the interpretation of complex biological phenomena, including molecular biology, stem cell differentiation [32], and tissue morphogenesis [33]. The majority of 2D approaches employ rigid substrates that do not faithfully represent the deformable matrices observed *in vivo*; in fact, cells in vivo do not spread in the same way as cells cultured on 2D substrates, but cells sense the stiffness of their environment and modify their shape, proliferation, and stiffness in response. *In vivo*, the ECM guides a host of cell and tissue level functions including regulation of cellular architecture [34], directing tissue-specific stem cell specification [35, 36], guiding cell migration [37], maintaining homeostasis [38], and influencing tissue development [39-41], including controlling branching morphogenesis [42,43]. One of the major function of the ECM is to regulate cell shape and its connectivity to surrounding cells which in turn regulates the cellular epigenetic state, gene expression, and function [39,44]. Strategies aimed at a closer approximation of tissue dimensionality involve pseudo-three dimensional (3D) or 2.5D environments, which aims to reduce the artificial polarity of 2D culture while maintaining the ease on the culture manipulation. An example of a pseudo-3D environment is the creation of micro-wells which are topographically structured surfaces that comprise a high density of micron sized cavities of a desirable geometry. They can be created via curing a gel solution, most commonly polydimethylsiloxane (PDMS) or polyethylene glycol (PEG), onto a silicon master [45]. Pseudo-3D platforms are useful for replicating higher order dimensionality to study the transition from 2D to 3D, where true 3D materials are difficult to yield coherent data on cell-cell and cell-ECM interactions. Pseudo-3D systems have proved a viable alternative, and show promise in mapping the differences between 2D and 3D towards translating the large number of 2D studies to 3D materials and *in vivo* systems. While 2D systems can give insight into many cellular functions, the addition of a third dimension enables a closer mimic to the *in vivo* environment. The ECM is a hydrophilic 3D micro-matrix whit two major solid structures: collagen fibers and proteoglycan filaments. The collagen fibers present as bundles and extend through the interstitium, providing the tensile strength and durability for the surrounding tissue. The proteoglycan filaments are coiled structures, made from protein and hyaluronic acid which entrapped interstitial fluid, that is a plasma-like fluid, giving to ECM a gel-like uniformity.

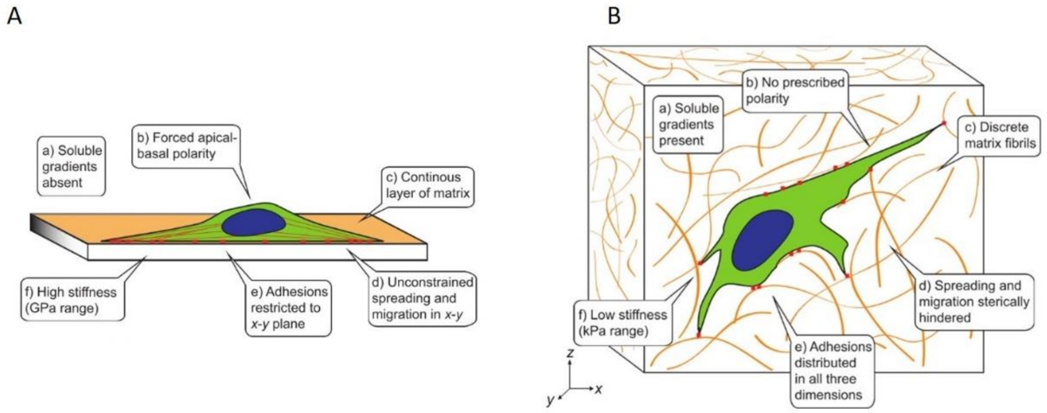
A
a) Soluble gradients absent
b) Forced apical-basal polarity
c) Continous layer of matrix
f) High stiffness (GPa range)
e) Adhesions restricted to x-y plane
d) Unconstrained spreading and migration in x-y
B
b) No prescribed polarity
a) Soluble gradients present
c) Discrete matrix fibrils
d) Spreading and migration sterically hindered
f) Low stiffness (kPa range)
e) Adhesions distributed in all three dimensions
z
y
x

Figure 1.1 *(A) 2D cell culture, (B) 3D cell culture (Reprinted from 46. Baker, B. M. & Chen, C. S [46]).*

Hydrogels scaffold have received a considerable attention due to their unique compositional and structural similarities to the natural ECM. From 2D plastic-ware to 3D hydrogels, model systems have come a long way in controlling the presentation of biochemical and biophysical cues to cells in culture towards elucidating the complex cellular orchestration underlying tissue morphogenesis. The design criteria should include both mechanical and physiochemical parameters (such as biodegradation, porosity and proper surface chemistry), and biological performance parameters (such as biocompatibility and cell adhesion), as well as demonstrating enhanced vascularization.

Biodegradation: a basic requirement of a scaffold for tissue engineering is to maintain cellular proliferation and desired cellular distribution during the life of the scaffold. The rate and extent of biodegradation are critical design considerations for hydrogels in tissue engineering. Some tissue engineering applications may not require complete scaffold degradation, such as whit corneal replacement or articular cartilage. For these types of tissue, semi-permanent or permanent scaffolds may be the best choice to replace the basic function of lost or damaged tissue. In general, degradable hydrogel scaffolds are developed via incorporating cleavable crosslinks and/or cleavable moieties into the polymer backbone. In this case, the degradation is achieved through biological processes, mainly enzymatic digestion. Biodegradable hydrogel scaffolds can also be made by incorporating naturally biodegradable ECM components.

Biocompatibility: the ability of a material to perform with an appropriate host response in a specific application. It means that no or very limited harmful immunological, toxic, or foreign body responses should take place as a results of regenerative medical intervention.

1.2.1 Hydrogel scaffolds

One of the most common forms of 3D culture is to encapsulate cells within hydrogel scaffolds consisting of different ECM proteins or peptides [47-51]. This technique involves the mixing of cells and a liquid gel and allowing the solution to set into the desired shapes. Synthetic polymers are preferred due to the ability to control their physical and chemical properties, but they lack the biological activity of natural polymers [52]. Hydrogels are used as tissue engineering scaffolds typically because their soft, hydrated form resembles that of naturally occurring living tissue. The mechanical properties of hydrogels can be tuned and the high water content and highly porous nature of hydrogels allow for facile transport of oxygen, nutrients and waste as well as effective transport of soluble factors [53]. An additional attraction of hydrogels is their ability to be administered via injection [54]. After injection, they can conform to the available space, allowing for uniform tissue regeneration. However, hydrogels have to be maintained in a hydrated state, therefore could possibly suffer from long term stability issues *in vitro* [55]. The scaffolds designed may contain pores size suited for living cells accommodation or may be regulated to degrade creating pores by releasing growth factors where cell penetrates and proliferates. Using hydrogels to mimic *in vivo* microenvironments has proved useful in deconstructing the biochemical and biophysical cues that influence cellular morphology [56-57], proliferation [57-61], migration [62], and differentiation [63-66]; but despite of this, the inability to control the pore interconnectivity and decoupling it from the matrix stiffness has tremendously limited the applicability of stiff hydrogels for 3D cellular engineering, e.g., in hard tissue engineering. A recent study showed a new concept to convert thermosensitive polymers with chemically-crosslinkable moieties into annealable building blocks, forming 3D microporous beaded scaffolds in a *bottom-up* approach and can be quickly photo-crosslinked, which provides shape fidelity and stability at physiological temperature [67].

ADVANTAGES	**DISADVANTAGES**
Aqueous environment can protect cells and fragile drugs (peptides, proteins, oligonucleotides, DNA)	Can be hard to handle
Good transport of nutrient to cells and products from cells	Usually mechanically weak
May be easily modified with cell adhesion ligands	May be difficult to load drugs and cells and then cross-link
Can be injected in vivo as a liquid that gels at body temperature	*in vitro* as a prefabricated matrix
Usually biocompatible	May be difficult to sterilize

Table 1.1 *Advantages and disadvantages of hydrogels as tissue engineering matrices, Reprinted from Wasupalli G.K., Verma D. Polysaccharides as biomaterials [65].*

Engineered extracellular matrices have proved useful in decoupling the environmental parameters that guide cellular processes, the form and function of tissue. While hydrogels provide excellent scaffolds that mimic the natural ECM, they are limited in scale-up because of long term storage issues, stability and batch-to-batch variability. Highly porous solid scaffolds can be manufactured in a controlled and reproducible fashion, can be appropriately moulded, are inert in structure and have long term stability [66]. The mechanical stability of these scaffolds, along with their high porosity and pore interconnectivity make them ideal for highly interactive 3D cell cultures [52]. In porous scaffolds theoretically, there should be deeper and more uniform nutrient transport and also allows cells to freely migrate throughout the structure without much resistance. The pores themselves can also limit the size of colonies, which when too large can cause cells to become necrotic [52]. The mechanical stability of solid porous scaffolds makes them a more practical material for handling, which is difficult with soft hydrogels. The key limitations of solid scaffolds however are, firstly, they are typically opaque and have poor light transmission properties, making in situ imaging difficult [66]. Secondly, the Young's modulus of many solid porous scaffolds is quite different to that of specific tissue as CNS tissue (0.1–16 kPa) [68] and so these scaffolds may not provide realistic tissue and disease models. An array of techniques has been used to synthesize solid porous scaffolds, including salt leaching, phase separation, freeze drying, gas foaming, emulsion templating and 3D printing [53].

Culturing cells in 3D materials more closely recapitulates the *in vivo* environment, when compared to conventional 2D systems; however, most of these materials only offer a static image of what is otherwise a dynamic and complex environment.

1.3 Microbeads-based scaffolds

Cells in the body exist in a 3D microenvironment comprising of proteins and polysaccharides, which is defined as the extracellular matrix (ECM). The properties of ECM strongly influence cellular phenotype and function. Biocompatible hydrogel microbeads with sizes ranging from 60 to 200 µm are promising platforms for *in vitro* cell culture, as they perform as 3D matrices that can mimic various aspects of the ECM [69,70]. Their properties such as stiffness and porosity can be tuned by altering the gel components. In addition, the intrinsic porous structure and the high surface-to-volume ratio of hydrogel microbeads facilitate exchange of oxygen, nutrients and waste, while protecting the cells from the surrounding environment and retaining cell viability. The function of a tissue is typically governed by multiple cues, such as intercellular signaling and cell interactions with the surrounding ECMs. Cell-laden microgel “modules” carrying different types of cells can be combined or reconfigured to mimic various types of tissues. These applications of microbeads depend on their properties which correlate with their size, structure, composition and configuration. Based on the structural prerequisites, one of the main goal of the production of microbeads is to ensure accurate control over their macroscopic properties (e.g., geometry, mechanical strength, density, porosity) and microstructure (e.g., size, pore interconnection). Microbeads with sizes ranging from 1 μm to 1000 μm have great potential in the fields of drug delivery, cell biology and biosensor**s**; the small size of the hydrogel microbeads is particularly attractive for injectable cell delivery systems in regenerative medicine, as it allows direct delivery of cells through needles to the damaged tissue area [72]. This minimizes surgical invasiveness and thus is beneficial in practical clinical applications such as drug delivery, tissue engineering, biosensing, and cellular life science. Depending on their structure, they can be classified into *microcapsules* and *microspheres.*

Microcapsules: They consist of a central nucleus (containing the drug, in liquid or solid form) surrounded by a polymeric membrane (wall) of coating [73]. There are different configurations:

- *Microcapsules with core-shell structure*: they are typically composed of solid, liquid surrounded by protective shell.
- *Janus microparticles*, they have two separate compartments with distinctive physicochemical properties which make them appealing for drug delivery, micromotors, and self-assembly.
- *Microparticles with complex structure (multi-core, higher order:* The structure of microcapsules can be much more diversified by incorporating an additional compartment in the emulsion droplet, either in the core or the shell. For example, microcapsules with multi-core components are synthesized by using several separate inner flows during emulsification. These inner cores

can be either separated by a solid shell or have a single Janus core within the shell after UV irradiation.

- *Porous microparticles*: they can be prepared by introducing sacrificial templates into the precursor droplet and subsequently removing them after solidification. In addition, phase separation can also be employed to prepare porous microparticles

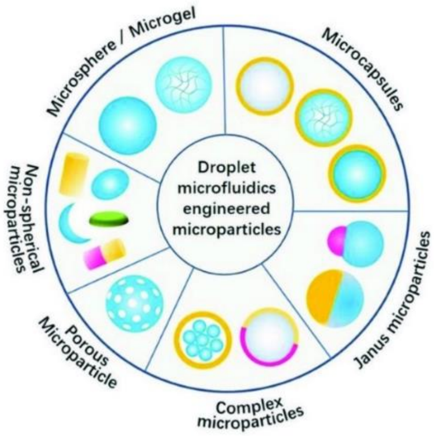
Microsphere / Microgel
Microcapsules
Janus microparticles
Complex microparticles
Porous Microparticle
Non-spherical microparticles
Droplet microfluidics engineered microparticles

Figure 1.2 *Different types of microbeads (Reprinted from Li W et al, 2018, [72]).*

Microspheres: They have a monolithic structure, that is they are constituted by a polymeric matrix.

Microbeads also have a number of specific requirements:

- chemically inert materials
- non-toxic
- sterilizable or not
- chemically and physically stable
- good mechanical strength
- they must not release impurities or polymerization residues

The choice of process to be applied depends on the assessment of a number of factors:

- Nature of the material to be encapsulated, physical state (solid or liquid), hydrophilia/lipophilia, thermal stability or pH dependent.
- Nature of the encapsulation medium: organic or aqueous solvents, gas.
- Structure of the microbeads to be obtained: microspheres, mononucleus microcapsules, multinucleus, etc.
- Economic: cost/benefit ratio, existence of patents, available equipment and/or technology, etc.

In particular, encapsulation can be defined as a process that involves the complete envelopment of preselected core material(s) within a defined porous or impermeable membrane using various techniques. The techniques used vary depending on the polymer used and the appropriate application [72]. The main techniques used in encapsulation can be classified into three main categories such as chemical, physicochemical, and mechanical processes. Chemical processes are those that involving mainly polymerization and polycondensation and in which the capsule shell is made by in situ formed polymers. The disadvantage is the tendency to form very thin polymer membranes. Physico-chemical process involves the formation of the capsule shell form a preformed polymer using processes such as solvent removal, gelatin, or coacervation. Mechanical processes produce the polymer shell around the core using techniques such as spray drying and spray cooling, dripping and jet break-up techniques. In particular, the most important methods for microencapsulation are the *dripping by nozzle*, *spray-drying*, and *microfluidic techniques*.

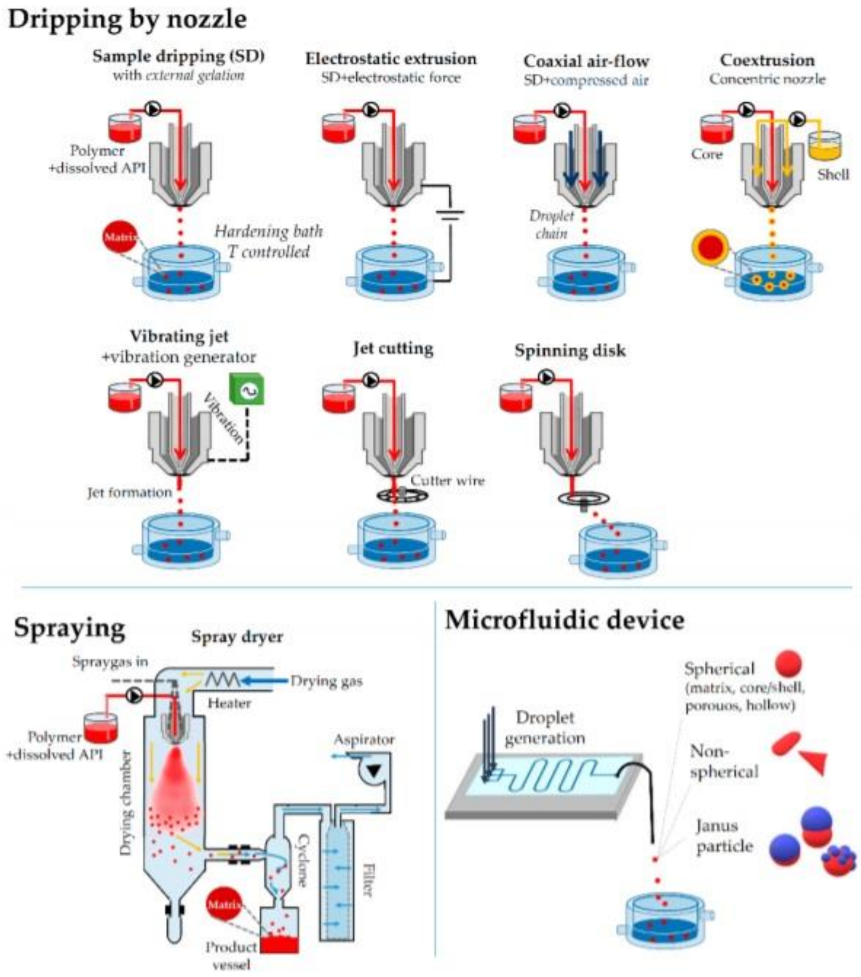
Dripping by nozzle
Sample dripping (SD)
with external gelation
Polymer
+dissolved API
Matrix
Hardening bath
T controlled
Electrostatic extrusion
SD+electrostatic force
Coaxial air-flow
SD+compressed air
Droplet
chain
Coextrusion
Concentric nozzle
Core
Shell
Vibrating jet
+vibration generator
Vibration
Jet formation
Jet cutting
Cutter wire
Spinning disk
Spraying
Spray dryer
Spraygas in
Drying gas
Heater
Polymer
+dissolved API
Aspirator
Drying chamber
Cyclone
Filter
Matrix
Product
vessel
Microfluidic device
Droplet
generation
Spherical
(matrix, core/shell,
porouos, hollow)
Non-
spherical
Janus
particle

Figure 1.3 *Different droplet production processes by dripping, spraying and microfluidic device. Simple dripping, electrostatic extrusion, coaxial flow, vibrating nozzle, jet cutting and spinning disk (Reprinted from Munmaya M. 2015 [72]).*

1.3.1 Dripping by nozzle

The Dripping mode is most widely utilized method due to the high monodispersity of droplets generated. The droplets are generated from a polymer extruded through a nozzle, and mechanical means are used to increase the normal dripping processes at the orifice of the liquid stream break up when it passes through the nozzle. The droplets will then take a spherical shape during falling due the surface tension of the liquid and will be solidified either by a physical or chemical means. In this mode, the size of droplets can be tuned by changing the nozzle size and flow rate of the fluids phases. Other factors influence the formation of microgels: the concentration, feeding rate, and surface tension of the polymer solution, solvent, temperature, and nozzle diameter [74]. The solidification of the formed microgel particles is performed in an additional step. For solidification of the gel, coacervation (either simple or complex) is an optimal choice. The formed particles are collected in a solidification liquid (ionic or polymer solution). The size and shape control of particles is dependent on various factors. The distance, concentration, surface tension of the solidification liquid, and the time of the process have a significance in the particle size and the physical properties of the beads (gel strength, porosity, etc.). The most important limitations of the extrusion are the viscosity of the polymer because of potential blockage of the nozzle; as such, the settings for optimal, narrow particle size distribution, and shape are required. For the scale-up of the process, multiple-nozzle solutions have been presented. In particular, the droplets formation is dependent on the velocity v of the extruded polymeric solution, surface tension, gravitation, impulse and friction force [72]. The extruded solution sticks to the edge of the nozzle until the surface tension is overcome by gravitational force that results in the release of the droplet. This mechanism is well known as "dripping". The diameter of the droplet, d_d formed during this mechanism can be estimated from Equation (1). The balance between the two main force is approximated, the gravitational force is pulling the drop down when the surface tension is holding into the tip at the instant of drop detachment. Moreover, as seen in the Equation (1), size of the droplets produced with this mechanism is dependent on the nozzle diameter.

$$d_d = \sqrt[3]{\frac{6d_n\sigma}{g\rho}} \qquad \textit{Equation 1.1}$$

with

d_d, = diameter of the nozzle
σ = surface tension of the extruded liquid
g = acceleration due to gravity
ρ = density of the fluid

The droplet formation is dependent on the velocity v of the extruded liquid, surface tension, gravitation and impulse. At very low velocity, single droplets are directly formed at the orifice of the nozzle. Increasing the velocity will cause the formation of an uninterrupted laminar jet, which eventually breaks by axial symmetrical vibration and the surface tension. The influence of the parameter can be describing by the dimensionless *Ohnesorge* (Oh) *number* and *Reynolds number* (Re):

$$Re = v d_d \rho / \eta \qquad \textit{Equation 1.2}$$

$$Oh = \eta / (\rho d_d \sigma) \qquad \textit{Equation 1.3}$$

v = velocity of polymeric solution at the point of impact
η = viscosity of the polimeric solution
d_d, = diameter of the nozzle
σ = surface tension of the extruded liquid
ρ = density of the fluid

An increase of flow rate (or Re) of a solution at constant Oh will lead the droplet detachment mechanism to a transit form dipping to jetting. The transition between dripping and jetting is strongly dependent on the viscosity or (Oh) of the solution.

1.3.1.1 Electrostatic extrusion

Electrostatic extrusion is a process that uses electrical forces to overcome the surface tension force ad pull the droplet of the orifice. Two main methods can be used, the dripping mode and the jetting mode. In the dripping mode, a low current is applied on the polymer solution flowing slowly through the nozzle. The electrical force then breaks-up the liquid and monodispersed microspheres between 500-1500 µm are obtained. Smaller beads can be produced by increasing the current and using a smaller orifice, however an increase in the electric current will lead to a broader size distribution of the beads due to splitting of the polymer solution filament into numerous side filament within the intense electric field. Increasing velocity, it will bead formation of a stable jet, and a higher electric current will then be necessary to break the jet into small droplet. This is the jetting mode, in which small monodispersed particles of 1-15 µm can be produced with a high productivity.

1.3.1.2 Vibrating-jet

The vibrating-jet techniques, also called vibrating nozzle or prilling is one of the most widely used techniques to produce microspheres. The technology is based on the principle that the application of a vibration frequency with defined amplitude to the extruded laminar jet will break it into equally sized droplets. The vibrational frequency and the jet velocity are the two main parameters to be determined in order to achieve optimal droplet formation with a given nozzle diameter. Uniform-sized droplets can be obtained with a range of frequencies which depend on the nozzle diameter, the rheology of the fluid and the surfaces tension. The vibration system is theoretically based on liquids with Newtonian fluid dynamics. When droplets are formed by the break-up of a jet by the vibration method, they are often dispersed by a system based on electrostatic repulsion force. Having the droplets flying through on electrostatic field after the break-up will charge them, therefore the droplets do not hit each other during the flight and are distributed over a large surface of the gelation bath, thereby resulting in monodisperse beads. The electrode potential is in the range of 400-1500 V depending on the droplet diameter, the jet velocity, and the geometrical setup.

1.3.1.3 Jet Cutter and Spinning Disk Atomization

The principle of the jet cutter is to form a solid jet by pressing the polymer out of a nozzle and then to cut it into uniform segments using a cutting tool formed of several wires. The segments then form spherical beads due to surface tension, as they fall into the cool medium. The diameter of the resulting droplet is dependent on the number of cutting wires, the number of rotations of the cutting tool, the mass flow rate through the nozzle, and the mass flow depending both on the nozzle diameter and the velocity of the fluid. This method allows the production of beads with a size range of 200 µm up to several millimeters, even when using viscous fluids. However, the main disadvantages of this method are the loss of material occurring during each cut of the liquid jet, knows as the cutting loss, its inability to produce beads smaller than 200 microns and to produce high quantities of beads.

The principle of spinning disk atomization is to distribute a liquid onto a rotating disk which, due to centrifugal forces and wetting ability, disperses into a thin film. The liquid gains in velocity, is transported to the disk rim and is spread into droplets, which are thrown off tangentially from the disk and form a spray. The size of the drops depends essentially on the rotary speed, disk geometry and liquind properties. Once drops are detached, interfacial forces keep the atomized liquid into a spherical shape to minimize the specific surface area. According to their size each drop falls at a different distance from the disk atomization is a technique that can produce monodispersed, homogeneous, and spherical beads, with a narrow size distribution, it can be used different viscosities of liquid solutions and operate under sterile conditions. This method has the advantage to be able to produce a large quantity of beads in a short time and can be scaled-up easily by increasing the flow rate, the disk size and the rotation speed of the disk. However, spinning disk fabrication requires a large surface or volume to collect the produced beads without damaging them and this can create problems with sterilization in the case of cell encapsulation.

Furthermore, to produce small beads, it necessary increase speed; high speeds can cause the disk to vibrate and produce of satellites drops.

1.3.2 Spray drying and spray congealing

Spray drying is widely used in the industry for microencapsulation of volatiles, probiotics, and viable cells. Besides the obvious drawback (high loss, low yield), the numerous advantages make this technology very popular (uniform particle size, all steps carried out in one apparatus, use of organic solvents, the capability of encapsulating heat-labile materials). Depending upon the removal of the solvent or cooling of the solution, the two processes are named spray drying and spray congealing respectively. The polymer is first dissolved in a suitable volatile organic solvent such as dichloromethane, acetone, etc. This dispersion is then atomized in a stream of hot air. The atomization leads to the formation of the small droplets or the fine mist from which the solvent evaporates instantaneously leading the formation of the microspheres in a size range 1-100 μm. Microparticles are separated from the hot air by means of the cyclone separator while the traces of solvent are removed by vacuum drying and as a result, regular shaped, micron-sized, uniform particles are created. The extruded wax particles can be solidified using congealing, which offers a solution for embedding hydrophilic component to perform sustained release via the slow erosion of the wall in the biological medium. Very rapid solvent evaporation, however leads to the formation of porous microparticles.

1.3.3 Microfluidics in Microparticle Fabrication

Microfluidics also presents promising results regarding microparticle production [74]. A wide range of microfluidic devices have been created concerning their various structure, material, and size [72].

Droplet microfluidic provides a unique method for fabrication of monodisperse microparticles whit control over the size, morphology and functionality, in high throughput manner. This technique also allows on-chip encapsulation of various bioactives, such as drugs, cells and other bio-reagents in microparticles whit high efficiency, and even direct co-encapsulation of multi-components. These advanteges make microfluidically engineered microparticles beneficial for various biomedical application including development of innovative delivery vehicles and fundamental studies of cell biology.

1.3.3.1 Droplet generation

An emulsion is a mixture of two immiscible liquids where one liquid is dispersed in an another immiscible liquid. The conventional methods for generating emulsions involve droplet breakup using shear or impact stresses generated by agitation.

Single emulsion technique

The micro particulate carriers of natural polymers i.e. those of proteins and carbohydrates are prepared by single emulsion technique. The natural polymers are dissolved or dispersed in aqueous medium followed by dispersion in non-aqueous medium like oil, **figure 1.4A**. In the next step, the cross linking of the dispersed globule is carried out. The cross linking can be achieved either by means of heat or by using the chemical cross linkers. The chemical cross linking agents used are glutaraldehyde, formaldehyde, acid chloride etc. Heat denaturation is not suitable for thermolabile substances. Chemical cross linking suffers the disadvantage of excessive exposure of active ingredient to chemicals if added at the time of preparation and then subjected to centrifugation, washing, separation. The nature of the surfactants used to stabilize the emulsion phases can greatly influence the size, size distribution, surface morphology, loading, drug release, and bio performance of the final multiparticulate product.

Double emulsion technique

Double emulsion method of microspheres preparation involves the formation of the multiple emulsions or the double emulsion of type w/o/w and is best suited for water soluble drugs, peptides, proteins and the vaccines. This method can be used with both the natural as well as synthetic polymers. The aqueous solution is dispersed in a lipophilic organic continuous phase. The continuous phase is generally consisted of the polymer solution that eventually encapsulates of the protein contained in dispersed aqueous phase. This results in the formation of a double emulsion. The emulsion is then subjected to solvent removal either by solvent evaporation or by solvent extraction, **figure 1.4B**.

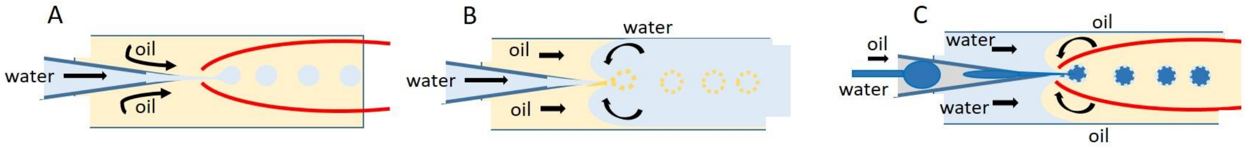

Figure 1.4 *Schematic illustration of emulsion techniques in microfluidic devices A) single (W/O), B) double (W/O/W) and C) triple (W/O/W/O) emulsions.*

Triple emulsion technique

Triple emulsion method of microspheres preparation involves the formation of the multiple emulsions or the double emulsion of type w/o/w/o, **figure 1.4C**. The high droplet stability ensures accurate and independent control of droplet size and the number of the inner droplets in multiple emulsions. Furthermore, triple emulsion droplets can also be prepared by simultaneous breakup of a core-sheath stream in a single step without sequential emulsification. One major advantage of this approach is that it allows formation of ultra-thin inner shells in triple emulsion droplets. This strategy is also used to form ultra-thin shells in double emulsion droplets. For both cases, the shell thickness can be reduced to less than 1 µm, which is difficult to achieve through sequential emulsification [74].

The droplets generation mechanism is a process well-controlled, where various forces acting on the fluids flow are balanced. These forces include inertial force, viscous force, interfacial tension and buoyancy. In some case, also external forces are utilized such as electric, magnetic and centrifugal forces. The complex phenomenon of droplet breakup is determined by various dimensionless numbers, Capillar number (Ca) and Weber number (We), which are related to the fluid properties, channel geometries and flow conditions. The *Ca* represents the relative effect of viscous forces and surface tension, while the *We* number reflects he balance between inertial and surface tension forces.

The droplet breakup modes ca be applied to various channel geometries including cross-flow, co-flow, and flow-focusing. These three device geometries rely mainly on the viscous shear force for droplet breakup, **figure 1.5**.

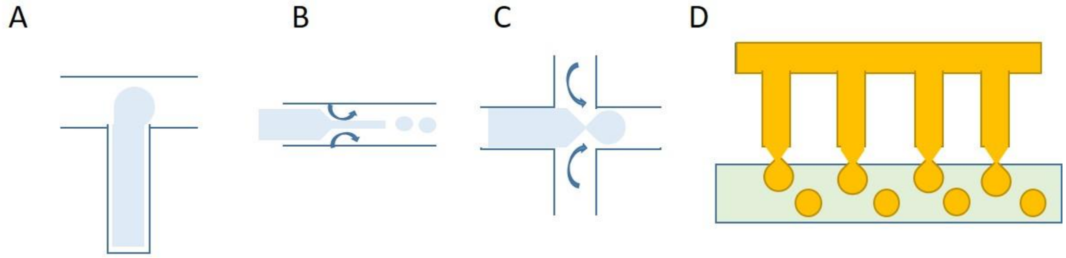

Figure 1.5 *Schematic illustration of various channel geometries, A) cross-flow, B) co-flow, C) flow-focusing, D) step-emulsification channel arranged with four parallelized drop markers.*

In cross-flow geometry, also called T-junction, the dispersed phase is sheared in T-shaped junction which has an angle θ (0° < θ < 180°) between the dispersed and the continuous phase channels, **figure 1.5A**. The droplets generated have high monodispersity with a coefficient of variation (CV) less than 2% and the size of the droplets generated is generally larger than 10 µm due to the limitation of the channel dimension.

In the co-flow geometry, also called coaxial junction, the dispersed phase channel is inserted into and aligned with the continuous phase channel, and dispersed phase and continuous phase fluids flow in parallel through the channels, **figure 1.5B**. The CV is less than 3% and the size of the droplets generated are larger than 10 µm. The flow-focusing mode has a channel geometry similar to the co-flow but has as a focus unit that shrinks the fluid passageway, **figure 1.5C**. There are also geometries that allow parallelization of multiple nozzles to obtain high throughput production droplets, **figure 1.5D**.

Two dominant types of droplet microfluidic devices used in generating various types of emulsion droplets: one is glass capillary microfluidics that have the advantage of high chemical resistance and ideal coaxial flow-focusing which enables preparation of droplets with wide range of material compositions and structures; the second one is soft-litographically fabricated poly(dimethilsiloxane) (PDMS) devices that have the advantage of preparing a large number of identical devices with micron-scale resolution, greater flexibility in the channel design compared to capillary devices, optical transparent, biologically inert, permeable to gases, and low in cost fabrication.

Other microfluidic devices, for example, fluoropolymer-based devices are commonly used in systems that involve chemical reactions with long-residence-time due to excellent chemical stability and moderate heat resistance. Organic reaction under strongly acidic and basic conditions ca be carried out in perfluoropolyether (PFPE) devices even at elevated temperatures. Quantum dots can be synthesized using the polytetrafluoroethylene (PTFE)-based microfluidic devices. Recently, 3D printed devices are gaining more attention in microsystems, the advantages are to obtained 3D design channels such as tapered geometry in XYZ in a cost-effectiveness manner and also the automation of microfluidic kit. Microfluidic channels as well as pumps expert user can producer functional modules whit 3D printing and can combine them to create their specific integrated microfluidic devices. However, these techniques have many remaining challenges, such as low resolution, lack of suitable materials, ad immature method to modify the surface wetting properties. Finally, microfluidic devices can also be prepared through hot-embossing, which is a versatile replication method that uses high pressure and elevated temperature to transfer structure in the master to the polymer. Advantages of hot-embossing for microfluidic include the ability to achieve very clean and precise features quickly and cost-effectively with materials that otherwise cannot be prepared using other technologies.

Microbeads with sizes ranging from a few microns to hundreds of microns can be generated by droplet microfluidics. For instance, as drug delivery vehicles [74-76] microcapsules or multi-core microbeads can be prepared with well-defined structures and compositions that allow for high encapsulation efficiency and well-controlled release of the encapsulate. As cell carriers, [69] hydrogel microbeads can be produced to act as extracellular matrix (ECM) to protect cells from the surrounding environment and maintain efficient nutrient and metabolic exchanges for long term cell culture. As a result, these cell-laden microbeads have direct applications in tissue engineering [77], stem cell therapy [78], and single cell studies [79]. In addition, liposomes or polymersomes with multicompartment structures can be generated by droplet microfluidics in an exquisite and facile manner, making them ideal candidates for artificial cells [80,81]. Therefore, it allows precise tuning of the compositions and geometrical characteristics of microbeads [82,83]. Exploiting these advantages, engineered microbeads with controlled sizes, monodispersity, diverse morphologies, and specific functions can be generated, and are playing an increasingly important role in biomedical fields [84,85]. Although nanoscale particles can be fabricated by droplet microfluidics [72], low concentration of precursor solutions are used, which reduces the production rate. Hydrogel microbeads produced by droplet microfluidics can serve as ideal ECM-like materials for 3D cell culture. There is a growing interest in the application of these cell-laden hydrogel microbeads as therapeutics or artificial organ/tissue building blocks for tissue engineering

However, encapsulation of cells with controlled number of cells per particle is still a big challenge, especially for single cell study

1.4 Fabrication Methods

The produced droplets are converted into solid microparticles by chemical or physical crosslinking techniques.

1.4.1 Chemical crosslinking

Covalent bonds are normally formed among polymer chains in chemically cross-linked hydrogels, and most of their linkages are strong and permanent when they are compared with those of the physically cross-linked hydrogels. Up to now, several crosslinking methods have been reported, and they typically involve free radical polymerization induced crosslink, enzymatic induced crosslink, Diels–Alder "click" reaction, Schiff base formation, oxime formation and Michael type-addition [68]. Compared with physically cross-linked hydrogels, chemically cross-linked hydrogels usually exhibit enhanced stability under physiological conditions and excellent mechanical properties as well as tunable degradation behavior.

In general, there are four types of chemical crosslinking

1. *Crosslinking Molecules*
2. *Polymerization*
3. *Photopolymerization*
4. *Enzymatic Crosslinking*

1.4.1.1 Crosslinking Molecules

Polymer chains can be conjugated through use of crosslinking molecules or can be directly bound to each other. The simples form of crosslinking takes place between aldehyde and amino groups to form a Schiff base, where di-aldheyde cross linkers (such as glutheraldehyde) are used for hydrogelation. Crosslinking molecules also present a facile method to bind biofunctional molecules into hydrogel [68]

1.4.1.2 Polymerization techniques

The polymerization reaction is normally initiated with radiation, ultraviolet, or chemical catalysts. A small amount of cross-linking agent is added in any hydrogel formulation. The choice of a suitable initiator depends upon the type of monomers and solvents being used. The polymerized hydrogel may be produced in a wide variety of forms including films and membranes, rods, particles, and emulsions. Polymerization is the simplest technique which involves only monomer and monomer-soluble initiators. High rate of polymerization and degree of polymerization occur because of the high concentration of monomer. However, the viscosity of reaction increases markedly with the conversion which generates the heat during polymerization. These problems can be avoided by controlling the reaction at low conversions [86].

1.4.1.3 Photopolymerization

Photopolymerization is one of the most prevalent ways to initiate polymerization due to the fast response time, which can induce polymerization within seconds, enabling less consideration of emulsion stability [72]. The advantage of this method is the rapid formation of hydrogel networks at ambient temperature under mild conditions, and the mechanical properties of hydrogels can be tuned by controlling the crosslinking reactions [87]. The cross-linked site is also ready to be accurately selected, because the photo-initiated polymerization takes place under light exposure and only the irradiated areas are involved in hydrogel crosslinking. Photo-initiated polymerizations are related to the presence of unsaturated groups, in most situations, the (meth)acrylates. The double bonded carbons in these groups are highly reactive and promote a free radical chain-growth polymerization when they are exposed to photo irradiation. Conventionally, water-soluble polymers with hydroxyl, carboxyl and amino groups can react with acryloyl chloride, glycidylmethacrylate

(GMA) and N-(3-aminopropyl) methacrylamide to introduce vinyl groups.102 Formation of biomedical hydrogels usually requires the presence of cytocompatible photoinitiators, such as Irgacure 2959, Irgacure 1173, Irgacure 819, Irgacure 651. Those photo-initiators can absorb specific light at different wavelengths, including UV (250 nm–370 nm), visible blue & purple (405 nm–550 nm) and red light (750 nm–810 nm) and either decompose (Type I) or abstract hydrogen from a donor molecule (Type II) to form radical initiating species. However, there are still some concerns about DNA damage caused by UV radiation. Some studies claimed that UV radiation posed a potential risk of accelerating organ/tissue aging and cancer onset. Thus, visible light photoinitiation might be an alternative candidate. Blue light (visible) photo-initiators have been used, such as camphorquinone and eosin Y, lithium phenyl-2,4,6-trimethylbenzoylphosphinate (LAP), riboflavin and ruthenium. These photo-initiators were able to effectively photo encapsulate various cells with high viability. Besides, visible light more readily penetrates tissue, which creates a pre-polymer solution forming hydrogel after subcutaneous injection.

1.4.1.4 Enzymatic crosslinking

Enzymatic crosslink occurs when enzymes, such as transglutaminase and peroxides catalyse crosslinking reactions between polymer chains. This approach has been used to form fast gelling, non-toxic stable hydrogels, [68].

1.4.2 Physical Crosslinking

Physically crosslinked hydrogels are usually created by intermolecular reversible interactions, such as ionic/electrostatic interaction, hydrogen bonds, polymerized entanglements, hydrophobic/hydrophilic interactions, crystallization/stereo-complex formation, metal coordination and π–π stacking. In ionic interactions, hydrogels can be crosslinked under mild conditions, at room temperature and physiological pH. This process of cross-linking does not require presence of ionic groups in the polymer. The use of metallic ions yields stronger hydrogel [86]. For stereocomplex formation, a hydrogel is formed through crosslinking that is formed between lactic acid oligomers of opposite chirality [86]. Hydrophobic interactions result in the polymer to swell and uptake water that forms the hydrogel. Polysaccharides such as chitosan, dextran, pullulan and carboxymethyl curdlan [86] are reported in literature for the preparation of physically crosslinked hydrogels by hydrophobic modification. Protein interaction involves block copolymers that contains repetition of silk-like and elastine-like blocks called ProLastins [85]. These ProLastins are fluid solutions in water and can undergo a transformation from solution to gel under physiological conditions because of the crystallization of the silk-like domains [86]. Crystallization involves freezing-thawing process and creates a strong and highly elastic gel [64]. The prominent advantage of a physical crosslink is biomedical safety owing to the absence of chemical crosslinking agents, thus, avoiding potential cytotoxicity from unreacted chemical crosslinkers. More importantly, physically crosslinked hydrogels are stimuli-responsible with self-healing and injectable properties under room temperature. These hydrogels can be designed as bioactive hydrogels for the encapsulation of living cells and drug delivery of therapeutic molecules.

1.4.2.1 Ionic Crosslinking

The ionic/electrostatic interaction that has been extensively applied to the construction of hydrogels is the basis of a routine physical crosslink with 2 molecules of opposite electric charges cytostatic interactions occur between the opposite charged macromolecules and those macromolecules interact with each other to yield polyelectrolyte complexes [87]. The hydrogels generated from those polyelectrolyte complexes can be modulated with a number of factors, including the charge density of the polymers, the mixed ratio and the amount of each polymer, as well as the soluble microenvironment of polymer. The specific advantage of an ionic/electrostatic interaction is its self-healing ability as a result of which the physical network of hydrogels can be broken at high stress and reform once the stress is removed. However, the mechanical strength of hydrogel is extremely limited owing to the crosslinking strategy of the ionic/electrostatic interaction.

1.4.2.2 Hydrogen Bonding

Hydrogen bond is one of the most important noncovalent interactions. For example, hydrogen bond could stabilize a secondary structure during a peptide or agarose based hydrogel formation. For hydrogel formation, amide, urea, carboxylic acid, pyrrole, carbazole and hydroxyl groups could form hydrogen bonds among themselves or interact with electron donor groups, such as pyridine and imidazole groups. However, a single hydrogen bond is generally not strong enough to support hydrogel formation. Can be used to form non-covalently crosslinked hydrogels, stabilized through physical chain interaction. Microparticles prepared by polymerization method result in a polymeric matrix with covalent linkages which make them chemically resistant as well as mechanically durable as compared to other methods. However, radicals generated during polymerization can cause serious problems considering their biotoxicity. Solidification droplets through temperature induced physical gelation and freezing can avoid some of these issues. The gelation method is applicable to droplets made of collagen, agarose and gelatin, which can be transformed into hydrogel by simply changing the temperature. The freezing method relies on the fact that some hydrocarbon molecules and lipid molecules including glycerides process melting point at or above room temperature. Microcapsule prepared by freezing exhibit large pores in the shell, inducing leakage of encapsulatns.

1.4.3 Physico-chemical processes

1.4.3.1 Solvent Evaporation

This process is carried out in a liquid manufacturing vehicle phase. The microcapsule coating is dispersed in a volatile solvent which is immiscible with the liquid manufacturing vehicle phase. A core material to be microencapsulated is dissolved or dispersed in the coating polymer solution. With agitation the core material mixture is dispersed in the liquid manufacturing vehicle phase to obtain the appropriate size microcapsule. The mixture is then heated if necessary to evaporate the solvent for the polymer of the core material is disperse in the polymer solution, polymer shrinks around the core. The core materials may be either water soluble or water in soluble materials. Solvent evaporation involves the formation of an emulsion between polymer solution and an immiscible continuous phase whether aqueous (o/w) or non-aqueous.

1.4.3.2 Phase separation technique

This process is based on the principle of decreasing the solubility of the polymer in organic phase to affect the formation of polymer rich phase called the coacervates. In this method, the particles are dispersed in a solution of the polymer and an incompatible polymer is added to the system which makes first polymer to phase separate and engulf the drug particles. Addition of non-solvent results in the solidification of polymer. The process variables are very important since the rate of achieving the coacervates determines the distribution of the polymer film, the particle size and agglomeration of the formed particles. The agglomeration must be avoided by stirring the suspension using a suitable speed stirrer since as the process of microspheres formation begins the formed polymerize globules start to stick and form the agglomerates. Therefore, the process variables are critical as they control the kinetic of the formed particles since there is no defined state of equilibrium attainment.

Chapter 2

Biomimicking the Extracellular Matrix of Central Nervous System

2.1 Extracellular matrix of soft tissues

The extracellular matrix (ECM) is a complex scaffold consisting of structural and functional proteins, proteoglycans, glycoproteins and glycosaminoglycans arranged in a tissue-specific orientation. Working and interacting together, the individual ECM components direct the processes of acute inflammation, healing and tissue remodeling to achieve tissue function and restore homeostasis when tissue integrity is disrupted. It is the presence of these matrix factors and their inhibitors in tightly controlled concentrations and states of activity that lead to successful tissue restoration following injury. For example, fibrillar collagens provide the support and tensile strength that give the ECM its structural integrity. Following tissue trauma, type I collagen stimulates the respiratory burst, granule exocytosis and cytokine secretion by human leucocytes, leading to chemotaxis of cell types needed for wound healing [88]. Glycoproteins, such as fibronectin and laminin, provide attachment sites for cells of various types. Fibronectin attracts and binds cells through integrins, allowing them to repopulate the site of injury [89]. Laminin helps direct the formation and stabilization of blood vessels and also provides attachment sites for fibroblasts and endothelial cells [90]. Glycosaminoglycans, such as hyaluronic acid, aid in retaining matrix hydration and act as signalling molecules that direct tissue repair and regeneration [91]. Hyaluronic acid also inhibits the excessive formation of scar tissue by inhibiting platelet aggregation and the release of platelet-derived growth factor and other cytokines [91]. Growth factors and matrix metalloproteinases contribute to matrix turnover, actively directing the local cells to increase matrix production, initiate angiogenesis and vasculogenesis, and migrate and proliferate to where they are needed. For example, transforming growth factor-b and connective tissue growth factor (CTGF) stimulate collagen deposition following injury and inhibit matrix degradation [93,94]. Vascular endothelial growth factor (VEGF), CTGF and basic fibroblast growth factor (FGF-2) all contribute to the reestablishment of the local vascular supply needed to provide nutrients for healing and rid the damaged area of dead cells, tissue debris and metabolic waste [94,95].

The ECM is a dynamic environment in which components act and react with each other—and with the cells that are contained within it—to maintain homeostasis in the uninjured state and to restore homeostasis in the case of injury or tissue loss. The ECM is not a static structure but is highly involved in regulating the tissue microenvironment. The components within the ECM protect growth factors from degradation and modulate their synthesis, assist in orchestrating the complex processes of tissue inflammation and repair and modulate the localized innate immune response [91,94,96]. Because of its integral roles in maintaining tissue homeostasis and providing structural support, a biological ECM graft material that recapitulates the function and structure of the lost tissue can provide the key extracellular signals and cues needed to restore damaged tissues to their natural state. In vivo, cells reside in a complex yet highly organized environment containing a diverse collection of soluble and insoluble proteins, sugars, and other cells, and the exact composition and spatial orientation of a cell's microenvironment dictates the local mechanical environment that a cell is exposed to. The mechanical environment is composed of endogenous forces generated by the cells themselves, as well as exogenous forces that are applied to cells by the surrounding microenvironment. Endogenous forces are largely produced by cytoskeletal contractility within cells [97, 98], whereas exogenous forces exist in a variety of forms, including gravity, shear stress, and tensile and compressive forces. Cells receive these exogenous forces through interaction with the ECM, and the local stiffness of the ECM is an important mechanical effector of cell behavior. Interestingly, external physical forces can shape the mechanical environment and make it a continually evolving and dynamic microenvironment for cells. Physical forces have long been known to contribute to tissue development and homeostasis through clinical observations of brain morphology and bone remodeling [99]. cells are constantly synthesizing, breaking down, or otherwise rearranging ECM components to change ECM composition and topography. On the other hand, the ECM has a fundamentally important role in dictating cell behavior, and as such, any changes in ECM dynamics will influence adjacent cells and influence their cellular activities. By maintaining this feedback loop between cells and their ECM, tissues can become very Reprintedive to the physical forces imposed on it. However, when tissue homeostasis becomes imbalanced, tissue function generally becomes impaired as a result of aberrant cellular behavior. Thus, it is critical to understand how cells respond to their mechanical environment for the treatment and prevention of a variety of diseases. Stiffness, or rigidity, of a material is defined as the extent to which a material resists deformation in response to an applied force. Stiffness is used to indicate whether a material is compliant (soft) or rigid (hard). In biology, stiffness has been used to collectively represent mechanical properties of a biological substrate. Our tissues, which are composed of a variety of different ECM molecules, feature a wide range of elastic moduli (**figure 1.1**), and each tissue/organ has specific stiffness for fulfilling physiological needs. An ideal material for soft tissue reconstruction must be strong, easy to handle and biocompatible while supporting the growth of new tissue [99].

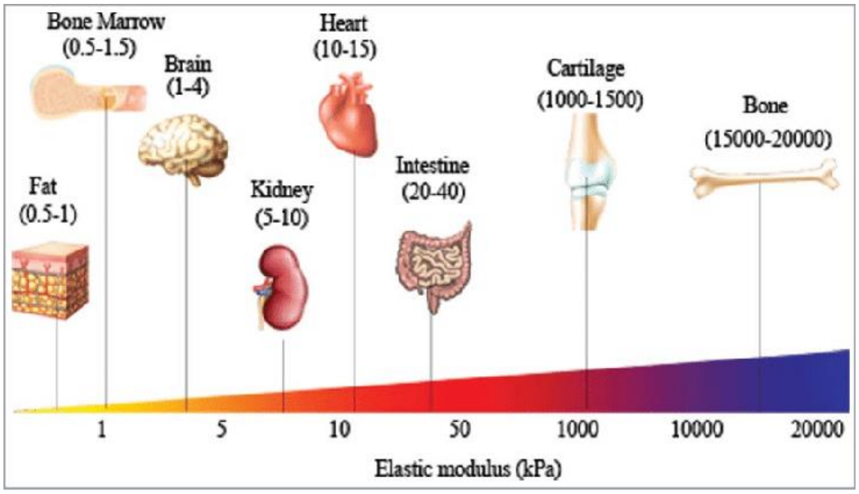

Figure 2.1 *Distinct modulus of human tissues suggesting tissue-specific stiffness. Different tissues with their specific elastic modulus in the body are correlated with their functions (Reprinted from Cox et al., [100]).*

2.2 CNS - extracellular matrix

The extracellular matrix (ECM) in the brain plays a defining role in regulating stem cell differentiation, migration and proliferation during development. The brain ECM takes on many different forms and compositions throughout neurogenesis [101]. The role of extracellular matrix (ECM) in neurological development, function and degeneration has evolved from a simplistic physical adhesion to a system of intricate cellular signaling. While most cells require ECM adhesion to survive, it is now clear that differentiated function is intimately dependent upon cellular interaction with the ECM [102]. Biological components form a major structural component of the CNS extracellular environment are glycosaminoglycans (GAGs) and also contain collagen (I, III, IV, V, and VI), fibronectin and laminin. The ECM of the CNS can be divided into three main sections (**figure 2.2**).

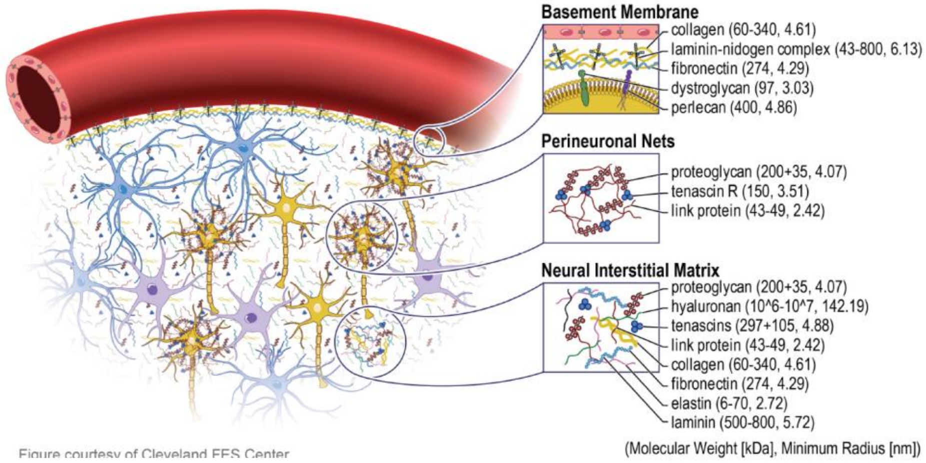
Basement Membrane
collagen (60-340, 4.61)
laminin-nidogen complex (43-800, 6.13)
fibronectin (274, 4.29)
dystroglycan (97, 3.03)
perlecan (400, 4.86)
Perineuronal Nets
proteoglycan (200+35, 4.07)
tenascin R (150, 3.51)
link protein (43-49, 2.42)
Neural Interstitial Matrix
proteoglycan (200+35, 4.07)
hyaluronan (10^6-10^7, 142.19)
tenascins (297+105, 4.88)
link protein (43-49, 2.42)
collagen (60-340, 4.61)
fibronectin (274, 4.29)
elastin (6-70, 2.72)
laminin (500-800, 5.72)
(Molecular Weight [kDa], Minimum Radius [nm])

Figure courtesy of Cleveland FES Center

Figure 2.2 *Extracellular matrix in brain. The extracellular matrix (ECM) in the brain is divided into three major components. The basement membrane (basal lamina) which lies around the cerebral vasculature, the perineuronal net which surround neuronal cell bodies and dendrites, and the neural interstitial matrix which are diffusely distributed*

between cells in the parenchyma. The blue, purple, and yellow cells depict astrocytes, microglia, and neurons, respectively (Reprinted from Kim Y. et al, [103]).

The first is the **basement membrane**, a layer that surrounds the endothelial cells of blood vessels, which is mainly composed of laminin, perlecan, fibronectin and heparin sulphate proteoglycan. The second section consists of **perineuronal nets** (PNNs) that surround neuronal cell bodies and smaller neurons. The final section is the **neural interstitial matrix**, a dense network of ECM components furthest away from the basement membrane and perineuronal nets. The ECM polymer network itself is primarily composed of a hyaluronic acid-based backbone [101] functionalized with ECM proteins. Brain ECM proteins such as *collagens, laminins* and *fibronectins* provide mechanical support as well as important molecular cues for cell behaviour. *Fibronectin* is a large multidomain glycoprotein expressed as an ECM protein or as a soluble plasma protein. In the adult CNS, fibronectin is restricted to the vasculature and is not expressed by neurons and glia [104]. *Laminins* are heterotrimeric glycoproteins composed of α-, β- and γ-subunits. To date, 14 different laminins have been identified [105], of which only Laminin 111 has been identified in the CNS, while multiple forms have been found in the peripheral nervous system (PNS).

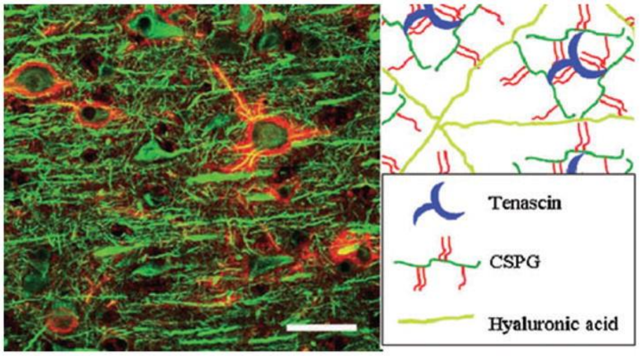

Figure 2.3 *Perineuronal nets (PNNs). Brain stained with microtubule-associated protein 2 (MAP2) (green) and Wisteria floribunda agglutinin (WFA) (red) (A). Model of PNNs (B). Hypothetical PNN ternary complex of tenascin, chondroitin sulfate proteoglycans (CSPGs) and hyaluronic acid (HA), (Reprinted from Bonneh-Barkay D et al, [101]).*

While laminin expression has been detected during pathway development [106], the major function of astrocyte-derived laminin in the adult is to maintain the blood brain barrier through actions on pericyte differentiation [107]. In culture, laminins universally promote neurite outgrowth, and an integrin-binding peptide (IKVAV) derived from laminin has similar actions and has been used to promote regeneration in vivo [108]. PNNs are reticular networks observed on the surface of neuronal cell bodies and proximal dendrites (**Figure 2.3**). This structure includes *lecticans, hyaluronic acid (HA), Tenascin-C and Tenascin-R*. It is thought that the HA–lecticans–tenascin complex deposited on neuronal surfaces may form a repulsive barrier against approaching axons and dendrites [101]. *Lecticans* are large secreted proteoglycans that carry mainly CS side chains and include aggrecan, neurocan, brevican and versican. These proteoglycans are characterized by the presence of an HA-binding domain. Two families of membrane-bound heparan sulfate proteoglycans (HSPGs) abundantly expressed in the CNS are glypicans and syndecans. Hyaluronan (also called hyaluronic acid: HA) is a unique GAG which is not attached to a core protein and whose sugars are not modified by sulfation or epimerization. Many of hyaluronan's physiological properties, including providing biomechanical integrity, altering tissue hydration and facilitating tissue assembly, are dependent on its size, concentration, and localization [104]. *Tenascin-C* and *Tenascin-R* are oligomeric multi-domain anti-adhesive proteins expressed in the CNS and are known to have roles in cell adhesion, neuronal migration, migration and differentiation of oligodendrocytes and cellular responses to growth factors [109]. *Tenascin-C* is expressed by astrocytes, oligodendrocytes and some neuronal populations [110], while *Tenascin-R* is expressed by oligodendrocytes and neurons [111]. They are predominantly expressed during embryonic development and then again in response to nervous system injuries in both animals and humans [104]. PNNs are a structural defined part of the ECM composed of a variety of proteoglycans. The diversity of proteoglycans in the ECM is dependent on differential expression of genes encoding core proteins, alternative splicing and transcription–termination, as well as variations in the length and types of glycosaminoglycan (GAG) side chains.

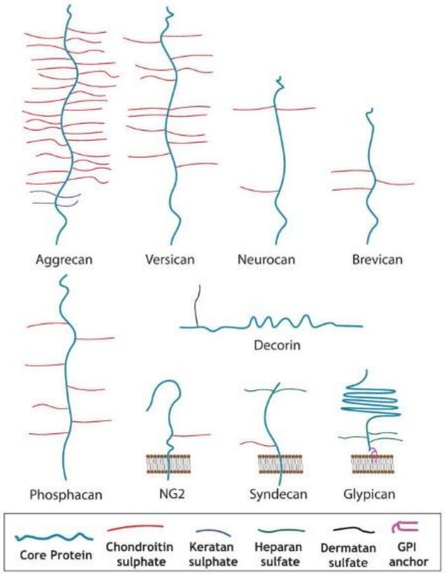
Aggrecan
Versican
Neurocan
Brevican
Decorin
Phosphacan
NG2
Syndecan
Glypican
Core Protein
Chondroitin sulphate
Keratan sulphate
Heparan sulfate
Dermatan sulfate
GPI anchor

Figure 2.4 *Major brain proteoglycans. Proteoglycans consists of a protein core decorated with unbranched sulfated glycosaminoglycan sugar chains. CSPG core proteins are decorated with one or more chondroitin sulfate sugar chains. Based on the core protein they are classified into lecticans (which includes neurocan, brevican, versican, and aggrecan), phosphacan, and NG2. HSPGs are decorated with HS chains. Syndecans are transmembrane proteins, while glypicans are anchored to the cell membrane with a GPI linkage. Decorin is a secreted proteoglycan with dermatan sulfate side chains (Reprinted from George N et al, [104]).*

As major components of brain ECM, proteoglycans mediate cell-cell interactions and modulate growth factor and cytokine signaling during development as well as in response to various pathophysiological conditions in the adult [112]. The signaling functions of proteoglycans in the brain are primarily due to their GAG chains [117], while the core proteins contain specific domains that determine localization and mediate interactions with cells and other matrix molecules. Proteoglycans can either promote or inhibit neuritic growth and possibly synaptic remodeling. Both the protein core and GAG side chains contribute to promoting or inhibiting neurite growth (**Table 2.1**) [102]. Built around a core protein, polymers of 20–

200 disaccharide repeats are attached through serine residues. Classified on the basis of disaccharide composition, GAGs are grouped as *chondroitin/dermatan sulfate, heparan sulfate (HS) and keratan sulfate (KS)*. HA is a non-sulfonated polymer of glucosamine and glucoronic acid, which exists as a protein-free polysaccharide on cell surfaces and in the ECM [102]. *Chondroitin sulfate (CS)* or HS side chains compose most central nervous system (CNS) proteoglycans; some of them are constituents of the ECM and others are bound to cell surfaces by a transmembrane domain or anchored with glycosyl phosphatidylinositol (GPI). CSPGs are the most studied proteoglycan in the nervous system. CSPG core proteins are classified as lecticans, phosphacan, and NG2. The exact mechanism by which CSPGs affect axonal guidance is not known. CSPGs may affect neuronal growth and regeneration by inactivating neuronal integrins [114].

Dermatan sulfate (DS) GAG chains are derived from the epimerization of D-glucuronic acid in chondroitin sulfate to L-iduronic acid [115]. Although most of the functions of DS are related to the development and homeostasis of peripheral tissue, DS GAGs, especially over sulfated GAGs, stimulate neuritogenesis [116,117]

HSPGs have important roles as modulators of cell signaling in brain, mainly by acting as co-receptors for many different cytokines and growth factors, such as FGFs [118], GDNF [119] and semaphorin 5A [120]. In contrast to the CSPGs, HSPGs binding to these receptors promotes axonal growth. HSPG core proteins are classified into syndecans, glypicans, perlecan, and agrins.

	GAGs
Heparan sulfate (HS)	Polymer of disaccharide of N-acetylglucosamine and glucoronic acid. HS moieties of cell surface proteoglycans modulate the biological responses to FGF.

Chondroitin sulfate (CS)	Polymer of disaccharide of N-acetylgalactosamine and glucoronic acid.
Dermatan sulfate (DS)	Polymer of disaccharide of N-acetylgalactosamine and iduronic acid.
Keratan sulfate (KS)	Polymer of disaccharide of N-acetylgalactosamine and galactose.
Hyaluronic acid (HA)	Non-sulfated polymer of N-acetylglucosamine and glucoronic acid. As opposed to other GAGs, it is not attached to a core protein. Component of PNNs. The biological effects of HA are mediated through cell surface receptors including CD44 and receptor for HA-mediated motility.

Proteoglycans

Glypican	A family of six GPI-anchored cell surface HSPGs that are widely expressed in the CNS. Bind laminin, thrombospondin, FGFs, VEGF and IGF. Associated with neurogenesis and neurite outgrowth.
Syndecan	A family of four membrane-associated HSPGs. Bind tenascin-C, fibronectin, laminin, HB-GAM, bFGF and TGFβ. Associated with LTP and synaptic function and neurite outgrowth.
Phosphacan	A secreted CSPG. Bind Tenascin-R/C and HB-GAM. Associated with neurogenesis, neuronal migration and neurite outgrowth.
Versican	Secreted CSPG. Binds to HA, Tenascin-R and fibronectin. Different alternative spliced variants have been identified. Associated with neuronal migration and neurite outgrowth.
Brevican	Secreted and GPI-anchored CSPG. Binds to HA and tenascin-R. Associated with neurite outgrowth and synaptic function.
Neurocan	A secreted CSPG. Binds to HA, Tenascin-R/C and bFGF. Associated with neurite outgrowth and synaptic function.

Other proteins

Tenascin	ECM protein associated with PNNs. Binds to brevican, phosphacan, neurocan, HA, syndecan, glypican and integrins. Associated with neurite outgrowth and LTP and synaptic function.

Laminin	A secreted family of key members of the ECM. Binds predominantly to integrins. Associated with migration, survival and synaptic function.
	ECM-modulating enzymes
MMP	Family of zinc-dependent extracellular proteases. Associated with neurogenesis, survival and plasticity.
TIMP	Inhibitor of MMPs. Associated with neuronal survival and plasticity.
tPA	Serine protease that converts inactive plasminogen to active plasmin. Key initiator of MMPs. Associated with neurite outgrowth, neuronal migration, survival and synaptic function.
ADAMTS	Protease family with aggrecanase activity associated with the ECM through a thrombospondin motif.
Plasminogen activator inhibitor 1	A serine proteinase inhibitor (serpin) plasminogen activator inhibitor.
Hyaluronidase	Family of enzymes that degrade HA.
Heparanase	An endo-β-D-glucuronidase that catalyzes the hydrolytic cleavage of the β-1,4-glycosidic bond in HS.
Chondroitinase	Lyase that degrades CS.
	ECM-binding factors
FGF	FGFs constitute a large family of polypeptides (eg, aFGF, bFGF, KGF) that are important in the control of cell growth and differentiation and play a key role in oncogenesis, developmental processes and neuronal development.
HB-GAM	HB-GAM (also designated as pleiotrophin) and midkine form a two-member family of ECM proteins that bind tightly to sulfated carbohydrate structures such as HS. Binds to phosphacan and syndecan. Associated with neurite outgrowth, axon guidance and synaptogenesis.
PDGF	PDGF is one of the numerous growth factors that regulate cell growth and division.
VEGF	VEGF is an important signaling molecule involved in angiogenesis.

Table 1: *Extracellular matrix (ECM) components. Abbreviations: PNN = perineuronal net; CSPG = chondroitin sulfate proteoglycan; Abbreviations: PNN = perineuronal net; CSPG = chondroitin sulfate proteoglycan; GAG =*

glycosaminoglycan; CNS = central nervous system; GPI = glycosyl phosphatidylinositol; HSPG = heparan sulfate proteoglycan; FGF = fibroblast growth factor; VEGF = vascular endothelial growth factor; HB-GAM = heparin-binding growth-associated molecule; bFGF = basic fibroblast growth factor; TGFβ = transforming growth factor β; LTP = long-term potentiation; MMP = matrix metalloproteinase; TIMP = tissue inhibitors of metalloproteinase; tPA = tissue plasminogen activator; ADAMTS = A disintegrin and metalloproteinase with thrombospondin motifs; PDGF = platelet-derived growth factor; (Reprinted from Bonneh-Barkay D et al, [101]).

ECM capacity to bind growth factors via HS and CS modulates their interaction with the cell surface. In fact, the localization and biological activity of factors such as fibroblast growth factors (FGFs) depend strongly on the presence and composition of the ECM. Cells that express high-affinity receptors but lack surface HS do not respond to these ligands [121]. HSPG can stabilize FGF, protect it from proteolysis and serve as a co-receptor influencing its interaction with cell surface high-affinity receptors [122]. Specific structural aspects, including sulfonation of HSPG, are required for the proper interaction of HSPG with FGF. Thus, the regulation of GAG biosynthesis and modification greatly influences the functions of HSPG. The differential binding characteristics of specific HS structures can potentiate or inhibit the biological activity of FGFs [102]. Other growth factor families, such as vascular endothelial growth factor (VEGF) and platelet-derived growth factor (PDGF), are known to bind to heparin/HS, which can modulate their biological activities [123]. The interaction between chondroitin sulfate proteoglycans (CSPGs) and growth factors has attracted less attention; however, recent evidence supports the ability of CS chains to bind growth factors and to modulate their role in growth factor cell signaling. During neurogenesis the ECM is constantly changing its morphology to modulate and guide axonal growth. The elastic modulus of the human brain varies across different regions. Different moduli are typically displayed by white and grey matter regions. The mammalian white matter, which is composed of the majority of glial cells and axons, is the stiffer of the two, with an elastic modulus of 1.9 kPa [68].

The mammalian grey matter, primarily composed of neuronal cell bodies, is elastically weaker with an elastic modulus of 1.4 kPa, [68].

2.3 *In vitro* models of CNS

Historically the culture of mammalian cells in the laboratory has been performed on planar substrates with media cocktails that are optimized to maintain phenotype. The study of neurons in 2D culture first became possible in 1907 when Rose Harrison introduced tissue culture by maintaining tissue explants outside of the animal and observing the outgrowth of nerve cells [124]. *In vitro* models are cell-based models which involve culturing cells in 2D on functionalized surfaces (tissue culture plastic, natural or synthetic polymer coatings), frequently co-cultured with other cell types [125]. *In vitro* cultures of neuronal cells on flat 2D surfaces offer simplified, high throughput systems to study disease, drug toxicity, and biological processes by controlling environmental factors and directly measuring cell responses [126,127]. These traditional *in vitro* models have provided a wealth of information about neural cell types; examples include spontaneous network formation, cell attachment sites for adhesion and migration, axonal guidance mechanisms, molecules (soluble and insoluble) in synaptic targeting, and the resting membrane potential of different cell types [128]. Since these early studies, *in vitro* tissue models of the CNS have advanced, however none are able to fully capture the functionalities and subtle mechanisms of the actual tissues. In fact, 2D cultures lack endogenous 3D cell-cell interactions and physiological cues provided by the ECM. This is due to challenges of complexity (structure, number and flux of bioactive factors), physiological relevance (substrate stiffness, cell-cell interactions, and ultrastructure) and methods for functional evaluation (electrophysiology). For these reasons, researchers are invested in the development of tissue-like models through tissue engineering. Tissue engineering aims to recapitulate human tissue systems outside of the body for tissue replacement and regeneration or for the in vitro study of cellular mechanisms and therapeutic development. 2D model systems still play a major role and are still considered the gold standard for (neuro)biological investigations [129,130]. Such 2D models are aimed not only at dissecting the fundamental mechanisms of neural communications and dynamics, but also at exploring the related effects of (novel) pharmacological compounds [131]. These networks are usually derived from animal tissue and grown onto rigid substrates, thus lacking most of the key in vivo-like constituents: cell morphology, cell-to-cell interactions, and spatially unrestricted neuritic outgrowth. While there is no substitute for the low cost and simplicity of 2D cell culture studies or the complexity provided by *in vivo* systems, the goal of 3D in vitro tissue modeling is to fill in the knowledge gap that exists between the 2D *in vitro* and *in vivo* approaches.

2.4 2D neuronal network

Most in vitro functional studies in the developing nervous system have been performed using traditional monolayer culture developed onto supports modified by extracellular matrix components such as glycoproteins: laminin, fibronectin, tenascin, the cell adhesion molecule Ll and the lectin concanavalin A (ConA) [131-137] and synthetic biopolymers such as poly-ornithine and poly-lysine [124,138-142], which are expressed at stages critical for neuronal differentiation in situ and are functional in neurite outgrowth in vitro [143-144], acting as adhesion proteins. In many studies, the role of cell-to-substratum adhesion in the initiation, elongation, and branching of axons from rat embryonic cells was investigated [141-142]. Neurons in culture showed that nerve outgrowth requires a solid substrate [145]. The first work studied the use of collagen purified from rat tails as adhesion factors because was the only option available. In 1974, poly-lysine proved an excellent substrate. Both adhesion and neurite outgrowth were markedly better than on collagen, and results were much more consistent. One year later, also poly-ornithine pre-treated surfaces showed strong adhesive properties and enhanced neuronal morphogenesis [141]. Both poly-lysine and poly-ornithine studies were based upon previous observation on the electrostatic interaction of poly-cation whit the negative charges of the cell membrane, which promote cell adhesion and growth**, figure 2.5.**

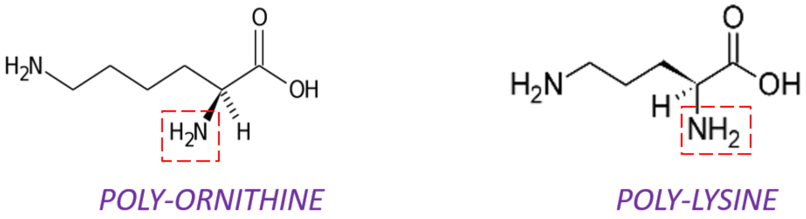
O
H2N
OH
H2N
H
POLY-ORNITHINE
O
H2N
OH
H
NH2
POLY-LYSINE

Figure 2.5 *Chemical structures of poly-ornithine and poly-lysine.*

The 2D culture cannot fully represent the *in vivo* environment, but it still serves as a powerful tool for understanding fundamental relationships between cell function and microenvironment parameters. The development of hippocampal neurons in culture can be divided into 4 stages as shown schematically in **figure 2.6** [124].

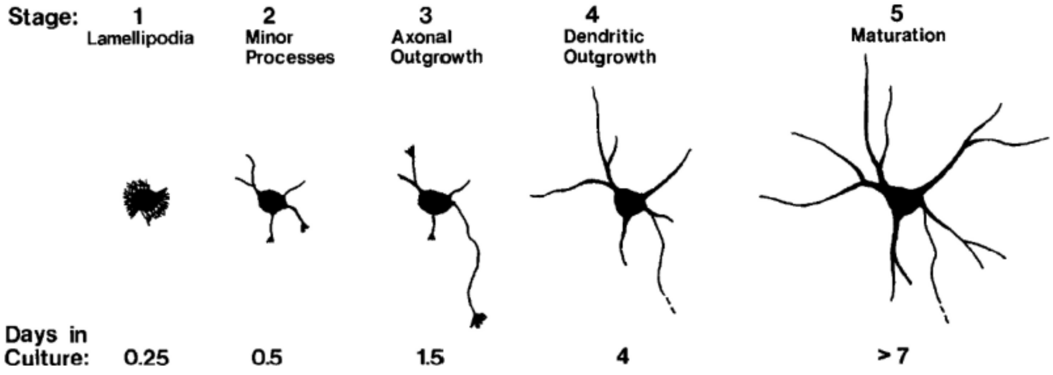
Stage:
1
Lamellipodia
2
Minor
Processes
3
Axonal
Outgrowth
4
Dendritic
Outgrowth
5
Maturation
Days in
Culture:
0.25
0.5
1.5
4
> 7

Figure 2.6 *Stages of development of hippocampal neurons in culture. (Reprinted from Dotti et al.[124]).*

Stage I: formation of lamellipodia. Shortly after the cells attach to the substrate, motile lamellipodia develop around the periphery of the cell. to the substrate, motile lamellipodia develop around the periphery of the cell. Because comparable structures have not been observed during neuronal development in situ, their appearance in culture may reflect the cell's Reprintedation to growth on an artificial, two dimensional substrates. The lamellipodia, which initially surround most ofthe circumference of the cell, break up into discrete, motile patches at intervals along the cell periphery. Neurites appear to arise preferentially at these sites, the lamellipodial patches becoming the neuritic growth cones.

Stage 2: outgrowth of the minor processes. This stage of development is characterized by the transformation of lamellipodia into distinct processes, which, in the course of a few hours, extend to a length of 10-15 μm, after the appearance of minor processes, one of the minor processes begins to grow at a much more rapid rate

Stage 3: formation and growth of the axon. Several hours after the appearance of minor processes, rather abrupt change occurs: one of the minor processes begins to grow at a much more rapid rate. From this stage onward, its rate of growth will average 5-10 times greater than the other processes of the cell. This process is the axon, and it can be identified unequivocally as soon as its growth spurt begins. At this point, the cell has become polarized.

Stage 4: growth of dendrites. Like the axon, dendrites develop from the minor processes that appear during the first day in culture, but significant dendritic growth begins only after about 4 d in culture, 2-3 d after axonal outgrowth. The temporal difference in the initiation of significant axonal. Dendritic growth differs from axonal growth in 2 other obvious but important respects. First, dendrites grow more slowly than axons. The rates, averaged over an interval of 24 hr, differ by at least a factor of 5 Second, unlike axons, several dendrites grow at the same time. If some internal mechanism prevents simultaneous elongation of more than one process during the phase of axon initiation, it must be altered when dendritic development begins.

From stage 3 onward, proteins that are homogeneously distributed over all cellular compartments at earlier stages become selectively enriched in major or minor neurites. Synapsin I, synaptophysin, and growth-associated protein 43 (GAP-43) become concentrated in major neurites [145], whereas microtubule-associated protein 2 (MAP2) becomes restricted to minor neurites [140]. Furthermore, the glycosylphosphatidylinositol-anchored glycoprotein Thy-l is enriched in axons of stage 5 neurons [138]. Ultrastructurally, hippocampal axons in vitro, as in vivo, lack polyribosomes that are prominent in dendrites [146]. Axons contain filamentous cytoskeletal elements that are packed more densely than in dendrites, with axoplasmic organelles being largely restricted to axonal branch points [147]. The orientation of microtubules also differs between axons and dendrites. In axons, all microtubules are oriented with their plus ends toward the axonal tip, whereas in dendrites both microtubules with minus and plus ends oriented toward the neurite tip are present [148]. The extracellular matrix components the mostly studied in the developing nervous system are t laminin and fibronectin, the neural cell adhesion molecule L1 and concanavalin A (ConA) which are expressed at stages critical for neuronal differentiation in situ and are functional in neurite outgrowth. Furthermore, several studies have stressed the importance of extracellular matrix molecules for the establishment of neuronal polarity.

2.5 3D neuronal network – microbeads

The intricate structure of the brain comprises highly organized interconnected neurons that interact with the extracellularmatrix (ECM) to form a complex network [149] During development, neural cells proliferate and migrate into discrete locations within the brain in response to various trophic cues [150]. Neurons also transduce topographical stimuli through interaction of the growth cone (a specialized axon tip containing filopodia) with the immediate environment [151,152] and mechanical cues that can direct neurite extension [153]. Guided neurite and axonal growth ensures appropriate and regulated connectivity within the overall neural circuitry, giving rise to specialized nuclei with specific functions within the brain. To promote neural regeneration within an unconducive environment, a scaffold needs to regulate cell adhesion, proliferation, migration and neurite elongation, recapitulating some of the events that occur during embryogenesis. Furthermore, this must occur within a three-dimensional (3D) architecture to allow for relevant and appropriate tissue reformation.

Biomimicry requires modelling the 3D scaffold on the biological target tissue processes, properties and features. The current challenge of biomimicry is amplified by the incomplete understanding of the following properties of brain tissue as a biological system:

- *Heterogeneity*: Neural tissue is comprised of varied anatomical regions due to the varied density and alignment of the tissues components (e.g. different cell types, biomolecules, blood vessels, fibrous proteins) in various regions.

- *Complex 3D tissue*: 3D culturing is a process crucial to reconstructing the in vivo structure-function relationship of the neural tissue. This would ensure that the newly formed tissue is 3D to enhance integration with the surrounding 3D tissue at the lesion zone. However, replicating the structural and functional framework has thus far been a challenge due to the high complexity of the 3D neural tissue network.

- *Unique neuronal micro-environment*: *In vivo*, the immediate microenvironment of neural cells is composed of the interstitial system, which accounts for approximately 20% of the total brain volume. The interstitial system (ISS) or neural microenvironment comprises of the extracellular matrix and the interstitial fluid (ISF). Briefly, the interstitial fluid serves as a medium that bathes the cells in a rich environment (of for example, contains hormones, neurotransmitters) and facilitates waste removal, nutrient supply, organic molecules such as proteins; while the extracellular matrix directly attaches to and anchors the cells as depicted in figure specifically highlights that the ECM enables intercellular adhesion and functions as a scaffold [154].

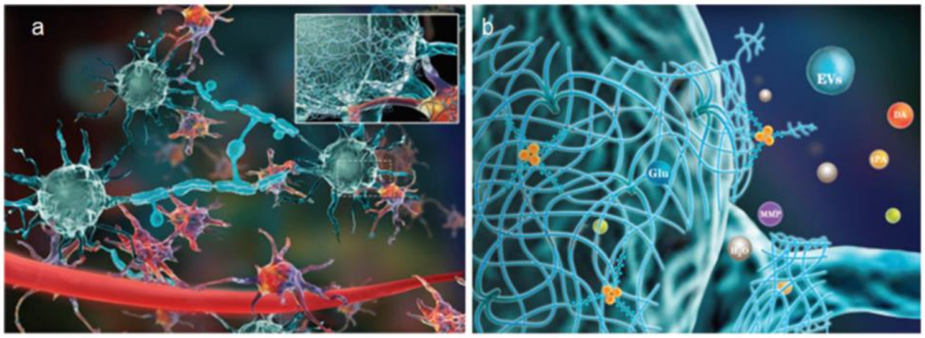

Figure 2.7 *Schematic depiction of the neural environment. (a) Spatial arrangement of the brain tissue compartments (cyan cells = neurons, purple cells = astrocytes, zoom-in subplot: ECM = a net-like cover attached to the surface of neural cells. (b) Enlarged view of the zoom-in subplot of the brain ECM in (a). The net-like cover = hyaluronic acid (HA) secreted by cells acting as a trestle for the ECM net-like structure. The penniform objects crossing the gaps between the HA chains = glycoproteins. Orange triple-circle = tenascin linking glycoproteins up. Multicoloured single circles = components of interstitial fluid (ISF), e.g., water molecules (H2O), extracellular vesicles (EVs), matrix metallopeptidase (MMP), glucose (Glu), dopamine (DA), and tissue plasminogen activators (tPAs). This figure is reused and reprinted from Progress in Neurobiology, Lei and co-workers. (Reprinted from Mahumane G.D. et al, [154]).*

The native ECM presents a macro to nanoscale topography, therefore, 3D scaffolds need to be processed to exhibit similar topographical cues (e.g. fibres and pores). Neural tissue has a dense vasculature in order to facilitate mass transport (e.g. of cells, nutrients, waste) [154]. Interconnected pores and channels designed in the architecture can accommodate for the absence of vasculature at the lesion site by facilitating mass transport within the 3D scaffolds. In addition, physical support must be offered to cells and axons, as well as physical properties similar to the native environment (e.g. elastic modulus). This poses a major scaffold design challenge because native brain tissue typically has an elastic modulus of 0.5–1 kPa [155,156]. Neural cells sense mechanical properties such as matrix stiffness and respond through cell colonization, migration and biased differentiation [157] and altered neurite formation and trajectory [158]. For instance, after 8 days of stem cell culture on photopolymerizable methacrylamide chitosan hydrogels with stiffness between < 1 and 7 kPa, biased cell differentiation was observed such that the < 1kP a substrate produced 59% oligodendrocytes, 33% neurons, and 2% astrocytes, while the 7kPa substrate produced 72% oligodendrocytes, 12% neurons, and no astrocytes, and the 3.5kPa substrate yielded intermediate values [159]. Furthermore, the rate of neurite extension of dorsal root ganglion cells is inversely proportional to substrate stiffness [158] and neurons produce more primary dendrites and shorter axons on stiffer substrates. A range of scaffolds including hydrogels, self-assembling peptides, and electrospun nanofiber scaffolds have been investigated as candidates for neural tissue engineering within the brain. Within CNS tissue, a greater proportion of the microscale tissue organization can be thought of as granular, with cells binding to cells. This is a colloidal structure, with dense cell packing as the main phase surrounded by proteoglycan rich extracellular space [159]. It is possible to replicate this architecture directly using densely packed cells, however, without the benefit of a vascular system, perfusion into and diffusion from tissue sections thicker than 200um is decreased, leading to the generation of toxic microenvironments [160]. To overcome this, hydrogels with higher internal porosity and lower cell densities can be used. The internal structure of this bulk hydrogel system needs to be optimized to support adequate cell adhesion and diffusion, whilst also entrapping expressed factors to support the generation of a niche cellular environment. Alternatively, the hydrogel structure can be modified to take the form of a granular structure, better replicating the structure of brain tissue. This multiphase structure encompasses hydrogel granules surrounded by an ECM rich secondary phase into which cells are seeded. Modification of bulk hydrogels into granular systems conveys further advantages. Granular hydrogels readily fluidise when compressed, a property known as shear thinning [161]. This increases the injectability of these systems. Furthermore, cells can be mixed homogeneously with fluidised hydrogel granules and the granular structure negates the effect of settling following mixing. The granules also act as a protective medium that supports cell viability during delivery. Granular systems work well as cell carriers. In a proposed stemcell delivery therapy for traumatic brain injury, a microsphere chitosan hydrogel scaffold functionalized with heparin to bind FGF-2 was shown to support radial glial cell (RGC) delivery when injected into a rat brain contusion model [162]. Analysis after 3 days revealed that the RGCs remained positive for nestin, indicating that the microspheres supported RGC viability and maintained the cells in a progenitor state. Granular scaffolds have also been found to facilitate cell infiltration and promote vascularization in-vivo. In a recent example, a granulated chitosan hydrogel scaffold was implanted into a rat spinal cord injury model and the granular hydrogel was found to elicit a dynamic restorative process, promoting axon outgrowth, vasculature ingrowth and diminishing fibrous glial scarring and the inflammatory response [163]. In a similar way, a microsphere hydrogel scaffold was injected into a rat cortical stroke cavity model with the goal of accelerating neural repair [164]. The scaffold consisted of HA microgel particles functionalized with multiple groups known to support cell binding and promote tissue repair. The scaffold was found to alter poststroke astrogliosis and inflammation, enhancing vascularization and neural progenitor cell migration into the site of damage. Hydrogel granules and spherical carrier-embedded hydrogels have also been used in other controlled delivery applications [165]. In one example, poly(N-isopropylacrylamide) (PNIPAm) hydrogel granules were used to facilitate cell transplantation of neurons into rat hippocampus [166]. PNIPAm hydrogel granules have a thermo-switching capability, such that mature neurons can be dissociated from the granules without neurite damage. In use, the granules enhanced cell survival and minimized the number of carriers needed for cell transplant. Unlike cells encapsulated inside bulk hydrogel, many of the mechanical and biochemical properties of granular gels are effectively decoupled. Whilst it is the bulk material of the hydrogel granules that supports the scaffold and maintains space for diffusion, it is the extended interconnected interface structure that occurs between granules that facilitates and localizes the exchange of biological factors and cell-cell interactions [167,168].

Chapter 3

Chitosan as adhesion factor for 2D neuronal networks

3.1 Bioactivity of chitosan

Chitosan (CHITO), a copolymer of glucosamine and N-acetyl-glucosamine, is obtained by alkaline deacetylation of chitin, which is the main structural component of exoskeletons of crustaceans, crabs, insects and fungal mycelia, **figure 3.1,** [169]. The deacetylation degree (DD) of chitosan represents the number of amino groups along the chains. It is calculated as the ratio of D-glucosamin and the sum of D-glucosamine and N-acetyl D-glucosamine. To be named “chitosan”, the deacetyleted chitin should contain at least 60% of D-glucosamine residues.

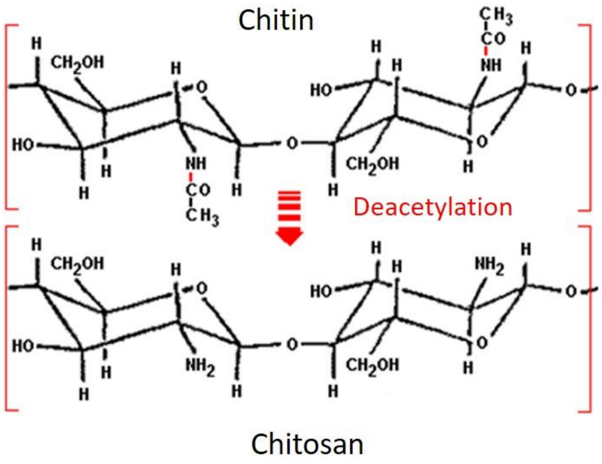

Figure 3.1 *Chemical structure of chitin and chitosan, (Reprinted from N. Acosta et al [169]).*

This polysaccharide is well known in biomedical application due to its attractive properties in terms of *biocompatibility, biodegradability, muco-adhesiveness, antibacterial and antifungal activity* and *low cost* [170]. The *biocompatibility* of chitosan depends on the preparation method (residual proteins could indeed cause allergic reactions) and on the DD, biocompatibility increases whit DD increase. Indeed, while the number of positive charges increases, the interaction between cells and chitosan increases as well, which tend to improve biocompatibility [170]. To explain chitosan *biodegradability*, it is important to remember that chitosan is not only a polymer bearing amino groups, but also a polysaccharide, which consequently contains breakable glycoside bonds [171]. Chitosan is actually degraded in vivo by several proteases, and mainly lysozyme [172,173]. The biodegradation of chitosan leads to the formation of non-toxic oligosaccharides of variable length The degradation rate of chitosan is mainly related to its degree of deacetylation, but also to the distribution of N-acetyl D-glucosamine residues and the molecular weight. The *mucoadhesion* of chitosan for example, can be explained by the presence of negatively charged residues (sialic acid) in the mucin – the glycoprotein that composes the mucus. In acidic medium, chitosan amino groups are positively charged and can thus interact with mucin. The mucoadhesion is directly related to the DD of chitosan: actually, if chitosan DD increases, the number of positive charges also increases, which leads to improved mucoadhesive properties. Due to its positive charges, chitosan can also interact with the negative cell membranes, which can lead to reorganization and an opening of the tight junction proteins, explaining the permeation enhancing property of this polysaccharide. As for mucoadhesion, if chitosan DD increases, the permeation ability also increases. There are two main mechanisms to explain chitosan *antibacterial* and *antifungal activities*. In the first case, positively charged chitosan can interact whit negatively charged groups at surface of cells, and as a consequence, alter its permeability. This would prevent essential materials to enter the cell or/and lead to the leaking of fundamental solutes out of the cells. The second case involves the binding of chitosan with the cell DNA, which would lead to the inhibition of microbial RNA synthesis. Chitosan antimicrobial property might result from a combination of both mechanisms. The abundance of sidechains in chitosan allows for easy modification and addition of other peptides or molecules. Moreover, chitosan can be easily molded into matrices of various forms such as films, porous scaffold, hydrogels, nanofibers and drug carriers. It can behave as a polycation under acidic conditions ($pH<6$), due to the protonation of free amino groups [172,173]; its pH-dependent cationic nature shows the intrinsic ability to interact whit anionic component (glycosaminoglycans and proteins), increasing the biomimeticity of the chitosan *in vivo* environment. Chitosan is commonly used in neural culture due to its linear structure similar to that one of the hyaluronic acid.

3.2 Aims

As a first step, 2D physically cross-linked chitosan films were prepared by phase inversion (liquid to solid) in an ethanol/sodium hydroxide solution [174] and covalent crosslinking [175] to investigate their interaction with neurons, with and without treatment with *adhesion proteins* (a.p.).

Then, the use of chitosan (CHITO) has been investigated as an alternative cell adhesion factor for *in vitro* preparation of two dimensional neuronal culture on different support (glass, polystyrene, silicon nitride). To validate the ability of chitosan to support neuronal adhesion, networks development and the differentiation capacity, morphological and functional characterizations were carried out and compered to the model proposed by Banker (**figure 3.2**) for the polarization process on hippocampal neurons growth on a substrate treat with a traditional adhesion factors, poly-ornithine. In the experiments, CHITO solutions at different concentrations were used as substrate by adsorbation and by nebulization whit an airbrush. Furthermore, using airbrush, there was the advantage to nebulize the material through the use of masks in order to create patterned adhesion surfaces which could generate non-random neuronal networks.

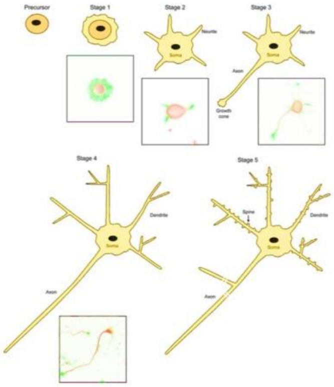

Figure 3.2 *Banker's model, neuronal stages' development from 0 to 7 DIV, (Reprinted from Dotti et al, [124]).*

3.3 Materials and methods

Materials

Chitosan solution: CHITO (low molecular weight, 75-85% deacetylated, code 448877, lot MKBD4275V, from Pandalus Borealis) was dissolved in 0.1 M acetic acid at concentrations 0.01%, 0.05%, 0.1%, 0.5%, 1%, 2% w/v and filtered through a syringe filter (5µm) to remove any undissolved material

Neutralizing solution: H_2Odd 40%, Ethanol 60% and sodium hydroxide 2% w/v

Genipin solution: genipin 2% in H_2O_{dd}

Methods

Four different methods to produce CHITO films:

1. *Thick Films* were prepared from CHITO solutions at concentrations 1% and 2% w/v. CHITO solutions (1 ml) were poured on a petri dish (Ø35mm) and allowed to dry before exposing them to 1 ml of gelling solution overnight. The gelling solution was prepared by mixing H_2O_{dd} 40%, Ethanol 60% and NaOH 2% w/v. The gelling solution composition was optimized on the basis of the data present in the literature and on results obtained by the FT-IR characterization of CHITO samples crosslinked at different concentrations of NaOH and genipin [174-175]. The obtained films were washed several times with distilled water.
2. *Spray coating:* CHITO solution was sprayed through airbrush onto different substrates petri dishes (plastic), micro-electrodes arrays (glass) and high density microelectrode matrices (MEA), high density-MEA (HD-MEA) (silicon nitride), giving also the possibility of producing a desired micro pattern through the use of stencil masks.

   The set-up is composed by a target-support where to place the substrate to be treated and an airbrush-support which allows to move the airbrush to the right and left. Films with different three different chitosan concentrations (0.1 %, 0.5%, 1%) and 1, 3, 6 and 10 layers were produced, to evaluate which was the minimum concentration of chitosan and the minimum number of layers to create a films able to support cell adhesion.

Definition of 1 layer: 1° spray for 2 second moving the airbrush to right and left, pause for 2 second 2° spray for 2 second

3. *Patterning*: To obtain pattern, CHITO solution at 1% was nebulized onto petri dishes with a mask. After nebulization, the films were allowed to dry before exposing them to a gelling solution for 20 min. The obtained films were washed several times with distilled water. All the procedure was performed at room temperature.
4. *Dip coating*: in order to obtain a complete comparison with the traditional adhesion factors, CHITO solutions at low concentration (0.1 %, 0.5%, 0.05%) were sterilized using a 0.22 μm sterile filters, poured by dip coating onto petri-dishes following the standard protocol and finally incubated for 4h, 8h and overnight at 37°C. As a control, the day before plating, other petri-dishes, MEA and HD-MEA were coated with poly-ornithine overnight.

3.3.1 Airbrush

The airbrush is an instrument that is used to spray various types of materials by nebulizing them with compressed air. It is used in precision work to produce thin lines, uniform color backgrounds and soft tones. Two different types of airbrushes have been used: a single-action, the simplest one, so called because the command button opens or closes the airflow, without adjusting the amount of mixture and a controlled double-action. It has a unique control that allows you to independently adjust the airflow and the amount of mixture released, moving back the command button, initially opens the air channel, then pressing deeper than the mixture.

The airbrush is connected by a flexible tube to an air source. The body sprays the material by atomizing it using a flow of compressed air. The material is inserted into a tank through an opening.

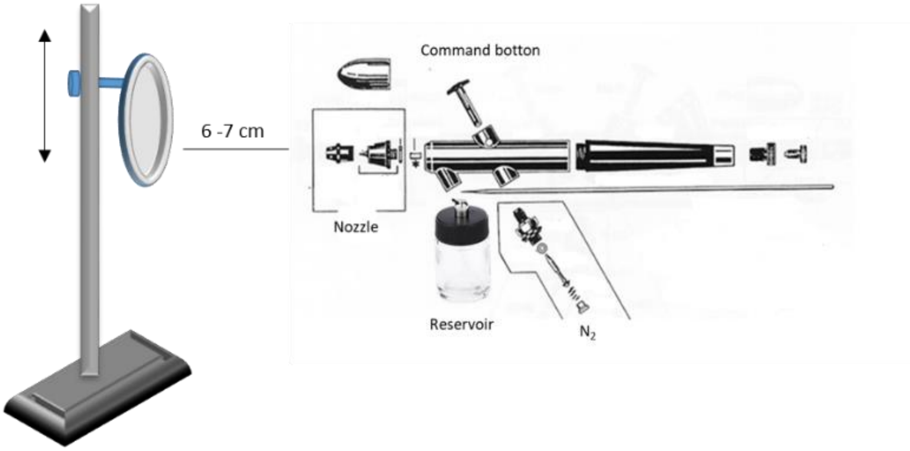

Figure 3.3. *Set-up airbrush.*

In the experiments, two types of airbrushes have been used; a *single-action* airbrush, the simplest one, so called because the command button opens or closes the airflow, without adjusting the amount of mixture and *controlled double-action* airbrush. It has a unique control that allows you to independently adjust the airflow and the amount of mixture released, moving back the command button, initially opens the air channel, then pressing deeper than the mixture. The set-up was composed by a target-support where to place the substrate to be treated and an airbrush-support which allows to move the airbrush to the right and left (**figure 3.3**). The main parameters for the process optimization are: nitrogen pressure, type of nozzle, distance between nozzle and target, time of spraying. The parameters were respectively set at 2.5 mbar (nitrogen pressure), 0.2 µm (the nozzle size), 6-7 cm (distance between nozzle and target) and the time of spraying at 2 second.

3.3.2 Patterned film

Samples have been prepared in plastic petri dishes, on which 1% CHITO solution was sprayed. Before spraying the solution, the PLA mask made by a 3D printer, was inserted inside the petri dishes, **figure 3.4**.

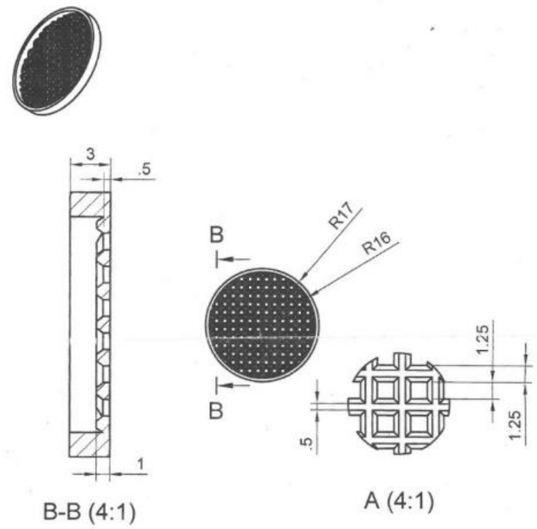

Figure 3.4 *PLA mask, main parameters of PLA mask to obtain patterned film*.

This mask has a circular shape, with a diameter of 34 mm. It consists of 120 squares, arranged in an orderly manner, which have a side of 1.25 mm, so each square covers an area of about 1.56 mm^2. CHITO solution was nebulized by the airbrush, maintaining a distance of 6-7 cm and an inlet pressure of 2.5 mbar.

The mask was removed and the samples were dried under a laminar flow hood for 5 min. The substrates were not treated by neutralizing solution, due to the fact that the CHITO solution sprayed was a very small amount. The samples were washing three times whit deionized water, sterilized in 70% ethanol, and then neutralized with medium culture.

3.3.3 Cell preparation

Hippocampi and cortical neurons were dissected and removed from embryonic Sprague-Dawley rats at gestational day 18 under sterile conditions. Hippocampal and cortex fetal tissue was enzymatically digested in Trypsin 0.125% in Ca++ and Mg++ free Hank's (Gibco Invitrogen) for 20' at 37°C. The enzymatic process was quenched by adding culture medium supplemented with 10% of FBS (Sigma-Aldrich) then the tissue was mechanically dissociated with a smoothly fire-polished Pasteur pipette. Neurons were re-suspended in plating medium consisting of Neurobasal medium (Gibco Invitrogen) with 2% w/v B-27 Supplement (Gibco Invitrogen), 1% Glutamax (Gibco Invitrogen), 1% Pen-Strepto (Gibco Invitrogen). Cultures were maintained in incubator at 37°C in a 5% CO2, 95% humidity atmosphere for 3-4 weeks by replacing half of the medium once a week. The experimental protocol was approved by the European Animal Care Legislation (2010/63/EU), by the Italian Ministry of Health in accordance with the D.L. 116/1992 and by the guidelines of the University of Genova. All efforts were made to reduce the number of animals used for the project and to minimize their suffering

3.3.4 Preparation of 2D networks on CHITO films

To evaluate the bioaffinity between CHITO and neurons, cultures were prepared using thick films treated and untreated with adhesion proteins (a.p.).

The day before plating, the thick *films* were sterilized in 70% ethanol for 1 hour and used for the cell culture experiments. In the first case, films were exposed to a mix of a.p., namely Laminin: P-D-Lysine (1:1), at the concentration of 0.05 mg/ml in sterile water (L-2020; P-6407 Sigma-Aldrich) and left in the incubator overnight at 37°C. The a.p. were then washed away from the films with sterile water. In the second case, both films were sterilized and used without any further treatment. Before cell plating, films were washed in a Neurobasal medium. Hippocampal neurons were plated onto the film surface at a seeding concentration of 1000 cell/µl with a final cell density of 800 cell/mm^2.

Moreover, to investigate on the use of chitosan as a cell adhesion factor, *petri-dishes* are pre-treated with chitosan solutions and PORN poured by *dip coating*. CHITO solutions were filtered using a 0.22 sterile filters. The samples were washes with sterilized water, neutralized with medium culture and then used for the cell culture. For patterning, films are obtained by spray coating whit and without mask stencil onto petri dishes; instead onto MEA and HD-MEA film are made only without mask stencil. Primary hippocampal and cortex neurons, isolated from embryonic day (E) 18 rat embryos, were plated at low concentration onto chitosan pre-treated petri dishes for the morphological studies (28-30 cell/mm^2) and at medium concentration onto chitosan pre-treated MEA and HD-MEA.

3.3.5 Characterization of CHITO films

3.3.5.1 Morphological characterization of neuronal networks by immunocytochemistry

To assess the expression of specific neuronal markers, hippocampal cultures were fixed in 4% paraformaldehyde in phosphate buffer solution (PBS), pH 7.4 for 30 min at room temperature. Permeabilization was achieved with PBS containing 0.5% Triton-X100 for 15 min at room temperature and non-specific binding of antibodies was blocked with an incubation of 45 min in a blocking buffer solution consisted of PBS, 0.3% BSA (bovine serum albumin Sigma) and 0.5% FBS. Cultures were incubated with primary antibody diluted in PBS Blocking buffer for 2 hours at room temperature or incubated at 4°C overnight in a humidified atmosphere. Cultures were rinsed three times with PBS and finally exposed to the secondary antibodies. Differentiation is the establishment of the two distinct classes of neuronal processes, axons and dendrites. To identify the major neurites as axons and the minor neurites as dendrites, the cultures were stained for MAP-2 (1:500, dendritic microtubule-associated protein), TAU

(1.200, axon microtubule-associated protein) and Akirin G (1:200, axon initial segment) to study their localization during early stages of axonal and dendritic development, TUBULIN βIII, clone TU-20 (1:500), NeuN 1:200 (neuronal soma), VGAT and VGLUT1 1:500 (GABA AND Glutamatergic vesicles), Synapsin 1:200 (synaptic vesicles), Dapi 1:10000 (nuclei). To verify the presence of glial cells in the culture, we fixed and exposed to the marker GFAP 1:1000 (glial marker). ImageJ and NeuronJ have been used to analyze, trace and measure neuritic processes.

3.3.5.2 MEA and HD-MEA recording and analysis

The spontaneous electrophysiological activity of 2D hippocampal and cortical neuronal networks was recorded at 15-25 days in vitro (DIV) by means of micro-electrode arrays (MEAs) made up of 60 planar microelectrodes (TiN/SiN, 30 µm electrode diameter, 200 µm spaced) arranged over an 8 X 8 square grid (except the four electrodes at the corners), supplied by Multi Channel Systems (MCS, Reutlingen, Germany). The electrophysiological activity was acquired with the 2100 System (MEA 2100-System, MCS), and signals were sampled at 10 kHz.

Furthermore, the spontaneous electrophysiological activity of 2D hippocampal and cortical neuronal networks was also recorded at 19-30 days in vitro (DIV) by means of high density micro-electrode arrays (HD-MEAs) made up of 4096 microeectrodes (electrode size 21µm x 21µm, electrode pitch 81 µm) arranged over a 64 X 64 square grid, supplied by 3Brain.

The electrophysiological activity was acquired with the Biocam X. Recordings were performed for 30 min outside the incubator at a temperature of 37 °C. To prevent evaporation and changes of the pH medium, a slow flow of humidified gas (5% CO2, 20% O2, 75% N2) was constantly delivered during the measurement sessions into a small plastic box covering the experimental MEA setup.

3.3.5.3 Data and Statistical analysis

Data analysis for electrophysiological activity acquire by MEA set-up was performed by using a custom software package named SPYCODE [176], developed in MATLAB (The Mathworks, Natick, MA, USA). Instead, data analysis for the recordings acquired by HD-MEAs was performed by usng a custom software ackage nemde BrainWave. Spike detection was performed by using the Precise Timing Spike Detection (PTSD) algorithm [177]. The algorithm requires three parameters: a different threshold set to 8 times the standard deviation of the baseline noise, a peak lifetime period (set at 2 ms) and a refractory period (set at 1 ms). To characterize the electrophysiological activity, we extracted some first order statistics. In particular, we evaluated the mean firing rate (MFR), i.e., the number of spikes per second of each channel and the percentage of random spikes, i.e., the fraction of spikes outside bursts. We also performed burst detection according to the method described in [178]. A burst is a sequence of spikes having an ISI (inter-spike interval, i.e., time intervals between consecutive spikes) smaller than a reference value (set at 100 ms in our experiments), and containing at least a minimum number of consecutive spikes (set at 5 spikes). The parameters extracted from this analysis are the mean bursting rate (MBR) and the mean burst duration (MBD), which are the frequency and the duration of the bursts at the single channel level respectively. The same approach used for the detection of bursts was applied for the detection of quasi synchronous events at network level called network bursts [177]. The extracted parameters are the network bursting rate (NBR) and the network burst duration (NBD), which are the frequency and the duration of the bursts at global net level respectively.

Statistical analysis was carried out using OriginPro 8 (OriginLab Corporation, Northampton, MA, USA). All data are presented as mean ± standard error of the mean. Statistical analysis was performed using a non-parametric Kruskal-Wallis test, since data do not follow a normal distribution (evaluated by the Kolmogorov-Smirnov normality test).

Differences were considered statistically significant when $p<10^{-3}$. In order to determine which of the sample pairs are significantly different, post-hoc test, using Dunn's test, has been applied.

3.4 Results

3.4.1 Characterization of CHITO crosslinking

The structure of the neutralized and genipin cross-linked chitosan, were analyzed by FT-IR spectra. In the case of neutralized CHITO, infrared measurements on fixed (2%) CHITO samples were made at different molarities of the neutralizing solution in order to determine the concentration of the neutralizing solution components (**figure 3.5**). From the results obtained, the increase in the NaOH concentration corresponds to a relative decrease in intensity of all the characteristic bands of chitosan, which corresponds to a decrease in functional groups on the surface of the CHITO sample.

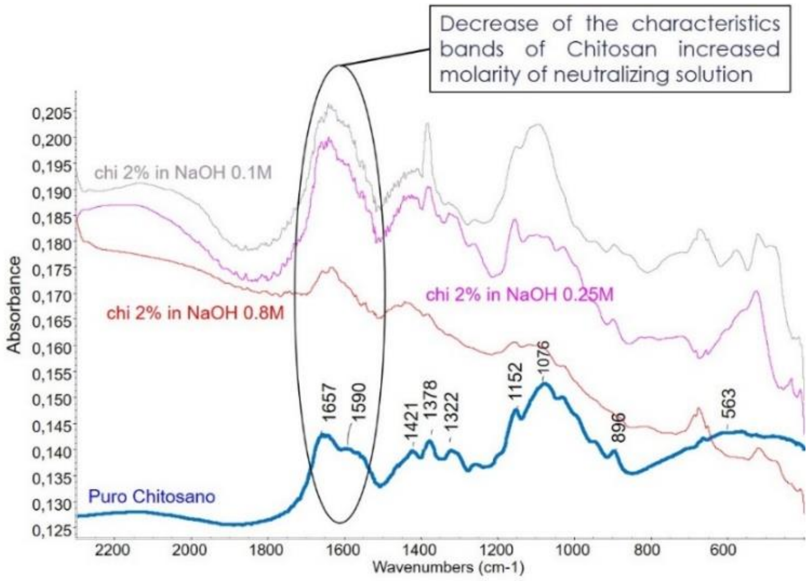
Decrease of the characteristics bands of Chitosan increased molarity of neutralizing solution

Figure 3.5 *FT-IR spectra of CHITO samples neutralized in NaOH solution at different molarity, a) pure chitosan (blu), 2% CHITO in NaOH 0.8 M (red), 2% CHITO in NaOH 0.25 M (pink), 2% CHITO in NaOH 0.1 M (yellow). The spectrum of the reference KBr was subtracted from each samples.*

For the protocol developed in this experiment, it has been chosen the 0.25 molarityto allow the formation of the hydrogel and to maintain, however, a certain amount of exposed surface charges (particularly that of the protonated amine groups).

The same evaluation was carried out on chitosan samples crosslinked in genipin: the covalent cross-linking with genipin follows the neutralization procedure, therefore the measurement was done on neutralized chitosan samples and neutralized chitosan further crosslinked with genipin, and the results showed that following the reaction with the crosslinking agent there is a decrease in intensity of the bands of the dNH of chitosan (1596 cm^{-1}), however the presence of amine groups persists (**figure 3.6**). The reason for maintaining a certain amount of surface charge of the polymeric substrate (especially of the amino groups) must be attributed to the interaction of the polymeric substrate with the cell population.

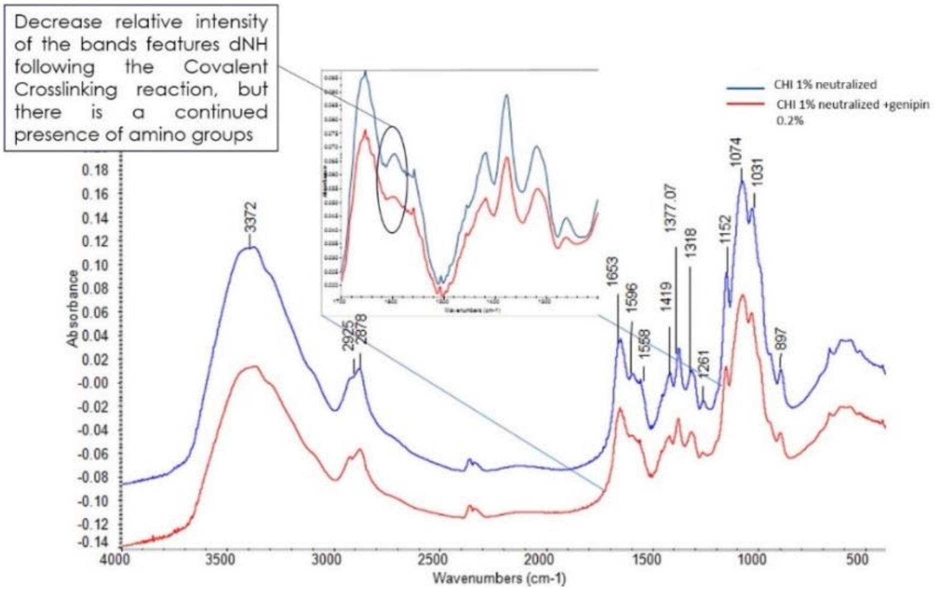

Decrease relative intensity of the bands features dNH following the Covalent Crosslinking reaction, but there is a continued presence of amino groups

Figure 3.6 *FT-IR spectra of CHITO samples cross-linked with genipin; 1 % CHITO in NaOH 0.25 M (blue), 1% CHITO in NaOH 0.25 M cross-linked in genipin (red). The spectrum of the reference KBr was subtracted from each sample.*

3.4.1 Characterization of sprayed CHITO films

The minimum number of layers able to support cell adhesion and growth was evaluated and characterized by optical and atomic force microscopies, by using 1% chitosan solution accordingly to the previous results [18]. **Figures 3.7 A-D** shows the optical images of 4 different number of layers; increasing the number of layers the film become more compact and homogeneous. Measurements of thickness were carried out by AFM microscope; apparently 1L films presented discontinuity with a thickness around 10 nm, instead 6 and 10 layers created a compact film, having millimeter thickness. From these preliminary results, 3 layers (3L) CHITO film, apparently more homogeneous than 1L but thinner than 6 and 10L, were sprayed also onto MEA and HD-MEA devices to carry out a preliminary electrophysiological characterization, **figures 3.7 E-F**. Moreover, cells were plated also onto petri- dishes coated with 1L. Surprisingly, the results showed that also 1% chitosan 1L film was enough to promote e support adhesion cells and growth.

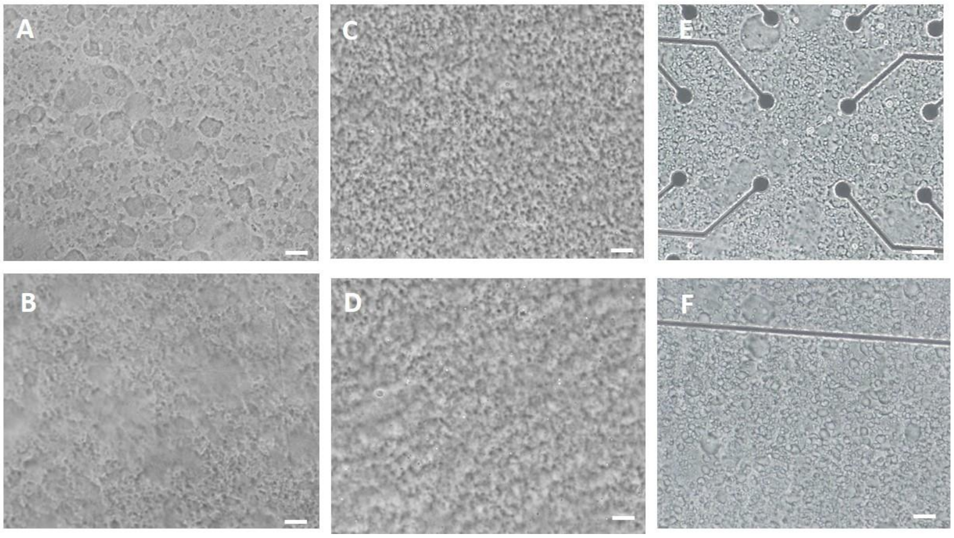

Figure 3.7 *Optical images of 1% CHITO films obtained with different sprayed layers A) 1L, B) 3L, C) 6L and D) 10L; E-F) 1% chitosan-3L onto active area of MEA. Scale bar: 50 µm.*

For this reason, all the new experiments based on spray coating, including patterning, were carried out onto 1% CHITO 1L film. Spray coating with low concentration of chitosan (< 1%) was evaluated highly insufficient to create a film; instead, it was observed that these chitosan concentrations (0.05%, 0.01%, 0.1%, 0.5%) were able to support adhesion and growth on substrates obtained by dip coting.

.

3.4.3 Characterization of 2D neuronal networks on CHITO films

As a first step, the bioaffinity of CHITO towards neurons was characterized. To conduct this study, a simplified standard 2D culture model was adopted and cells were thus plated onto the surface of CHI films. In order to evaluate the ability of physically cross-linked CHITO to promote neuronal adhesion and development, untreated and treated films with a.p. have been tested.

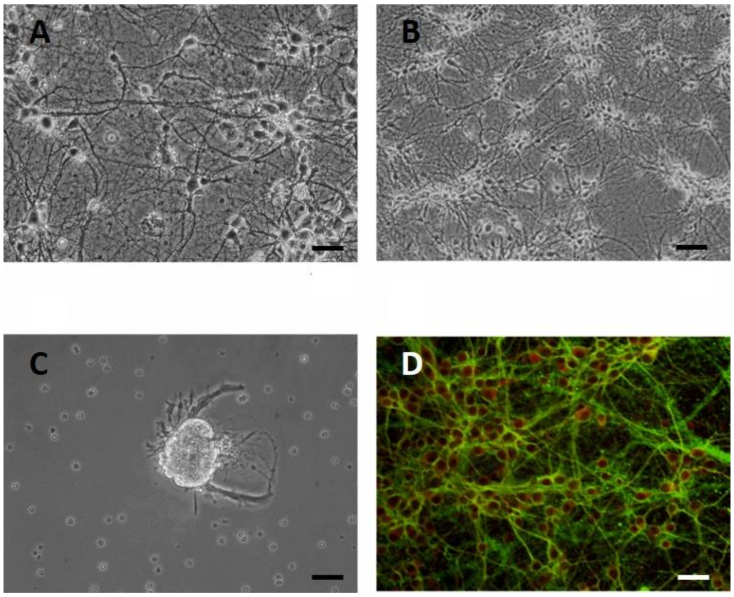

Figure 3.8 *Optical contrast phase images of 2D neuronal network: (A) 2% CHITO film untreated with a. p. at DIV 15; (B) 2% CHITO film treated with a. p at DIV 15; (C) petri dish untreated with a. p. at DIV 15; (D) 2% CHITO untreated film labeled for Tubulin-βIII (green) and NeuN (red) at DIV 25; Scale bar: 50 µm.*

Figure 3.8 shows the images of neuronal networks developed onto (**A**) 2% CHITO untreated film, (**B**) 2% CHITO film treated with a.p. and (**C**) petri dish untreated with a.p. at DIV 15 and (**D**) 2% CHITO untreated film, labeled for Tubulin-βIII and NeuN at DIV 25. With respect to the morphological development of the neuronal network, it can be observed that cell morphology is similar when cells are plated onto untreated and treated 2% CHITO films (**figures 3.8 A** and **3.8 B**).

Same results were obtained for cells cultured onto 1% CHITO films. In **figure 3.8C**, considered as the negative control, neurons, as expected, tended to form clusters and no network was obtained. Cells showed a homogeneous distribution and the formation of a dense network onto 2% CHITO untreated film even at DIV 25 (**figure 3.8 D**). Moreover, the presence of functional structures at DIV 25 was evaluated by 2D networks on 2% CHITO film labeled for Synapsin and VGAT-VGLUT, **figure 3.9**.

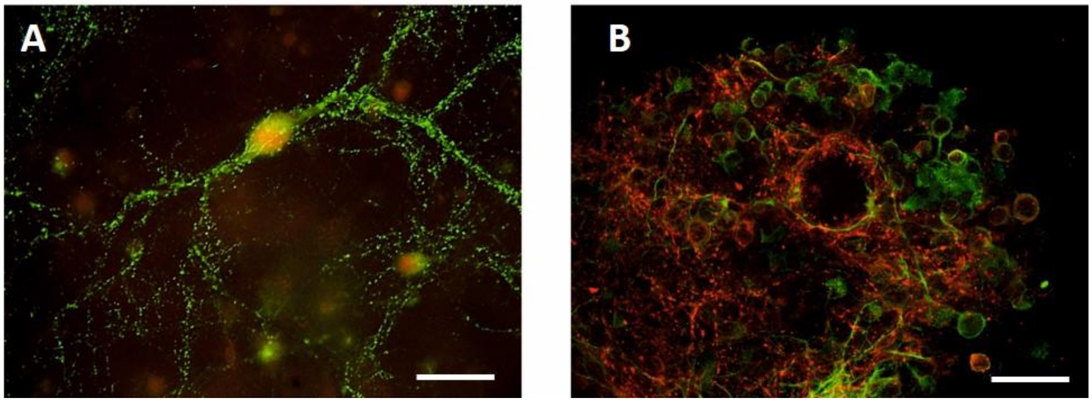

Figure 3.9 *(A) Neurons grown for 25 DIV on CHITO film marked for the pre-synaptic antibody vs Synapsin (green) and NeuN (red); Scale bar: 20 µm. (B) Neurons grown for 25 DIV on CHITO film marked for vesicular GABA transporter, VGAT (red) and vesicular glutamate transporter, VGLUT (green); Scale bar: 50 µm.*

These results confirm that CHITO naturally promotes adhesion, neurite growth and structural development of the network, even without any treatment with a.p.. Overall, both treated and untreated films were able to sustain the growth and development of cells over three-four weeks, with the formation of a stable network. Furthermore, in order to confirm chitosan bioaffinity, it was observed the morphological development of the neuronal network onto treated and untreated chitosan films neutralized and cross-linked with genipin. Both non-pretreated CHITO films were able to support neuronal growth during a period of more than 15 days (**figure 3.10 A-B**). In all cases, cell behavior is similar showing a homogeneous distribution and a dense network.

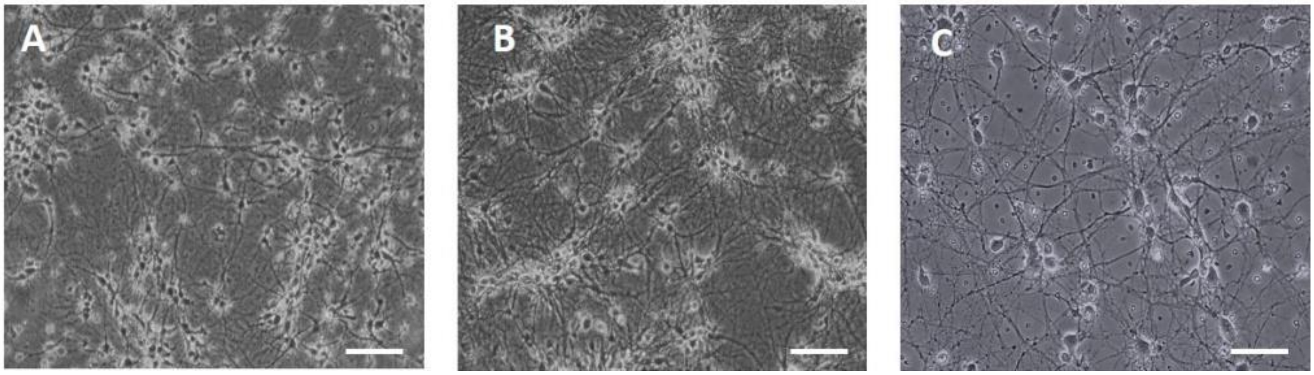

Figure 3.10 *Optical contrast phase images of 2D films neuronal network at DIV 15, CHITO film untreated with adhesion proteins (a.p.), (left); CHITO-Genipin film untreated with a.p.(middle); CHITO membrane coated with a.p. (right); Scale bar: 50 µm.*

In order to quantify the composition of the cells population during the in vitro network development on untreated film, a percentage variation of both the neuronal and glial population has been evaluated, according to the method described by Brewer et al. In this method, the serum-free medium is used, which allows the development and survival of hippocampal neurons at low levels of glial cells presence. Moreover, it should be considered that hippocampal cultures are typically derived from late stage embryonic tissues. This prenatal condition concurs in minimizing the growth of glial cells.

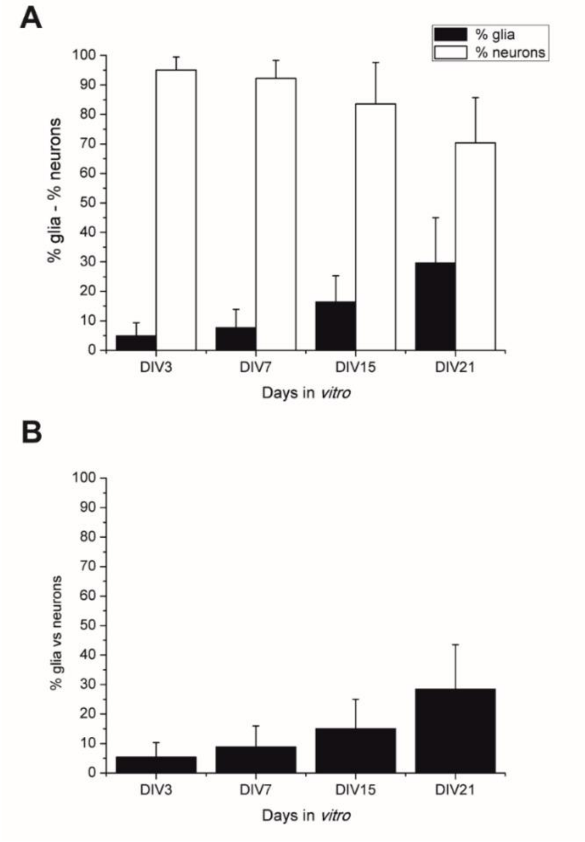

Figure 3.11 *Immunostaining for GFAP and NeuN to distinguish the two different populations. (A) The population of neuron and glia at DIV 3, 7, 15 and 21. (B) Percentage variation of glia vs neurons at DIV 3,7,15,21.*

In conclusion, while the glial population is present in our culture, its quantity never exceeds that of the neuronal population. Our starting population (DIVs 3) was determined by immunostaining (GFAP and NeuN) to be around 95,06 % neurons and 4,94% glia. The population of neuron and glia was determined also at DIVs 7, 15 and 21 (**figure 3.11**).

3.4.3.1 Characterization of 2D neuronal networks on chitosan as a cell adhesion factor

For the adhesion assay, cells at low density (28-30 cell/mm^2) were plated onto poly-ornithine and chitosan in the presence of astrocyte- conditioned medium. Plating efficiencies on the different substrates were determined in two experiments by counting at two different step (4 and 24 h) the total number of cells attached to the culture substrate in at least 10 visual fields per experiment, **figure 3.12**.

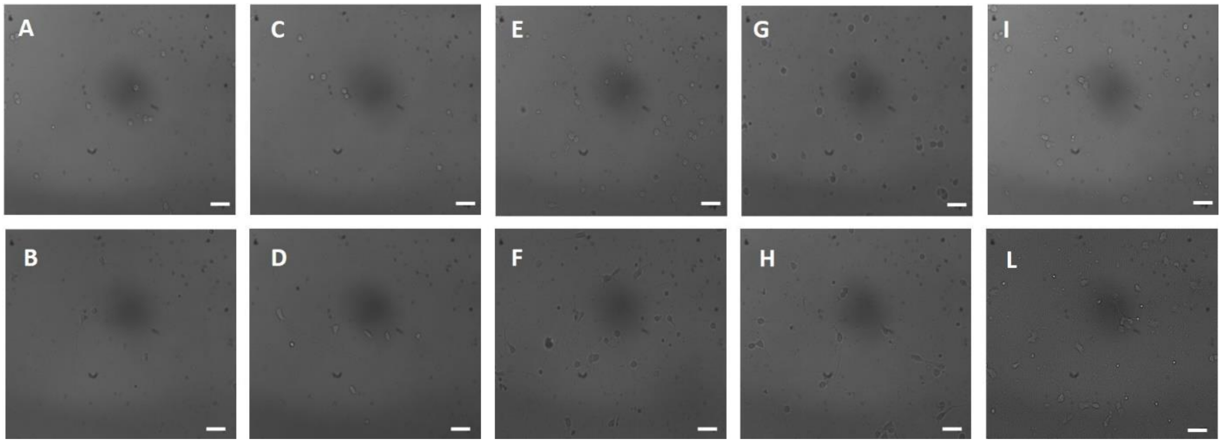

Figure 3.12: *Optical images of hippocampal neurons at 4h and 24 on CHITO at 0.01% (A-B), 0.05 % (C-D), 0.1 % (E-F), 0.5% (G-H) and on PORN substrates (I-L) Scale bar: 30µm.*

The number of cells attached after 4 and 24h on CHITO 0.01%, 0.05%, 0.1%, 0.5% and PORN are reported in **figure 3.13**.

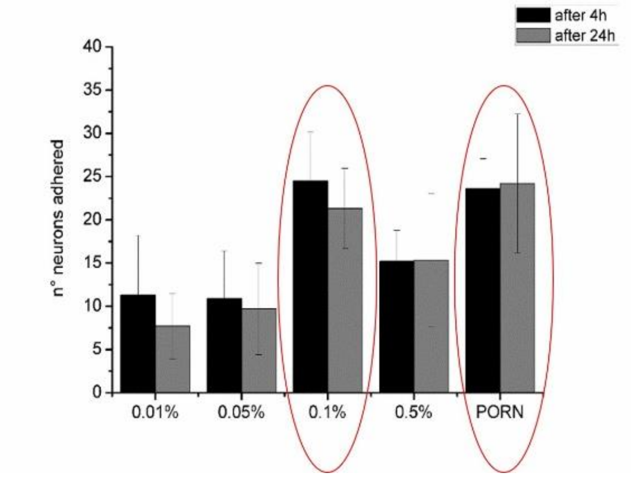

Figure 3.13 *Plating efficiency, n° neurons adhered after 4h and 24h on different CHITO concentrations substrates and PORN. There is nt signgnificant statistical differences between the two substrates at different time points.*

Individual cells in low-density cultures were selected, observed after 4h, 24h, 48h, and 72h in culture onto chitosan and poly-ornithine. ImageJ and NeuronJ have been used to analyze, trace and measure neuritic processes, **figure 3.14**.

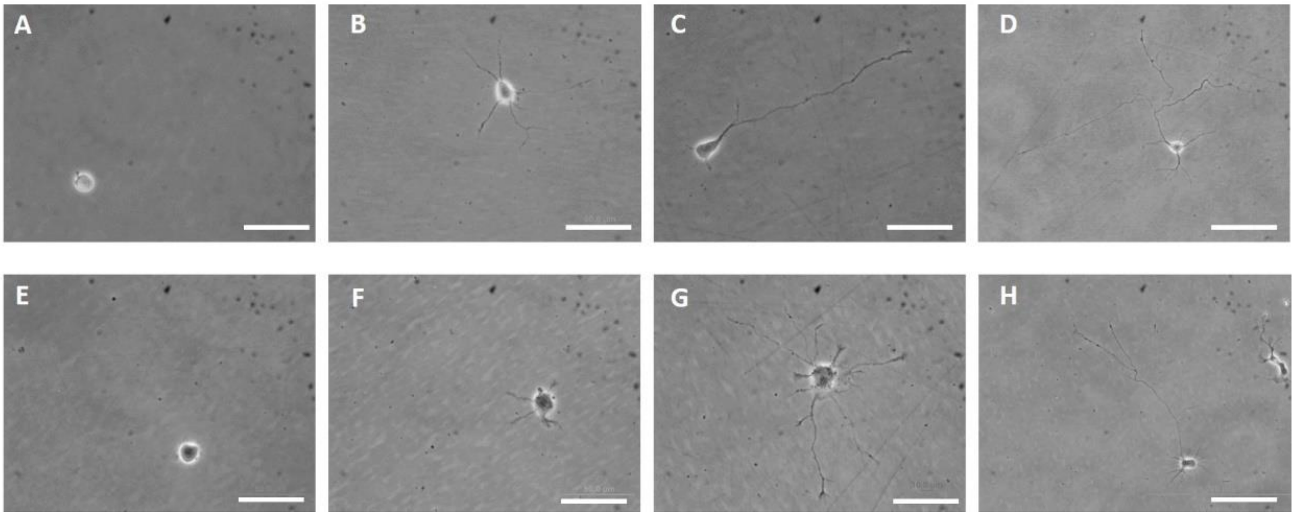

Figure 3.14 *Stages of neuronal development, A-D) Optical images of hippocampal neurons at 4, 24, 48, 72 hours on spray coating 1% CHITO 1L and onto PORN (E-F). Scale bar: 50µm.*

The cells reported in **figure 3.14** show the same basic series of developmental changes. To compare the two substrates, the number of neurites per cell, the average neurites length per cell and the length of the major neurite and the total length of minor neurites per cells at different stages 4h, 8h, 24h, 72h were evaluated. The number of neurites per cell, increased during the whole culture period (**figure 3.15A**). Neurons were maintained onto both CHITO and PORN substrates, the proportion of cells with neurites increased only during the first 24 hr of culture, after 4 hr in culture, less than 5% of cells maintained on PORN substrate (control) had developed neurites instead 90% on CHITO substrates. On the CHITO substrate, after 4 h, the average total neurite length is almost twice than the control, 15.41±6.59 (CHITO) and 7.49±3.43 (PORN).

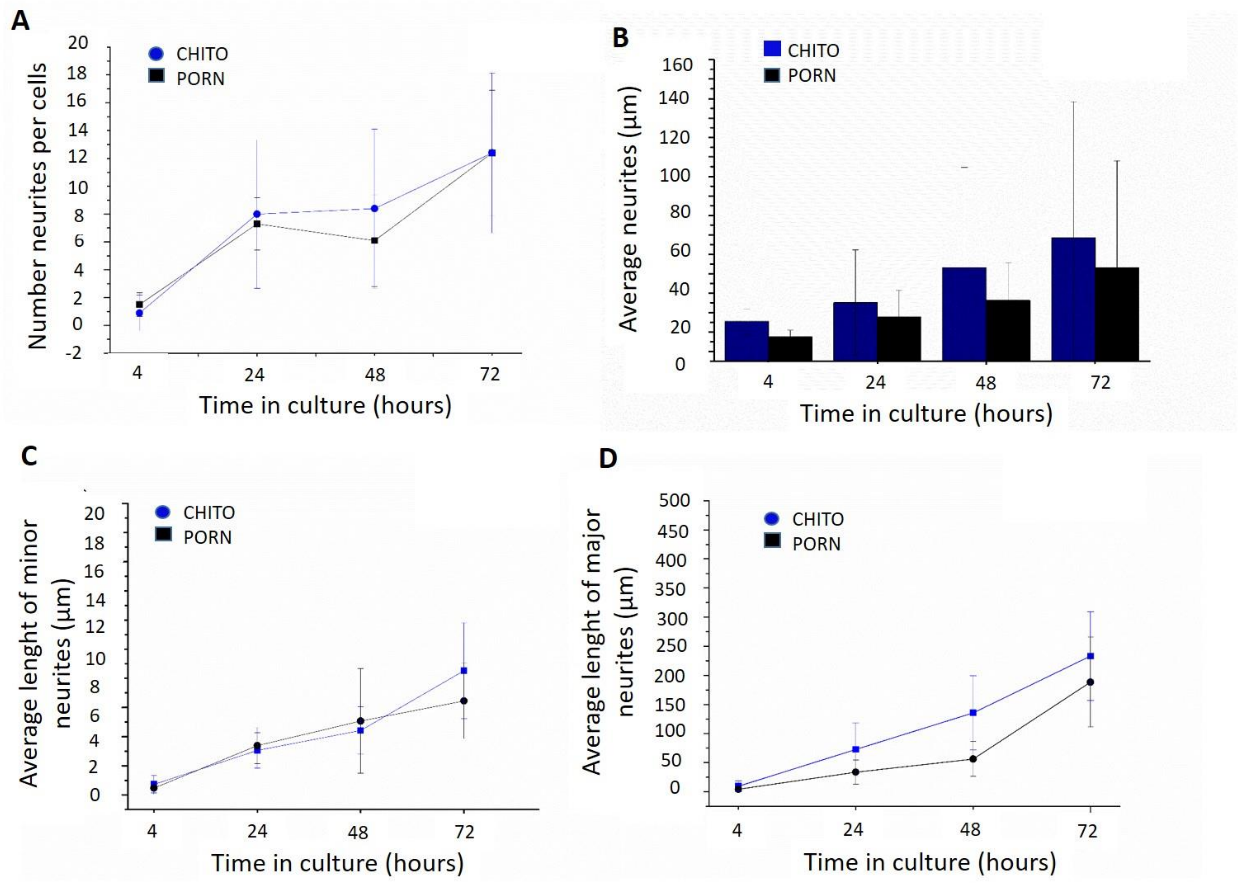

Figure 3.15 *Time dependence of the effects of substrate-bound chitosan on neurite lengths. Cells were maintained for 4, 24, 48, 72hr in culture, and the length of all neurites of process-bearing cells was measured for neurons on the control substrate (PORN) and on chitosan (CHITO). Results show the number of neurites per cells (A), the average lengths of all neurites (B), the average lengths of major neurites per cell (C), the total lengths of minor neurites (C).*

Observing the cultures during the first 72h, the neurites length increased steadily with time on both CHITO and PORN substrate (**figure 3.15B**). To investigate polar growth, that is, asymmetric growth of axonal versus dendritic compartments, the longest neurite of a given cell (major neurite) was measured separately from the minor neurites of this cell (**figure 3.15 C, D**). Onto PORN substrates, the growth of minor neurites was faster than growth of major neurites. Instead, the growth of major neurites onto CHITO substrates was faster than the minor ones (**figure 3.15C**)..

Differentiation is the establishment of the two distinct classes of neuronal processes, axons and dendrites. Because they are differentially distributed, microtubule-associated proteins (MAPS) might be considered prime candidates to regulate the spatial control of microtubule function during neuronal development. In the processes of mature neurons, MAP-2, is preferentially localized in dendrites, whereas TAU, is preferentially localized in axons. At the time that hippocampal neurons become polarized, however, MAP-2 and TAU are not differentially distributed; both are present in the axon and in the minor processes. To identify the major neurites as axons and the minor neurites as dendrites, the hippocampal cultures were stained for MAP-2, TAU and Akirin G (axon initial segment) to study their localization during early stages of axonal and dendritic development. Images, in **figure 3.16 A-L,** show hippocampal neuron development onto chitosan and poly-ornithine coatings, in according with Banker's model figure 2.

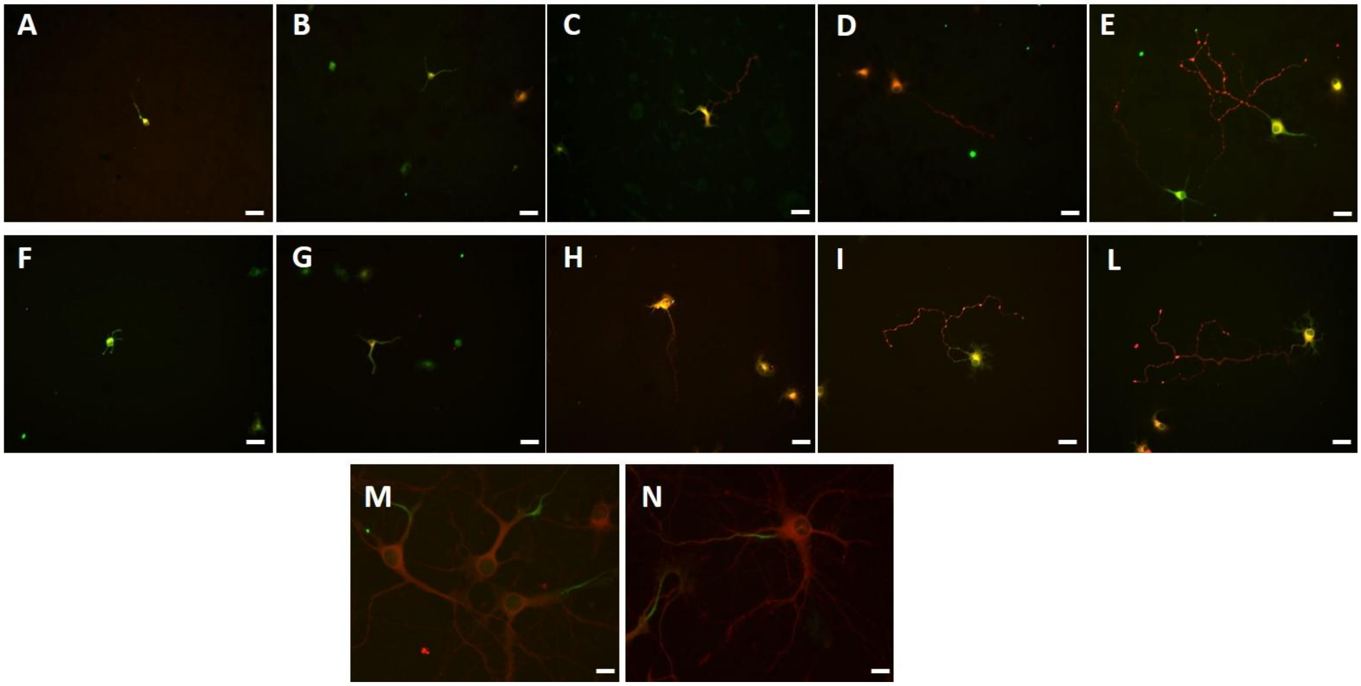

Figure 3.16 *A-E) Hippocampal culture development on spray-coating chitosan staining for MAP-2 (green) and TAU (red) at 4, 24,72 hours 5 and 7 days in vitro; F-L) hippocampal culture development on poly-ornithine staining for MAP-2*

(green) and TAU (red) at 4, 24,72 hours 5 and 7 days in vitro. Scale bar: 20 µm. M-N) Hippocampal culture development on spray-coating chitosan staining for AnkG (green) and TAU (red) at 72 h in vitro. Scale bar: 10 µm.

Despite the double staining, during the first stages in culture (4-24 h), processes were still immature and it was difficult to differentiate neuritic processes in axons or dendrites, due to the overlap of the markers. After 3 days in vitro, axons and dendrites were well-differentiated and the distribution of these two proteins was found to be quite different. Finally, after 72 hours in culture, it can be observed that 90 % of neurons grown onto both chitosan and poly-ornithine present the major process, much higher than 80 µm, consistent with the data provided by Banker. As a result, the average growth rate of the longest neuritic process was calculated.

The average growth rate for poly-ornithine is higher than for chitosan between 24 and 48 hours, while between 48 hours and 72 hours the speed is higher for chitosan than for poly-ornithine. The growth values are expressed in µm/h. The data described is visible in **Table 3.1**, Banker affirm that from the second day in culture, it is possible to distinguish axon, this one growth at an average speed of 60 µm/d. It can be observed that from the second day in culture, the average daily growth rate onto PORN substrate is very close to that provided by Banker, instead in the case of CHITO, it is higher.

	CHITO	***PORN***
$[24 \div 48]h$	$2{,}65\ \mu m/h$	$0{,}96\ \mu m/h$
$[48 \div 72]h$	$4{,}12\ \mu m/h$	$4{,}16\ \mu m/h$

Table 3.1 *Average growth rate in µm/h.*

Finally, the average growth rate, expressed in µm/d, of the longest neuritic process has been mesaured. The data described are visible in **Table2**.

	CHITO	***PORN***
$[24 \div 48]h$	$63{,}70\ \mu m/d$	$23.20\ \mu m/d$
$[48 \div 72]h$	$98{,}9\ \mu m/d$	$99.89\ \mu m/d$
$average\ growth\ rate$	$81{,}3\ \mu m/d$	$61{,}5\ \mu m/d$

Table 3.2 *Average growth rate in µm/d.*

3.4.6 Patterned film

In each sample it is possible to observe the square pattern according to the geometry of the mask. As can be seen in figure 13, the pattern outlined by the cells, is in accord withthe geometry of the mask and the low cell density allowed a fairly homogeneous distribution throughout the available area, with the exception of the edges where cell clusters can be seen. By enlarging area, it is possible to observe that all the cells communicate with each other and the neuronal network has developed.

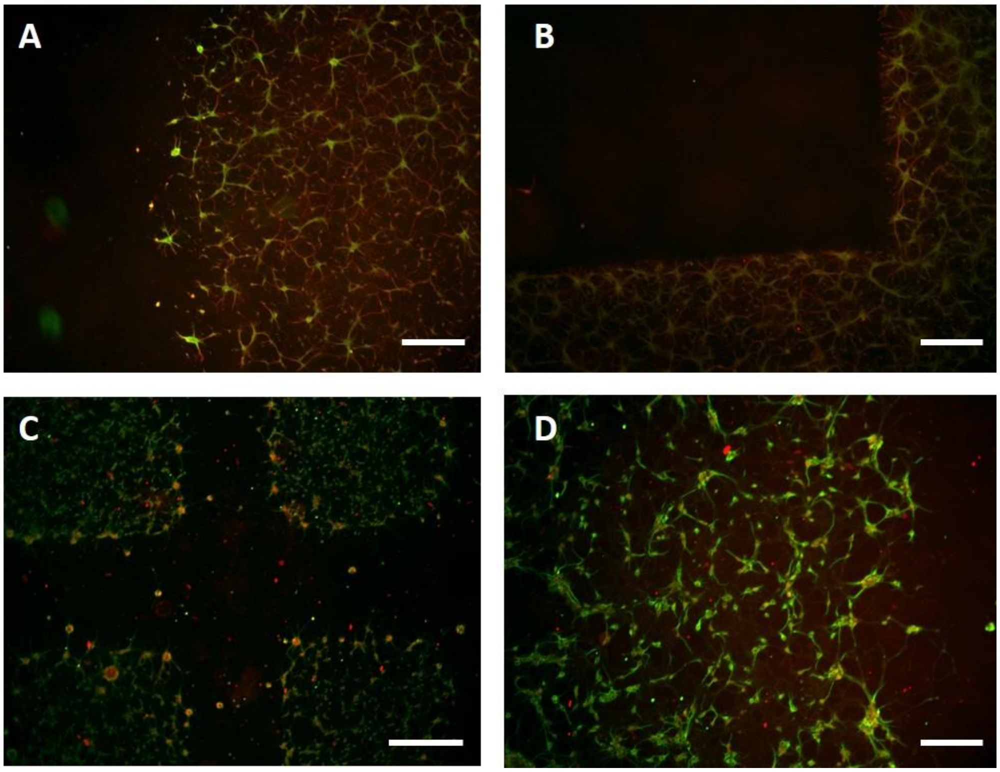

Figure 3.17 *2D neuronal network on CHITO patterned film, Hippocampal culture development on spray-coating chitosan patterned film staining for MAP-2 (green) and GFAP (red). Scale bar:500 µm.*

A preliminary spray coating macro-pattern test showed that neurons were homogeneously distributed only on the area coated by 1% chitosan 1L film, following perfectly the spray patterned, **figure 3.17**.

3.4.6 Functional characterization of 2D networks.

The electrophysiological activity of 2D cortical neuronal networks onto HD-MEA was recorded from DIV 19 to DIV 30 from hippocampal cultures and from DIV 15 to DIV 30 form cortical neurons, in order to obtain a functional development characterization.

.

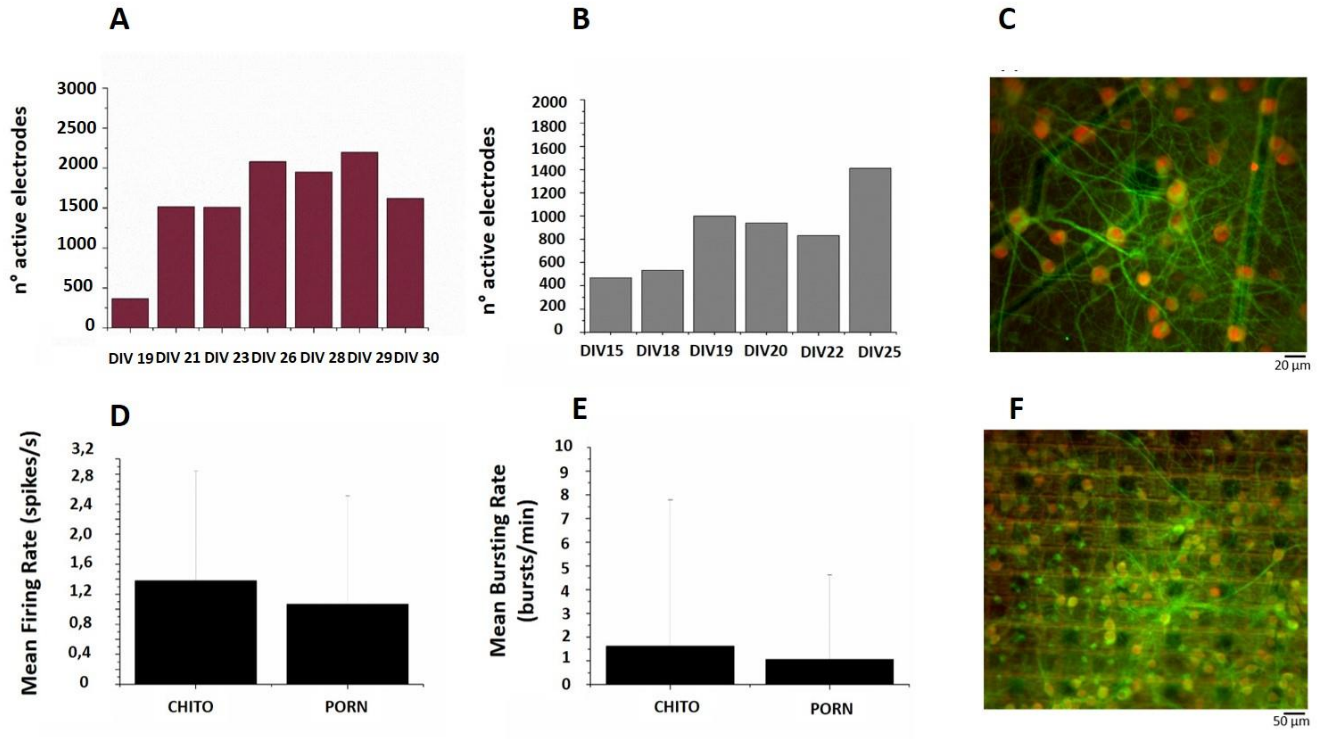

Figure 3.18: *(A) number of active electrodes (hippocampal culture), (B) number of active electrodes (cortical culture), (C) Neuronal culture development on CHITO substrate on MEA staining for MAP-2 (green) and NeuN (red) at DIV 24, scale bar: 20 µm; (D) Comparison of mean firing rate between 2D neuronal networks developed on CHITO and PORN substrates at DIV 22, (E) Comparison of mean bursting rate between 2D neuronal networks developed on CHITO and PORN substrate at DIV 22. (F) Neuronal culture development on CHITO substrate on HD-MEA staining for MAP-2 (green) and NeuN (red) at DIV 24, scale bar: 50 µm.*

The number of active electrodes increases up to triplicate at DIV 25, **figures 3.18 A** and **B**, for both types of cultures. The Mean firing rate and mean bursting rate were evaluated for 2D neuronal networks growth on both chitosan and poly-ornithine substrates. In **figures 3.18 D-E** a comparison between the main parameters extracted from 2D networks on both substrates at DIV 22 is reported. This comparison displays not significantly differences between the neuronal activity on CHITO and PORN. Chitosan coating on both devices, supports the development of a dense and highly connect networks, as it can see in **figures 3.18 C** and **D**

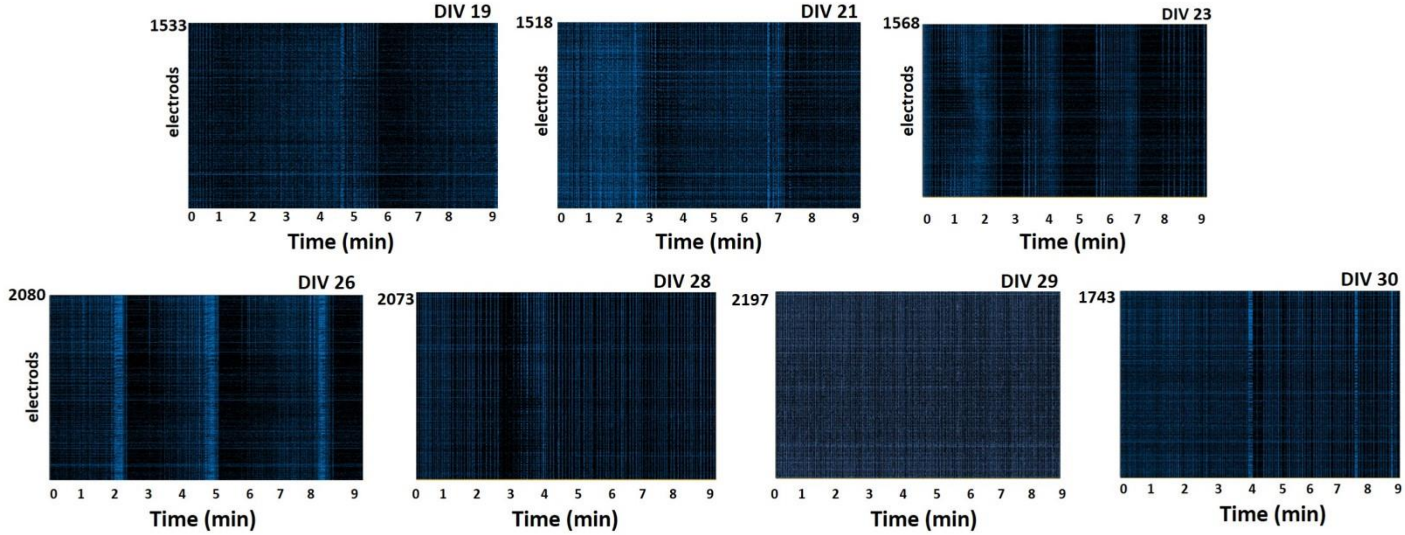

Figure 3. 19 *Spontaneous activity characterization of hippocampal cultures: (A) Raster plot showing 10 min of spontaneous activity of 2D network on CHITO substrates from DIV 19 to DIV 30.*

A quasi-synchronous network bursts (NB) were mixed with random spiking activity from DIV 19 to DIV 21. The 2D culture exhibited a global activity characterized by long bursts at DIV 23, that became completely synchronous from DIV 29, **figure 3.19**.

3.5 Discussion

In the effort of investigating the intrinsic bioaffinity of CHITO, we firstly characterized its ability to induce cell attachment and neurite outgrowth without any pre-treatment with adhesion proteins. As a first step, this characterization was carried out using standard 2D cell culture models onto the surface of CHITO films. Quite surprisingly, non-pre-treated CHITO films neutralized and cross-linked with genipin were able to support neuronal growth during a period of more than 15 days. A similar observation was previously done for soft alginate hydrogels, which were able to support neural cell cultures in monolayer or spheroids [19,20]. However, the use of alginate as supporting material for neuronal cultures is controversial, since it requires Ca_2+ ions for its ionic cross-linking and it is well known that neurons and glial cells are extremely sensitive to Ca_2+ ions, even at nM concentrations [21]. To our knowledge, this is the first work reporting the ability of pure CHITO to support neuronal cell attachment and functional neuronal network development. This represents a valuable contribution in the search for low-cost biomimetic culture systems, which can have important applications in neuropharmacology, toxicology, and regenerative medicine [22,23]. Individual cells, in low-density cultures were selected and observed after 4h, 24h, 48h, and 72h in culture onto chitosan and poly-ornithine substrates. The cells in **figure 14** follow the basic developmental changes of the Barker's model. The number of neurites per cell increased during the first 24 hr of culture on both control and chitosan coatings, **figure 3.15A**. On chitosan substrates, 4h after plating, the cells developed the first neuritic processes more than on the control one, where cells without neuritic processes were more than 70%. On both substrates, the proportion of cells with neurites increased steadily until 24 hr, when it all neurons bearing processes. Between 24 - 48h, the number of neurites per cell on chitosan and on poly-ornithine did not increase further, leading to significantly lower values on chitosan than under control conditions. Then, a strong increase was observed after 48h when the numbers of neurites per cell on control and chitosan substrates reached similar values, **figure 3.15A**. Furthermore, the total length of all neurites per cell increased steadily with time on both substrates, but chitosan showed higher values than poly-ornithine, **figure 3.15B**. Both chitosan and poly-ornithine affect neurite outgrowth in a manner dependent on the culture time. The total length of minor neurites per cell was higher on the control substrate during the first 48 hr of culture and this result has been supported also by the fact that PORN substrates showed the highest number of neurites per cell, **figures 3. 15 A-C**. However, the growth of major neurites was slower than the growth onto CHITO substrate, **figure 15D**. The total length of minor neurites on chitosan substrates increased in accord to the rapid growth in the number of neurites after 48h, **figures 3.15 A-C**. Chitosan thus favored growth of major neurites over growth of minor neurites and therefore increased neuronal polarity at later stages of neuritogenesis, **figure 15D**. After 72 h in vitro, axons and dendrites were well-differentiated and the distribution of MAP-2 and TAU confirmed this thesis. In all cases, petri dishes, MEA and HD-MEA coated with 1% chitosan 1L were able to support neuronal growth and cell behavior was similar showing a homogeneous distribution and a dense network, **figure 3.18 C** and **F**. In addition, the same data were compared with the data provided in the literature, taking into account that the neurons studied by Banker were grown on poly-lysine substrates. By comparing the average growth of the longest neuritic process of neurons grown on CHITO and PORN substrates with the data provided by Banker, it is possible to affirm that the neuritic process growth mode depends on substrate types. The growth of the major process on PORN (black) is gradual and very similar to the model describied by Banker for poly-lysine-grown neurons (magenta) and this is not surprising given the similarity between PORN and poly-lysine as growth factors. For the neurons grown on CHITO (green), at 24h and 48h, the behavior is similar to PORN and poly-lysine, while at 72h it is completely different**, figure 3.20**.

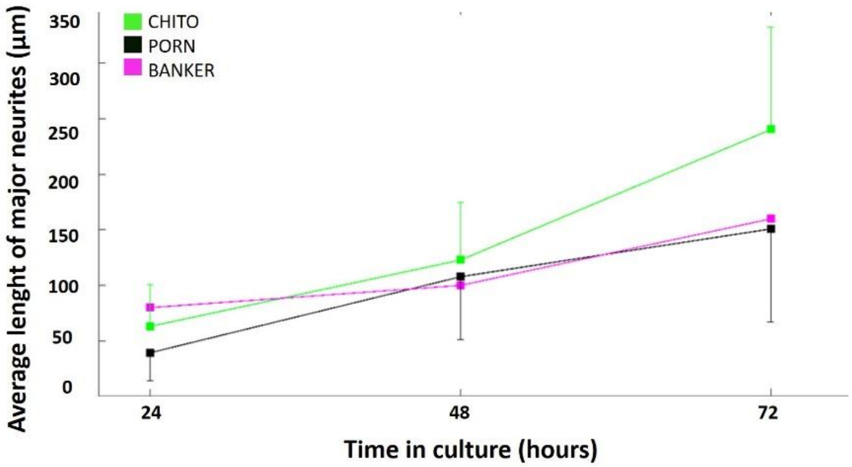

Figure 3.20 *Comparison of the effects of substrates, CHITO, PORN and poly-lysine on the length of major neurites.*

The standard methods for the functionalization of supports used for 2D cell cultures are based on the use of poly-lysine and PORN, which generally have a high cost. These macromolecules containing amino groups, have been frequently used as coating materials for in vitro neuronal substrates, as electrostatic attraction between the positive charges of the NR_3^+ groups on a culture substrate and the negatively charged neuronal membranes has been suggested as an indispensable factor for stable neuronal adhesion and proper development. In this work, CHITO has been introduced as an alternative adhesion factor used to support neuronal culture. CHITO can behave as a poly-cation under acidic conditions (pH<6), due to the protonation of free amino groups, showing along the chains NR_3 + groups in a similar way of that one present along the standard macromolecules, **figure 3.21**.

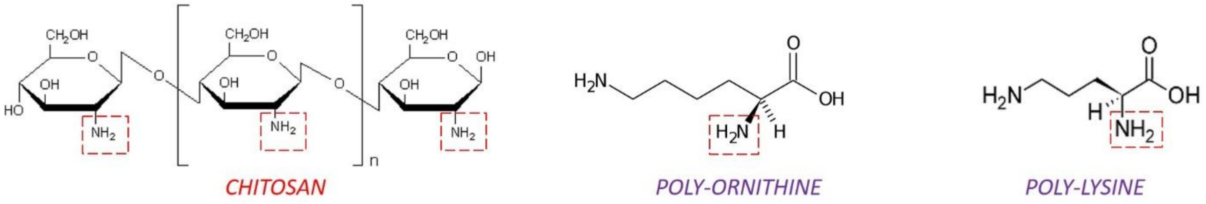

Figure 3.21. *Chemical structures of Chitosan, poly-ornithine and poly-lysine.*

3.6 Conclusions

The 2D cultures growth onto chitosan films were investigated in the view of gain information on the bioactivity of chitosan in terms of cell adhesion ad network development. We demonstrated that the natural and low-cost polysaccharide chitosan possesses excellent processability, film forming properties and more importantly bioactivity towards all tested neuronal populations. The spray-coating technique, through a conventional airbrush, was selected as coating method since it is widely recognized as a versatile, high-speed and easy technique for coating thin layers onto virtually any kind of substrates, giving also the possibility of producing a desired micropattern through the use of stencil masks. The use of the chitosan as adhesion factor leads to the development of a homogeneous, dense and highly connected electrically active network. The main advantages of this disclosure are related to the speed-up of the supports preparation before cell seeding, with the possibility of preparing micropatterned surfaces and finally to the reduction of laboratory reagents costs.

Chapter 4

Chitosan– based microbeads scaffold for 3D neuronal networks

This chapter was adapted from the following publication:

Tedesco. MT et al, "Soft chitosan microbeads scaffold for 3D functional neuronal networks".

Biomaterials. 2018

4.1 Chitosan microbeads scaffolds

In literature is reported that hydrogel structure can be modified to take the form of a granular structure, better replicating the structure of brain tissue. This multiphase structure encompasses hydrogel granules surrounded by an ECM rich secondary phase into which cells are seeded. Granular hydrogels readily fluidize when compressed, a property known as shear thinning [179]. This increases the injectability of this systems. Cells can be mixed homogeneously whit hydrogel granules, which act as a protective medium that supports cell viability during delivery. In a stem cells delivery therapy for traumatic brain injury, a microsphere chitosan hydrogel scaffold functionalized whit heparin to bind FGF-2 was shown to support radial glial cell (RGC) delivery when injected into a rat brain contusion model [180]. Moreover, granular scaffolds have also been found to facilitate cell infiltration and promote vascularization in-vivo. In a recent work, chitosan microspheres based scaffold was implanted into a rat spinal cord injury model and the granular hydrogel was found to elicit a dynamic restorative process, promoting axon outgrowth, vasculature ingrowth and diminishing fibrous glial scarring and the inflammatory response [181]. Chitosan microspheres have been produced via different techniques as spray drying [182,183], emulsification [184], internal gelation [185,186], electrospinning and freeze drying processes.

4.2 Aims

Physically and covalently cross-linked chitosan microbeads were then fabricated by an aerodynamically assisted jetting technique, characterized by optical and atomic force microscopies (AFM) and then used as scaffold for 3D hippocampal neuron cultures. The 3D neuronal networks were characterized morphologically by transmission electron microscopy (TEM), by immunofluorescence techniques and 3D imaging with a confocal microscope. The spontaneous electrophysiological activities of the obtained

3D networks were recorded after 21 days of in vitro culture (21 DIV); results were compared with those obtained using glass microbeads [187] as 3D scaffold for neuronal growth.

4.3 Materials and methods

Materials

Chitosan (CHI) solution: CHITO (medium molecular weight, 75-85% deacetylated, code 448877, lot MKBD4275V, from Pandalus Borealis), was dissolved in 0.1 M acetic acid at concentrations 1% and 2% w/v under continuous stirring for two hours and filtered through a syringe filter (5µm) to remove any undissolved material.

*Neutralizing solution***:** H_2Odd 40%, Ethanol 60% and sodium hydroxide 2% w/v

Genipin solution: genipin 2% in H_2O_{dd}

Laminin: P-D-Lysine (1:1) solution: concentration of 0.05 mg/ml in sterile water

Filtered CHITO solutions were extruded using a microencapsulation unit (Nisco Encapsulation Unit VAR J30) equipped with a conical nozzle having a diameter of 0.25 mm [32], figure 22. The extrusion flow rate was 0.4 ml/min under 100 mbar pressure for 1% CHITO, whereas for 2% CHITO the extrusion flow rate was 0.5 ml/min under 200 mbar pressure. The generated micro-droplets were collected into 150 ml of gelling solution bath while continuously stirring at 200 rpm. The distance from the nozzle to the gelling solution was set at 6 cm. The resulting microbeads were left in contact with the gelling solution for 30 min at room temperature to ensure complete solidification. Afterwards, the gelling solution was removed through. The production yield was evaluated using optical microscopy. An inverted optical microscope (IX-51 Olympus microscope equipped with a DP70 digital camera and with a 10X N.A. 0.25 PhC objective) was used to take images of the microbeads. From the collected images, after binarization, the “analyze articles tool” of ImageJ software (NIH, USA) was used to evaluate the projected areas of the microbead. Areas of particles touching each other were separated by watershed segmentation.

4.3.1 Nisco Encapsulation Unit VAR J30

The J30 is the aerodynamically assisted jetting equipment shown on the **figure 4.22**. The product enters through a central needle. The exit orifice, which is centrally in line with the axis of the needle, has been counter-sunk externally. The counter sunk leads to the aero dynamical effect so that the jet has a smaller diameter when passing the orifice than before at the needle. The needle is enclosed in a pressure chamber with an exit through the orifice. The size of the drops is determined by the product *flow rate* and the *pressure* inside the chamber. The product flow rate is typically controlled by a syringe to be connected to the product nozzle. The pressure in the pressure chamber is controlled by the specifically for the J30 developed Nisco pressure control unit consisting of a pressure sensor and a digital indication. The pressure set point can be fixed with a potentiometer.

Parameters to be monitored for the process optimization are Flow rate, nitrogen pressure, type of nozzle (100, 250, 350, 500, 1000 μm), distance between nozzle and neutralizing solution, speed of stirrer.

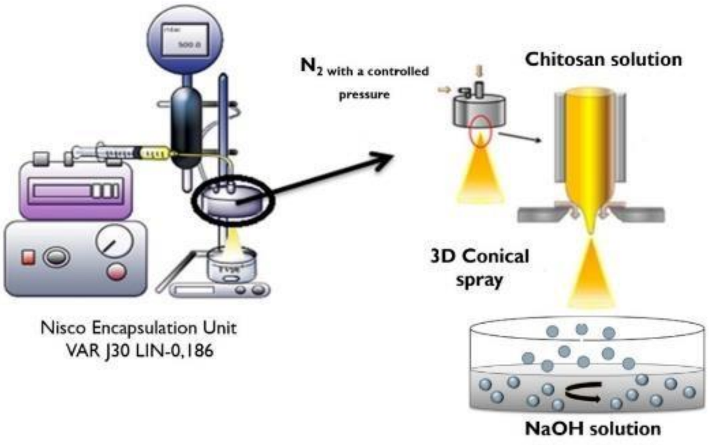

Figure 4.22 *Nisco Encapsulation Unit VAR J30.*

The generated micro-droplets were collected into the gelling bath while continuously stirring. The resulting microbeads are left in contact with the gelling solution for 30 min at room temperature to ensure complete solidification. Afterwards, the gelling solution was removed through centrifugation (1000 rpm for 5 min), followed by four washing steps in distilled water.

In our case, chitosan films and microbeads were synthetized by physically and chemical cross-linking:

Phase-inversion, using neutralization solution (H_2O_{dd} 40%, Ethanol 60% and NaOH 2% w/v)

$$CHITO\text{-}NH_3 + OH \rightarrow CHITO\text{-}NH_2 + H_2O$$

Covalent cross-linking, using a naturally crosslinking agent genipin. Genipin is extracted from the fruit of the gardenia plant. Chemical crosslinking is achieved by the covalent bond between two chitosan primary amines through one genipin molecule (**figure 4.23**). Chemical crosslinking of chitosan by genipin leads to the formation of secondary amide and heterocyclicamino linkage [175].

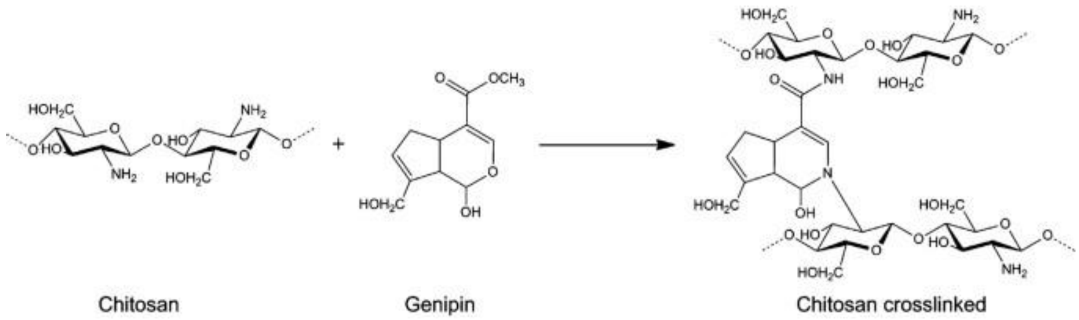

Figure 4.23 *Covalent crosslinking of CHITO cross-linked with genipin.*

Before the covalent cross-linking with genipin, 1% CHITO films and microbeads are neutralized by NaOH solution. The prepared CHITO films and microbeads are, respectively, immersed in the genipin solutions for crosslinking (12h). followed by four washing steps in distilled water.

4.3.2 Cell preparation

Hippocampi were dissected and removed from embryonic Sprague-Dawley rats at gestational day 18 under sterile conditions. Hippocampal fetal tissue was enzymatically digested in Trypsin 0.125% in Ca++ and Mg++ free Hank's (Gibco Invitrogen) for 20' at 37°C. The enzymatic process was quenched by adding culture medium supplemented with 10% of FBS (Sigma-Aldrich) then the tissue was mechanically dissociated with a smoothly fire-polished Pasteur pipette. Neurons were re-suspended in plating medium consisting of Neurobasal medium (Gibco Invitrogen) with 2% w/v B-27 Supplement (Gibco Invitrogen), 1% Glutamax (Gibco Invitrogen), 1% Pen-Strepto (Gibco Invitrogen). Cultures were maintained in incubator at 37°C in a 5% CO2, 95% humidity atmosphere for 3-4 weeks by replacing half of the medium once a week. The experimental protocol was approved by the European Animal Care Legislation (2010/63/EU), by the Italian Ministry of Health in accordance with the D.L. 116/1992 and by the guidelines of the University of Genova. All efforts were made to reduce the number of animals used for the project and to minimize their suffering.

4.3.3 Characterization of chitosan microbeads

The mean particle size and size distributions were evaluated using optical microscopy. The mean particle size was evaluated using ImageJ software as described above. To perform SEM imaging, microbeads were freeze-dried and then coated with carbon using a Polaron E5100 sputter coater.

4.3.3.1 Water content

2.5x106 microbeads in 0.5 ml of water were weighed inside an Eppendorf tube and were then lyophilized. The weight of the dried microparticles was measured and the water content was calculated using the following equation, where Ws is the weight of hydrated microbeads and Wd is the weight of the lyophilized ones:

$$\text{Water content} = ((\text{Ws} - \text{Wd}))/(\text{Ws})) \times 100\%$$

4.3.3.2 Atomic Force Microscopy (AFM)

A commercial atomic force microscope, equipped with a closed loop scanner capable of 9 μm vertical range (Keysight Technologies, model 5500ILM), was used to measure both the topography and the stiffness of the microbeads. Rectangular micro-cantilevers (Mikromash HQ: CSC38, type B, nominal spring constant k=0.03 N/m) either with a conical tip or without any tip were employed. Images of the topography of single beads were obtained in contact mode, by careful adjusting the lowest possible force to keep the contact during the whole scan. In order to evaluate the stiffness of the beads, standard force curves were recorded and the region after contact was considered for further analysis. The applied load for cantilever deflections was calculated by first converting the output voltage, from the AFM four-segment photodetector, into nanometers of deflection, and then by multiplying the deflection by the cantilever spring constant. The conversion factor was calculated by taking several force curves onto a hard glass substrate each time the laser spots on the cantilever had to be adjusted, and by considering the reciprocal of the average slope of the constant compliance region of the curves. When using sharp conical tips, the load versus indentation curve was evaluated to extract the elastic modulus of the sample using the model proposed by Oliver and Pharr [188] as already described in [189]. When using tipless cantilevers the load versus microbead deformation curve was evaluated in order to extract the stiffness of the bead in analogy with unconfined compression testing. All measurements were performed at a constant approaching/retracting speed of 1 mm/s. This allowed us to compare results, despite the viscous (i.e. speed-dependent) response of the CHITO microbeads. In order to take into account intra-sample heterogeneity, 16×16= 256 force curves were recorded over a regular grid over a 5×5 μm.

Microbeads were adsorbed onto the surface of a petri dish pre-modified by the deposition of a layer of polyethylenimine (PEI 1mg/ml in pure water, from Sigma Aldrich), followed by a layer of polystyrene sulfonate (PSS 2mg/ml, Sigma-Aldrich). For both samples, three maps of 16×16 curves were collected onto three different microbeads randomly selected over the petri surface.

4.3.3.3 Preparation of 3D networks on CHITO microbeads

The day before plating, microbeads were sterilized by exposure to ethanol 70% for 2h. The sterilized samples were then washed with sterile water 5 times, normalized in cell culture medium and used for the cell culture experiments. To evaluate the bioaffinity between CHITO and neurons, cultures were prepared using both microbeads treated and untreated with adhesion proteins (a.p.).

In the first case, microbeads were exposed to a mix of a.p., namely Laminin: P-D-Lysine (1:1) solution, and left in the incubator overnight at 37°C. The microbeads were centrifuged three times, for 5 min at 1000 rpm. Each centrifugation step was followed by a washing step in sterile water. In the second case, microbeads were sterilized and used without any further treatment. Before cell plating, microbeads were washed in a Neurobasal medium and then exposed to the cell suspension in complete Neurobasal medium; the ratio of the number of microbeads to the number of neurons was nominally 1:4. Eppendorf vials were used for this step; 10^6 microbeads/ml and $4x10^6$ cells/ml were mixed and after an interval of around 3-4 hours they aggregated and formed small clusters. The vials were kept in horizontal position and turned for 12-16 times at 20-25 min intervals in order to expose the whole microbead surface to the suspended cells. At the end of the incubation-adhesion phase, the neuron-microbead aggregates were left to deposit slowly at the bottom of the vial. Finally, they were carefully collected with a micropipette in small volumes (30-35µl), and directly transferred onto standard petri dishes (Ø35mm) for subsequent immunocytochemistry characterization, or plated onto the MEA surface for electrophysiological characterization. The day before plating, MEAs were assembled with donuts-shaped Poly-dimethyl-siloxane (PDMS) structures (internal and external diameters: 5 and 22 mm respectively, height: 650 µm) to confine the self-assembled microbeads and neurons onto a circular surface of 20 mm^2 around the active electrodes area (**figure 4.24A**). MEAs (assembled as explained above) were sterilized in the oven at 120° for 2 hours. At the end of the sterilization process, the chips were treated only on the area delimited by the PDMS structure, with a mix of a.p. namely Laminin: P-D-Lysine (1:1), at the concentration of 0.05 mg/ml in sterile water (L-2020; P-6407 Sigma) and left in the incubator overnight at 37°C. The coating solution was removed from the MEA which was then washed twice with water and left to dry under the laminar hood until the plating took place. Similarly, to what performed in [187], hippocampal neurons without microbeads were first plated onto the MEA surface to create a first monolayer of cells at a final concentration of 800-1000 cell/mm^2. 3-4 hours after plating, 30-35 µl of neuron-microbead aggregates were transferred inside the PDMS confinement structure onto the area on which hippocampal neurons were previously seeded (**figure 4.24B**). Around 4.5x10^4 microbeads and 1.5x10^5 cells were transferred into MEAs.

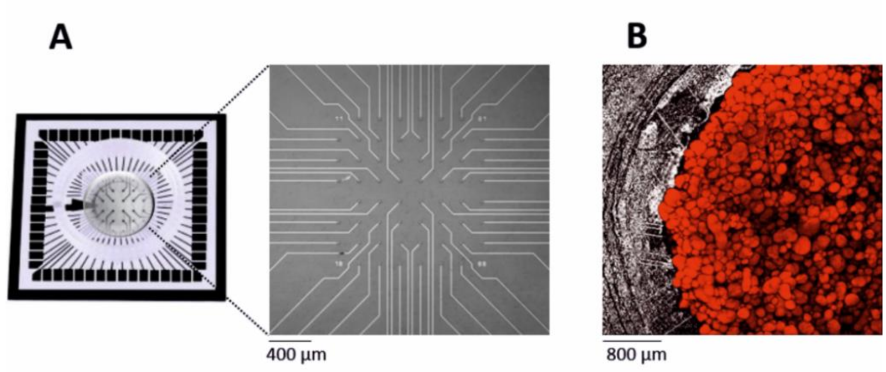

Figure 4.24 *Set-up configuration, (A) Micro-electrode arrays (MEAs) made up of 60 planar microelectrodes (TiN/SiN, 30 mm electrode diameter, 200 mm spaced) arranged over an 8 X 8 square grid with inserted PDMS (internal diameter 5 mm) constraint on the active area; (B) 3D CHITO scaffold macroscale assembly onto MEA labeled for MAP-2.*

4.3.3.4 Morphological characterization of 3D neuronal networks by transmission electron microscopy

In order to analyze the samples with Transmission Electron Microscopy (TEM), the 3D networks on CHI 2% were fixed for 2 hours in a fixative solution (2% Glutaraldehyde, in buffer Na-Cacodylate 0.1M) and then post-fixed (2h) in a solution 1% OsO4, 1,5% Potassium Hexacyanoferrate, in Na-cacodylate buffer 0.1M. Subsequently, they were stained overnight in a 1% Uranyl acetate aqueous solution and dehydrated with series of alcohols. TEM samples were infiltrated with Propylene Oxide and low viscosity Spurr resin (SPI-Chem). Once the resin hardened, 70 nm thick sections were cut with a Leica EMU C6 ultra-microtome. TEM images were collected by means of Jeol JEM 1011 (Jeol, Japan) TEM, operating at an acceleration voltage of 100 kV, and recorded with a 11 Mp fiber optical charge-coupled device (CCD) camera (Gatan Orius SC-1000). All used reagents were from Sigma-Aldrich.

4.3.3.5 Morphological characterization of neuronal networks by immunocytochemistry

To assess the expression of specific neuronal markers, hippocampal cultures were fixed in 4% paraformaldehyde in phosphate buffer solution (PBS), pH 7.4 for 30 min at room temperature. Permeabilization was achieved with PBS containing 0.5% Triton-X100 for 15 min at room temperature and non-specific binding of antibodies was blocked with an incubation of 45 min in a blocking buffer solution consisted of PBS, 0.3% BSA (bovine serum albumin Sigma) and 0.5% FBS. Cultures were incubated with primary antibody diluted in PBS Blocking buffer for 2 hours at room temperature or incubated at 4°C overnight in a humidified atmosphere. Cultures were rinsed three times with PBS and finally exposed to the secondary antibodies. The following primary antibodies were used for CHITO microbeads: MAP-2 1:500 (monoclonal or polyclonal Synaptic System), TUBULIN βIII, clone TU-20 (similar TUJ1) 1:500 (Chemicon Millipore), NeuN 1:200 (Chemicon Millipore), Dapi 1:10000 (Sigma). Cultures were rinsed twice with PBS and finally exposed to the secondary antibodies: Alexa Fluor 488, Alexa Fluor 549, Alexa Fluor 633 Goat anti mouse or Goat anti rabbit, diluted 1:700 and 1:1000 (Invitrogen Life Technologies S. Donato Milanese).

To observe the perineuronal net-like structure, we exposed samples to Wisteria floribunda 1:200 (Sigma-Aldrich) as primary antibody for 24h and Streptavidin Alexa Fluor 488, 1:700 (Invitrogen Life Technologies S. Donato Milanese) for 6h as secondary antibody.

4.3.3.6 Optical microscopy and confocal imaging

An inverted IX-51 Olympus microscope equipped with a DP70 digital camera coupled with CPlan 10X N.A. 0.25 PhC objective was used to acquire contrast phase images of CHI microbeads coupled with neurons. An Olympus BX-51 upright microscope was used for immunofluorescence evaluation of the biological samples and the image acquisition was done with a Hamamatsu Orca ER II digital cooled CCD camera driven by Image ProPlus software (Media Cybernetic).

Confocal imaging was acquired on two different microscopes: Leica TCS SP5 AOBS Tandem DMI6000 inverted microscope coupled with objective Leica IRAPO 25X, 0.95 NA (Leica Microsystems, Mannheim, Germany) and Leica TCS SP5 AOBS Tandem DM6000 upright microscope coupled with objective Leica IRAPO 25X, 0.95 NA (Leica Microsystems Srl, Italy). Data were analyzed by means of the LASX V2.0 software (Leica Microsystems Srl, Italy).

4.3.3.7 MEA recording and analysis

The spontaneous electrophysiological activity of 3D hippocampal neuronal networks was recorded at 21-24 days in vitro (DIV) by means of micro-electrode arrays (MEAs) made up of 60 planar microelectrodes (TiN/SiN, 30 µm electrode diameter, 200 µm spaced) arranged over an 8 X 8 square grid (except the four electrodes at the corners), supplied by Multi Channel Systems (MCS, Reutlingen, Germany). The electrophysiological activity was acquired with the 2100 System (MEA 2100-System, MCS), and signals were sampled at 10 kHz. Recordings were performed for 30 min outside the incubator at a temperature of 37 °C. To prevent evaporation and changes of the pH medium, a slow flow of humidified gas (5% CO2, 20% O2, 75% N2) was constantly delivered during the measurement sessions into a small plastic box covering the experimental MEA setup.

4.3.3.8 Data and Statistical analysis

Data analysis was performed by using a custom software package named SPYCODE [176], developed in MATLAB (The Mathworks, Natick, MA, USA). Spike detection was performed by using the Precise Timing Spike Detection (PTSD) algorithm [177]. The algorithm requires three parameters: a different threshold set to 8 times the standard deviation of the baseline noise, a peak lifetime period (set at 2 ms) and a refractory period (set at 1 ms). To characterize the electrophysiological activity, we extracted some first order statistics. In particular, we evaluated the mean firing rate (MFR), i.e., the number of spikes per second of each channel and the percentage of random spikes, i.e., the fraction of spikes outside bursts. We also performed burst detection according to the method described in [178]. A burst is a sequence of spikes having an ISI (inter-spike interval, i.e., time intervals between consecutive spikes) smaller than a reference value (set at 100 ms in our experiments), and containing at least a minimum number of consecutive spikes (set at 5 spikes). The parameters extracted from this analysis are the mean bursting rate (MBR) and the mean burst duration (MBD), which are the frequency and the duration of the bursts at the single channel level respectively. The same approach used for the detection of bursts was applied for the detection of quasi synchronous events at network level called network bursts [176]. The extracted parameters are the network bursting rate (NBR) and the network burst duration (NBD), which are the frequency and the duration of the bursts at global net level respectively.

Statistical analysis was carried out using OriginPro 8 (OriginLab Corporation, Northampton, MA, USA). All data are presented as mean ± standard error of the mean. Statistical analysis was performed using a non-parametric Kruskal-Wallis test, since data do not follow a normal distribution (evaluated by the Kolmogorov-Smirnov normality test). Differences were considered statistically significant when $p < 10^{-3}$. In order to determine which of the sample pairs are significantly different, post-hoc test, using Dunn's test, has been applied.

4.4 Results

4.4.1 Preparation and characterization of CHITO microbeads

1% and 2% CHITO microbeads were prepared and characterized in view of their use as scaffolds for neuronal growth. The instrumental parameters, for microbeads production, were optimized in order to promote the formation of the micro-droplet spray and to avoid aggregation of microbeads on the air/gelling solution interface. The production yields were evaluated to be around 0.9×10^6 and 0.7×10^6 per batch for 1% and 2% CHITO respectively. Optical microscopy images of the obtained samples were acquired and analyzed. The results indicated a spherical shape and a size ranging from 40 to 90 µm, with an average diameter of 66 ± 20 µm, for 1% CHITO, while for 2% CHITO the size ranged from 40 to 160 µm, with an average diameter of 100 ± 40 µm**, figures 4.25 A-B**. Water content values were found to be 98.4% and 99.3% for 2% and 1% CHITO microbeads, respectively.

AFM topography showed nanometer sized features onto a rounded profile. The elastic modulus of the microbeads was first evaluated by AFM indentation measurements using microcantilevers with conical tips. The elastic modulus measured on 2% CHITO microbeads was in the range 15-25 kPa, whereas 1% chitosan microbeads were too soft to reliably determine the point of contact and, thus, to calculate the elastic modulus.

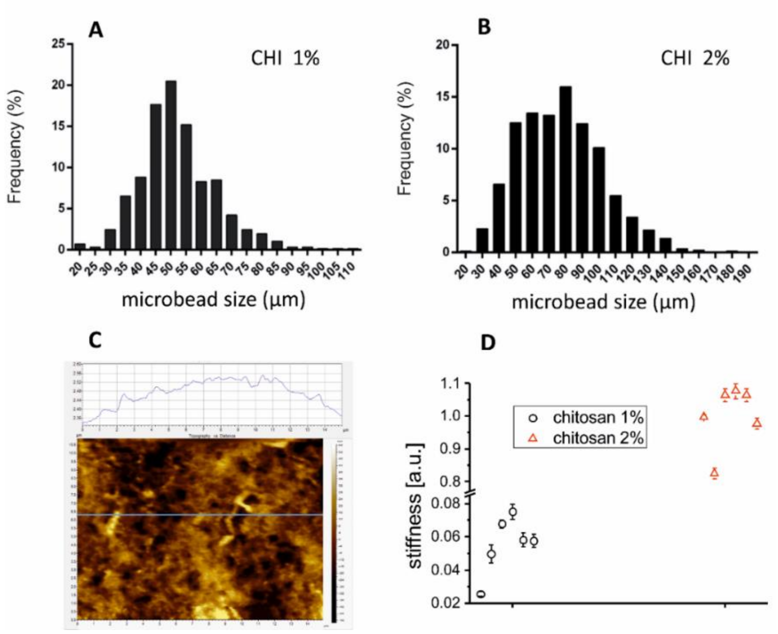

Figure 4.25 *Characterization of CHITO microbeads, (A) Histogram of the distribution of 1% CHITO microbeads size; (B) Histogram of the distribution of 2% CHITO microbeads size; (C) Topography AFM image (second order flattened) of 15 X 15 mm^2 of a single 2% CHITO microbeads in culture medium, the insert shows the profile of the raw data from a single line (blue line); (D) Stiffness values measured by AFM on 1% and 2% CHITO microbeads.*

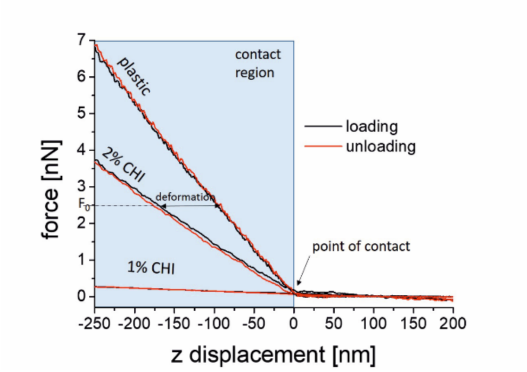

Figure 4.26 *Three representative AFM force-distance curves taken on 1%, 2% CHITO microbeads, and a reference hard surface, respectively, using a the same tipless cantilever. Both approach-loading and retract-unloading portions of the curves are plotted (black and red lines, respectively). A rather constant slope in the region after contact can be clearly observed for all curves. The lower slope when pressing against a CHITO microbead indicates that the bead deforms under the applied load. Such deformation can be calculated at any given force as indicated in the graph.*

Therefore, we used a tipless cantilever of the same type to press against a single microbead. The slope of the force curve after contact resulted constant for a wide range of applied forces (1-10 nN) and with negligible hysteresis between loading and unloading (**figure 4.26**). This slope represents the stiffness of the microbeads. Stiffness values obtained from the constant compliance region of curves performed on different microbeads using the same cantilever and the same approach-retract speed can be directly compared. In **figure 4.25D** average stiffness values measured on 1% and 2% CHITO microbeads are plotted. The values are normalized versus the average stiffness of 2% CHITO beads. 1% microbeads were found to be, on average, 18 fold softer than the average stiffness of the probed 2% microbeads. Interestingly enough, the range of the elasticity value for 1% CHITO microbeads that can be inferred by our measurements (1/18 of 15-25 kPa) falls in the same range of reported elasticity values for brain tissue (0.7-1 kPa) [190,191]. In addition, also, genipin-crosslinked microbeads were characterized. These microbeads shown a spherical shape and a size ranging from 120 to 140 µm. Water content values were found to be 96,8% The elastic modulus of the microbeads was in the range of 0,8-1 kPa.

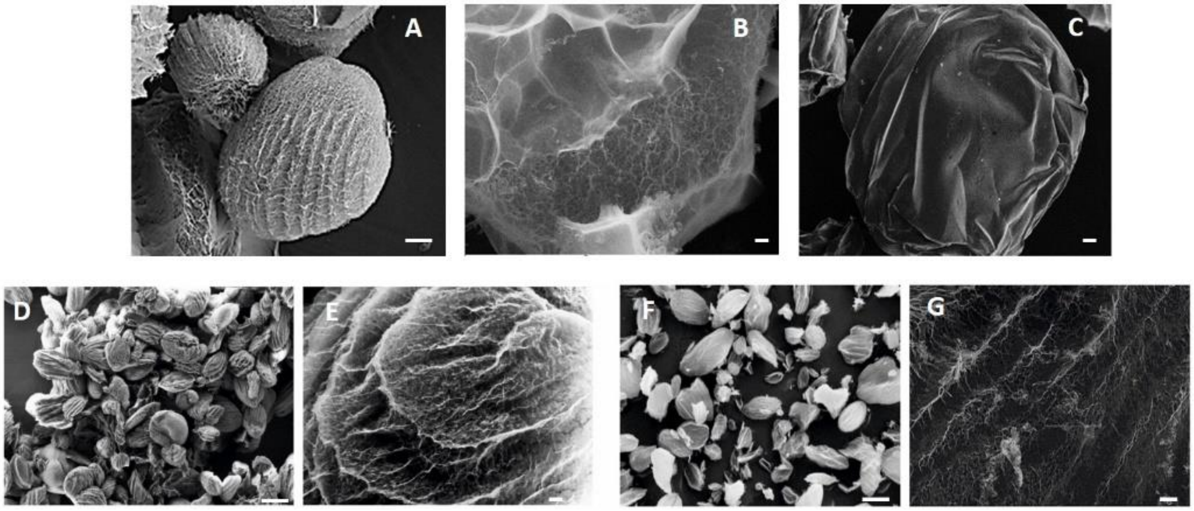

Figure 3.27 *FE-SEM images, (A) 1% CHITO microbead, scale bar: 20 µm; (B) 2% CHITO microbead, scale bar: 5 µm; (C) CHITO-genipin microbead, scale bar: 10 µm. (D) 1% CHITO microbeads, Scale bar: 100 µm; (E) zoom of 1%*

microbead surface, Scale bar: 2 μm; (F) 2% CHI microbeads, Scale bar: 100 μm; (G) zoom of 2% microbead surface, Scale bar: 2 μm.

The surface morphology was then characterized by FE-SEM (**figure 4.27**). 1-2 % CHITO microbeads show a surface rough and porous; instead, genipin-crosslinked microbeads have a compact and smooth surface.

4.4.2 Preparation and characterization of 3D neuronal networks on CHITO microbeads

As a first step, in order to verify the bioaffinity of CHITO also in the form of microbeads, cells were cultured onto CHITO microbeads both untreated and treated with a.p. The obtained 3D cultures were observed by contrast phase optical microscopy during the first two weeks of culture in vital conditions. In both cases, a branched and entangled expression of neurites and the presence of healthy neurons, which was demonstrated by the refractivity of the neuronal soma, were observed. All subsequent experiments were carried out onto 3D neuronal networks grown onto 1% and 2% CHITO microbeads pre-treated with a.p.. This was done in order to compare the properties of the 3D networks grown onto CHITO microbeads with the ones grown onto glass microbeads as described in [25]. TEM characterization was carried out in order to appreciate the interaction between CHITO microbeads and cultured cells. From low magnification imaging (**figure 4.28A**) it is clear that cells and microbeads (**marked with black asterisks**) create a dense network. Because of the electron microscopy staining, cell bodies and dendrites appear darker compared to the microbeads, allowing to observe that cells both envelop and penetrate the chitosan scaffold. Higher magnification images show more in detail the interaction among neurons and CHITO microbeads. **Figure 4.27B** shows a neuronal cell and its axon pushing out between two beads, meeting then the dendrites from another neuron.

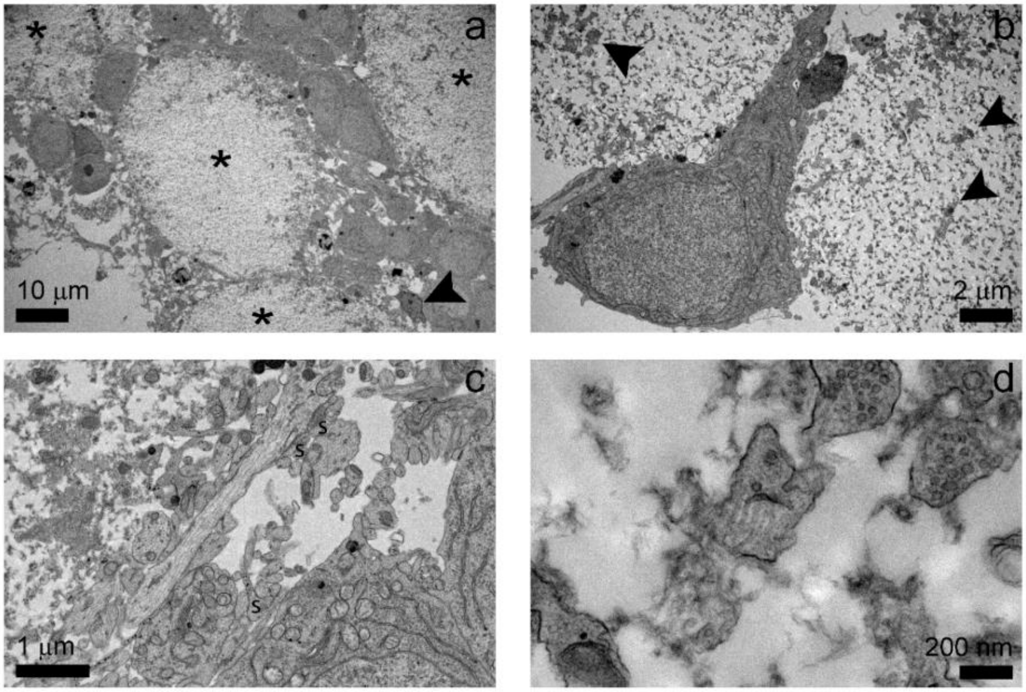

Figure 4.28 Low-mag TEM micrograph of a portion of chitosan scaffold with the neuronal network, (A) CHITO microbeads are marked with the asterisks, while cells appear darker, the dark arrow highlight a glial cell. (B) A neuron grown between two microbeads (1000x). The dark arrows indicate dendrites inside the chitosan. (C) A detail (2500x) of the interface cell-CHITO microbeads. Synapses are marked with the letter s. (D) High-mag (15000x) detail of dendrites taken far (15 mm) from the bead surface.

Besides this, it is clear how smaller dendrites enter inside the chitosan, as underlined by the black arrows. In **figure 4.27C** is reported a detail of the interface between cells and CHITO microbeads, where many neurons components are evident: cell bodies, axons with distinct tubulin cytoskeleton, small dendrites, spines and synapses. From these two images, it is clear that on the microbeads surface there is a dense network made up of axons and dendrites of different size, while only the smaller dendrites penetrate into the CHITO microbeads. **In figure 4.28D** is reported a detail of a dendrite taken far from the microbeads surface (about 15 µm). The size of these terminations is smaller (<400 nm), but they are clearly neural dendrites, as suggested by some details as the cytoskeleton and the vesicles.

Indirect immunofluorescence techniques were then used to assess the in vitro morphological and functional cell behavior and to characterize the 3D structure of the network. To this purpose, after 25 DIVs, at the end of the recording sessions, 3D cell-scaffolds were fixed with PFA 4% and labeled by using a panel of ad-hoc selected antibody molecules. The 3D neural networks were then characterized by confocal microscopy on MAP-2 labeled neurons and on MAP-2 and Tubulin βIII. Overall, the thickness of the 3D neuronal network on the 2% CHITO microbeads was evaluated to be around 300-500 µm. **Figure 4.29** shows the neuronal network development around the CHITO microbeads (**A, C**) and around glass microbeads (**B**). We can see (**figure 4.29A**, left and middle) neuronal soma from which rich neuritic arborizations depart. This is particularly evident around the CHITO microbead surfaces while it becomes partially fragmented due to the penetration of neurites into the microporous volume of the microbeads (white arrows). In the case of the glass microbeads, the neuronal network development was confined onto the surface of microbeads, without any fragmentation (**figure 4.29B, left**). Moreover, the shape of the soma was found to be spherical in both cases (**figures 4.29 A-B, middle**), as the one observed *in vivo* [25, 34]. **Figure 4.29A** (**right**) shows a section of the 3D culture where it is possible to observe the close assembly between CHITO microbeads mediated by neuronal cells. Instead, in the case of glass microbeads a hexagonal structure was observed characterized by well-defined and separated microbeads (**figure 4.29B, right**). **Figure 4.29C** left shows the structural proteins of the cytoskeleton of the 3D network on 2% CHITO microbeads. **Figure 4.29C** right shows the high density of synaptic puncta present on the 3D network. In the formation of brain-like constructs a pivotal role in the survival and differentiation of neurons is played by glial cells [36].

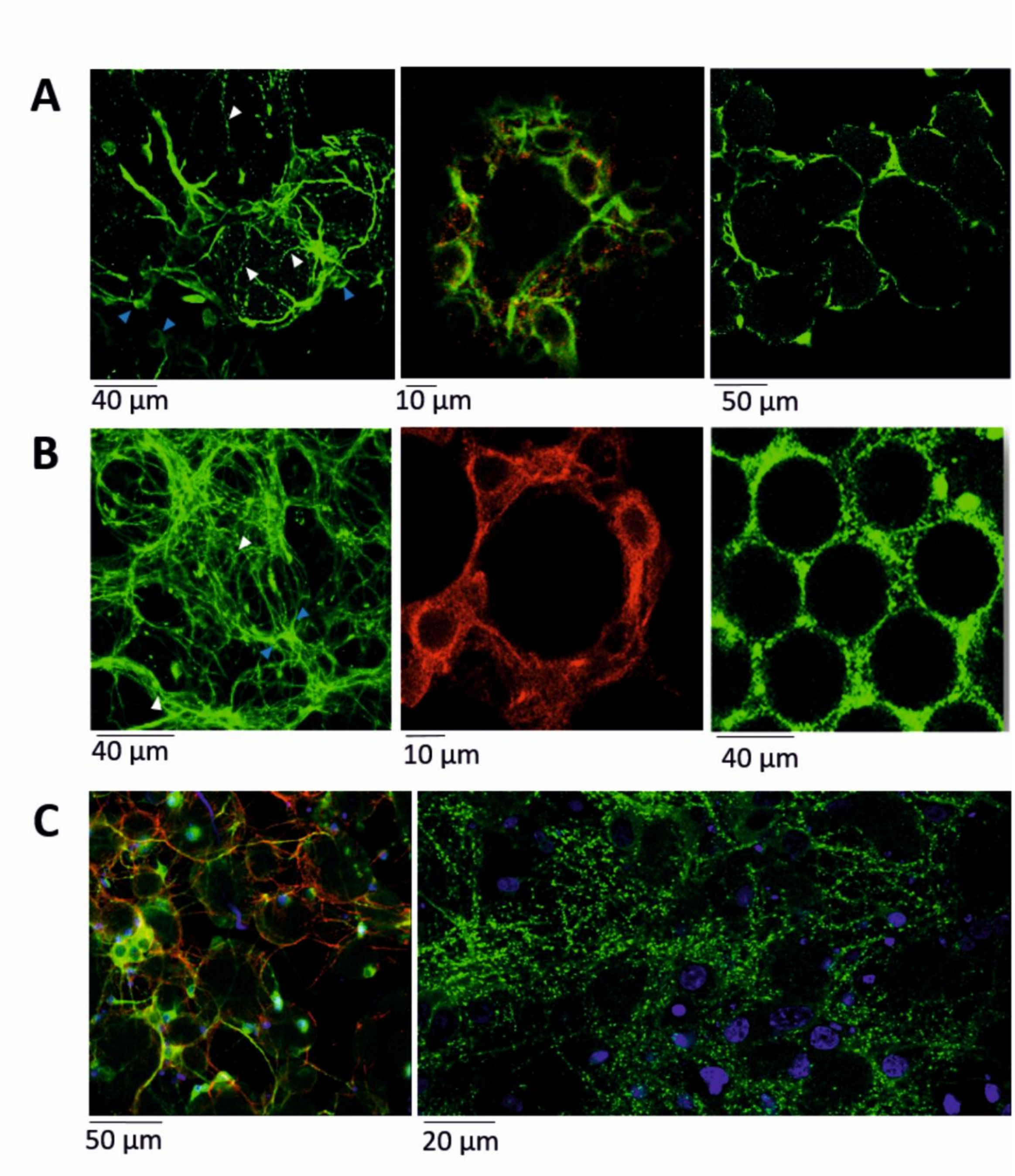

Figure 4.29 *Confocal microscope images of 3D neural network at DIV 25: (A) 3D neural network on 2% CHITO microbeads (left), single 2% CHITO microbead surrounded by almost six neurons (middle) and a section of 3D neural network on 2% CHITO microbeads (right), MAP-2 (green) and Synapsin (red). (B) 3D neuronal network on glass microbeads (left), single glass microbead surrounded by five neurons (middle) and a section of 3D neural network on glass microbeads (right), MAP-2 (green and red). The blue arrows point the cell soma while the white one points neuritic*

fragmentation. (C) 3D neural network on 2% CHITO microbeads (left) labeled for MAP-2 (green), Tubulin βIII (red) and DAPI (blue), 3D neural network on 2% CHITO microbeads (right) labeled for Synapsin (green) and DAPI (blue).

In order to highlight the morphology of glia cells, fixed 3D and 2D cultures were exposed to GFAP primary antibody followed by secondary antibody Alexa Fluor 549. It can be observed that the GFAP positive cells cultured both on 2D film and 3D microbeads 2% CHITO (**figures 4.30 A-B**) present a different morphology compared to GFAP positive cells cultured at the same conditions but on the 2D petri dish surface (**figure 4.30C**).

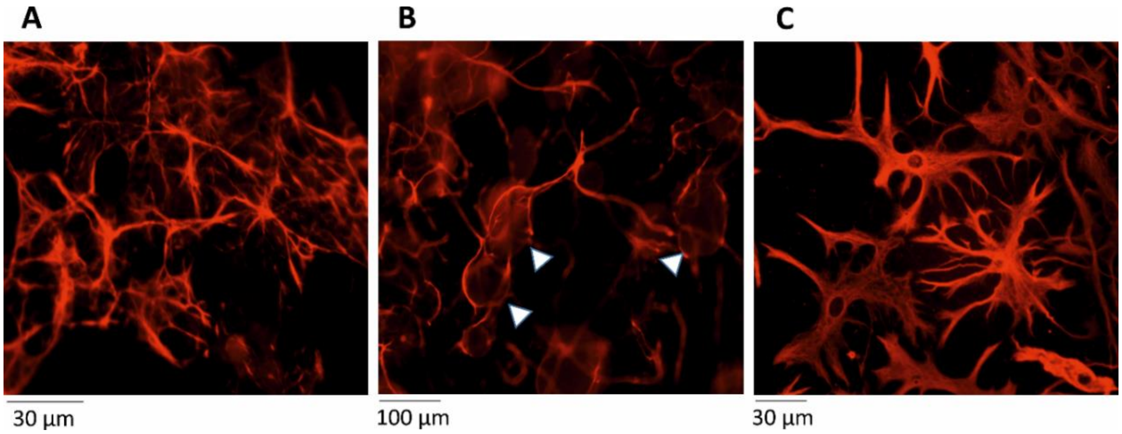

Figure 4.30 *Optical images of glial cells labeled for GFAP (DIV 25): (A) 2D network on CHITO film; (B) 3D network on 2% CHITO microbeads; (C) 2D network on petri dish. The white arrows point CHITO microbeads.*

These results suggest that the chemical and mechanical environments play a relevant role on the morphological behavior. Similar observations were already reported in previous works [35-40]. The 3D structure of neuronal networks after 24 days of culture fixed and immunolabeled for the dendritic marker MAP-2 is illustrated in **figure 4.31**.

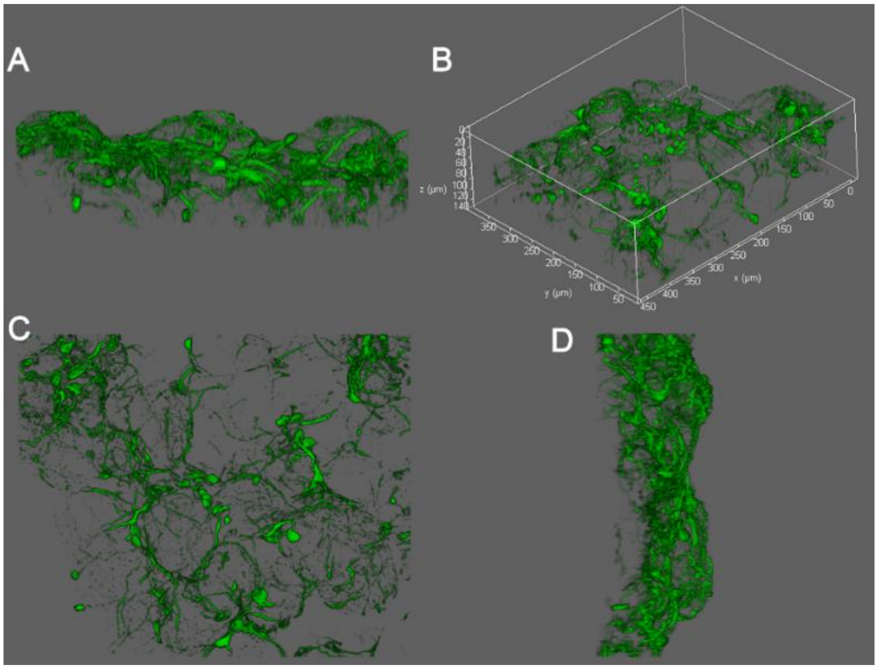

Figure 4.31 *Max intensity projection, Orthogonal View and Rendering 3D of population neurons network on the scaffold labeled (DIV 24) for MAP-2: Cross-sectioning along different axes XZ (A), XY(C), YZ (D); (B) Volumetric representation (XYZ) of neuronal networks from the same sample.*

.
Both the 3D reconstruction of 148 µm z-stack of the hippocampal network and the projections along different axes are shown, thus giving a comprehensive view of the neuronal network onto the CHITO microbeads scaffold (**figure 4.31B**). The max intensity projection of the orthogonal view is represented in this figure: XZ projection (**figure 4.31A**) shows CHITO microbeads profiles wrapped by neuronal network; **figure 4.31C** and **4.1D** show XY – YZ projections.

4.4.3 Functional characterization of 3D networks

In order to perform the electrophysiological characterization of the 3D networks grown onto CHITO microbeads and to compare the obtained results with the ones reported in [187], CHITO microbeads were pre-treated with a.p., then mixed with neurons and finally plated onto MEA. As reported in [187], before this final step, a 2D neuronal network was directly coupled to the active area of MEA in order to establish a good communication between the 3D culture and the underlying microelectrodes. **Figure 4.32** shows the spontaneous activity (raw signal) of 10 s of a 3D CHITO network as recorded from one microelectrode and characterized by two bursts and random spikes. The global electrophysiological behavior of representative 3D networks, is qualitatively showed in the raster plots of **figures 4.32B** and **C**, where 300 s of spontaneous activity are displayed. In both experimental conditions (CHITO, figure 32B and glass microbeads, **figure 4.32C**, quasi-synchronous network bursts (NB) are mixed with random spiking activity. However, 3D networks with CHITO microbeads scaffold exhibit a global activity characterized by longer bursts than glass microbeads ones. After 21 DIV, we recorded 30 minutes of spontaneous activity of n = 3 CHITO 1% networks, and n = 3 CHITO 2% networks, and we compared the obtained results to n = 3 cultures where the 3D scaffold was realized by means of glass microbeads. **Figures 4.32 D-I** show the parameters extracted from the analyzed spike data. CHITO 1% networks presented values of MFR (2.3±0.14 spikes/s), statistically different from the CHITO 2% ones (0.86 ± 0.05 spikes/s; $p < 0.\ 001$) but similar to the MFR of the 3D glass microbeads networks (2.97±0.55 spikes/s). All the 3D experimental configurations display high values of random spiking activity (**figure 4.32E**): specifically, CHITO 1% and 2% networks show higher (statistically significant) values with respect to glass microbeads ones. Regarding the bursting behavior, the MBR of CHITO 2% networks showed the lowest value (3.74 ± 0.31 (bursts/min)) which is significantly different ($p < 0.001$) from the CHITO 1% and glass microbeads networks. (ms)) significantly higher ($p < 0.001$) than the other two configurations that share similar MBD values (175.10 ± 16.41 ms and 190.70 ± 10.53 ms for CHITO 2% and glass microbeads).

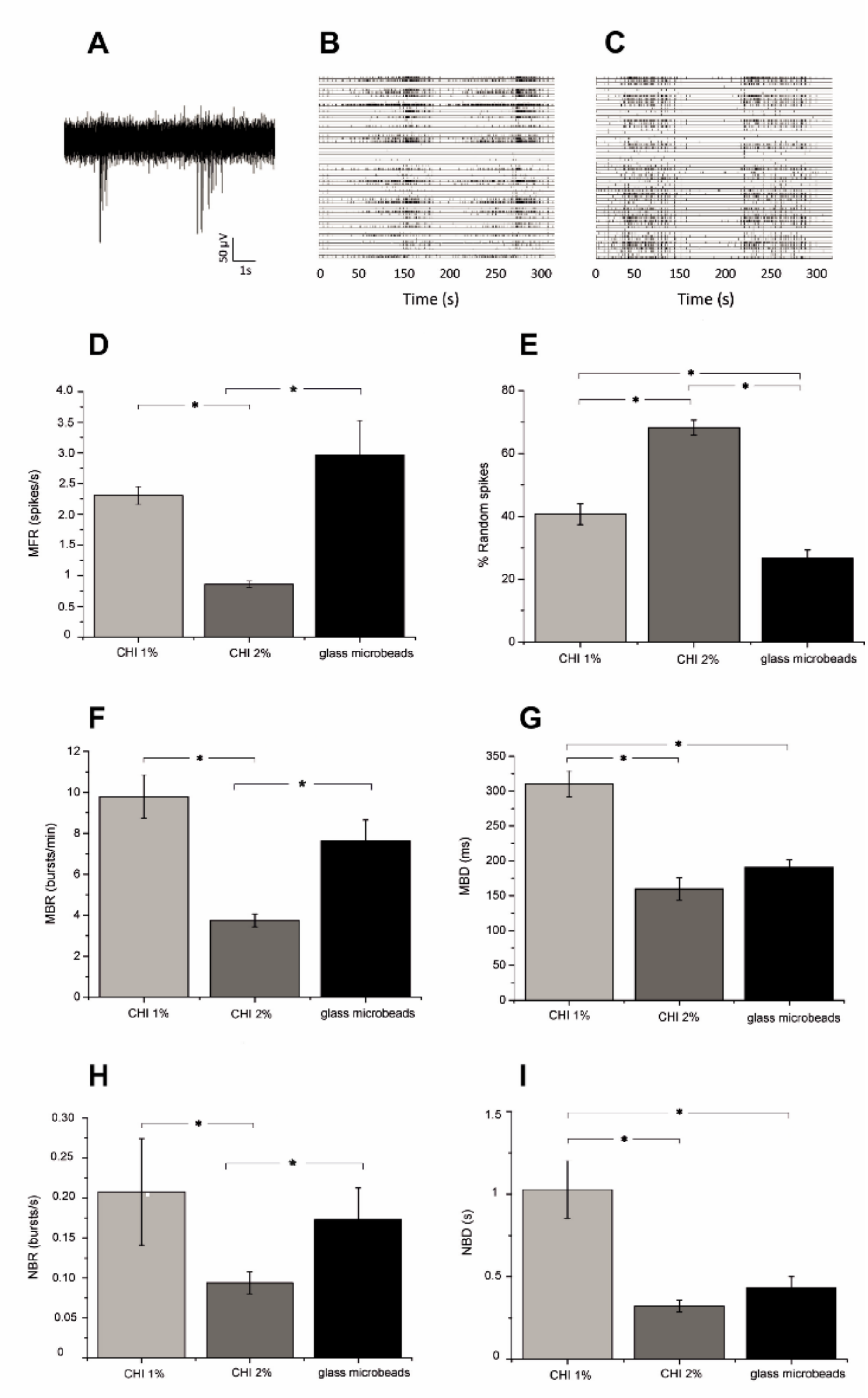

Figure 4.32 *Spontaneous activity characterization, A) 10 s of raw data recorded from a single microelectrode. Raster plot showing 300 s of spontaneous activity of 3D network on (B) 1% CHITO microbeads and(C) on glass bead; (D) mean firing rate, (E) percentage of random spiking activity, (F) mean bursting rate, (G) mean burst duration, (H) network bursting rate, (I) network bursts duration. (Kruskal-Wallis, *p < 10*$^{-3}$*).*

On the other way, round (**figure 4.32G**), 1% CHITO networks exhibited a MBD (310.5 ± 18.19). Finally, the NB activity was investigated by computing the network mean bursting rate (NBR; **figure 4.32H**) and duration (NBD; **figure 4.32I**). NBR was similar for 1% CHITO and glass microbeads networks and statistically different with respect to 2% CHITO networks. Again, for the NBD, 1% CHITO was different from 2% CHITO and glass microbeads that are in turn characterized by shorter bursts (0.32± 0.036 s and 0.43± 0.067 s, respectively).

4.5 Discussion

4.5.1 Characterization of CHITO microbeads

In this work, we explored the use of CHITO microbeads to actively support 3D functional neuronal cultures. CHITO was chosen for its biocompatibility, biodegradability, and low cost [171]. Moreover, in the literature it is reported that the positive charges of primary amines onto the polymer backbone favor the electrostatic interaction with the negatively charged cell membranes [192-195], promoting cell adhesion and growth. In general, the stiffness, porosity, and electrostatic charge of the scaffold concur in neuritic development and extension. In our case, the stiffness of 1% CHITO microbeads was found to be comparable to that of brain tissue (**figure 4.25D**). A difference in the stiffness, among 1% and 2% CHITO microbeads, was observed and could be attributed to the increase in the concentration of CHITO, corresponding to an increase in the density of the polymeric chains. Therefore, higher ionic interactions between the CHITO chains seem to be quite predictable, as the concentration of chitosan increased from 1% to 2% [196]. Besides, as shown by water content result, microbeads with lower concentration of chitosan have a higher content of water which consequently caused a decrease in stiffness [197] However, this effect is not a major factor because the difference of water content in the two samples is not remarkable and it is logic to state that the increase in the ionic interactions is the main mechanism for the stiffness growth.

Finally, AFM revealed darker areas on the surface, which might represent holes whose apparent dimensions are in agreement with data obtained by TEM (**figure 4.28C**). These characteristics combined with bioaffinity of CHITO, due to the presence of primary amines, contributed to the formation of a dense neuronal network onto CHITO microbeads.

4.5.2 Characterization of 3D neuronal networks on CHITO microbeads

The experimental design of this study was partially inspired by the results of a previous work in which a scaffold made by glass microbeads was used [187]. Indeed, to allow a direct comparison of results deriving from the use of CHITO and glass microbeads, CHITO microbeads were pre-treated with a.p. and employed as 3D support for cell attachment and growth.

The immunocytochemistry and confocal microscopy characterization allowed us to gain information on (i) the morphology of the 3D structure of mature neuronal networks after 24 days of culture and (ii) the distinct features of the two cell populations dissected from hippocampal rat brain tissues, namely neurons and glial cells.

Regarding cell morphology, the neuronal somata were found to be round, like the ones observed in the brain tissue. The ability of CHITO microbeads to maintain the in vivo cell morphology was already reported by Garcia-Giralt et al., who studied their interaction with human chondrocytes [198].

This result underlines that the combination of different factors, including substrate stiffness, 3D arrangement, and chemical cues altogether contribute to support an in vivo-like growth of the neuronal network.

The scaffold topography, characterized by confocal microscopy, showed that while the micro-scale dendritic extensions were distributed on the external surface of the CHITO microbeads, the nano-scale ones tended to penetrate the hydrogel, contributing to the formation of a compact structure.

This speculation was confirmed by TEM analysis, which allowed to understand in depth the micro- and nano- structure of the neuron-microbeads assembly. TEM micrographs (**figure 4.28**) clearly support the data obtained by confocal microscopy, putting in evidence that CHITO microbeads are enveloped in a dense network of neural dendrites and axons. At the same time, we had the evidence that smaller dendrites are allowed to enter and spread inside the CHITO microbeads, proving its porosity to neural dendrites.

The astrocyte glial fraction also proliferates on CHITO microbeads and its morphology was again similar to the one found in brain tissue (i.e., having a thin morphology and expression in GFAP). This observation was already reported by others [199-201] for 3D in vitro cultures, thus suggesting a substrate-induced morphological dependence. Interestingly, also the morphology of glial cells cultured onto CHITO film was found to be stretched (**figure 4.30**).

In the meanwhile, glial cells and the natural ECM, spontaneously produced by the neurons network in culture, were responsible for the assembly of the microbeads after four-weeks in culture. In order to verify the presence of natural ECM, we assessed the formation of perineuronal net-like structures in our culture systems using WFA.

Finally, it is worth mentioning that no evident differences between the microbeads made by CHITO at 1% compared to those at 2% were observed in terms of neuronal morphology and distribution of the biological material on the scaffold.

4.5.3 Functional characterization of 3D neuronal networks on CHITO microbeads

Regarding the electrophysiological characterization, after 21 DIVs, the 3D neuronal networks developed onto CHITO microbeads presented electrophysiological patterns similar to the ones observed for the glass microbeads in terms of the percentage of random spiking and bursting behavior. As already observed by Frega et al [187] in the case of glass microbeads, the percentage of random spiking of the 3D CHITO networks presents higher values than those observed in 2D cultures. Here we found a further increase of random spiking with respect to the 3D glass microbeads networks. Moreover, we observed that 3D CHITO 1% networks show more synchronous bursts (MBR, NBR), with respect to 3D CHITO 2% with associated longer duration for both bursts and network bursts. This activity indicates the formation of a very dense network with a high degree of connectivity as also suggested by the immunostaining for Synapsin (**figure 28C right**) and for MAP-2 (**figure 4.30**). Therefore, the 3D CHITO model presents possible advantages that would merit further investigations: (i) stiffness similar to the living brain tissue; (ii) no need for pre-treatment with a.p.; (iii) high-level of connectivity; (iv) in vivo like electrophysiological behavior.

From the other side, it should be considered that the number of active electrodes was significantly lower in the case of CHITO microbeads based 3D cultures. This was due to a lack of contacts between the substrate and the 3D assembly. Neurons were partially transferred onto the surface of the overhanging 3D assembly because of the higher bioaffinity of CHITO than the MEA surface. Moreover, it should be considered that we observed a stable assembly between CHITO microbeads and cells only after the first week in culture. Therefore, the mechanical stresses caused by replacements of the medium in the first week of culture might have contributed to the displacement of the 3D assembly.

Arrays of 3D microelectrodes ad hoc designed would provide easier physical integration with the culture and more resolved access to the electrophysiological network activity.

4.6 Conclusions

Chitosan microbeads based scaffolds were specifically optimized and adapted in order to be integrated onto planar MEAs to study and better understand the functional properties of biomimetic 3D hippocampal networks. Two types of chitosan microbeads were tested and both of them proved to be reliable supports, able to sustain the neuronal population during the growth in a 3D space. At the same time, the chitosan microbeads guaranteed both a morphological and structural development of a functional network. In conclusion, CHITO seems to be a promising scaffolding-support for developing 3D neuronal networks towards the design and implementation of brain-on-a-chip microsystems.

Chapter 5

Chitosan– based microbead scaffold enzymatic degradation

5.1 Biodegradation of chitosan

Porous scaffolds play a critical role in providing successful regeneration by acting as a three-dimensional (3D) template to carry nutrients/metabolites and promote matrix deposition along with the concomitant removal of waste and products [202]. The controlled degradation of hydrogel scaffolds is an important physical parameter in tissue engineering. Hydrogels used for implantation must degrade at a rate that is compatible with the desired function, into non-toxic products that can be easily cleared from the body, leaving healthy tissue post degradation [203]. Biodegradation of a scaffolds aimed at tissue engineering is also a complex phenomenon, the rate of which is dependent on several intrinsic and morphological factors such as pore size, pore morphology, surface area, hydrophilicity and porosity percentage and it affects cell vitality, cell growth, and even host response [205]. The rate of degradation should be ideally tailored to be inversely proportional to the rate of new regenerated tissue [204]. Once implanted in the body, a scaffold should maintain mechanical properties and structural integrity until the loaded cells adapted to the environment and excrete sufficient amount of extracellular matrix, etc.; on the other hand, after the scaffold accomplishes its mission, it could be completely degraded and absorbed by the body, leaving no trace [206]. Chitosan has been shown to be degraded *in vivo*, mainly by enzymatic hydrolysis. Lysozyme (EC 3.2.1.17) is the main enzyme responsible for the *in vivo* chitosan degradation. The enzyme exists in various forms within the fluids of the human body and in tissues, with a concentration from 4 to 13 mg / L in serum and from 450 to 1230 mg / L in tears [207]. Chitosan degradation is closely related to the degree of deacetylation (DD). When the degree of deacetylation is high (DD> 85%) degradation slows down and can last for months *in vivo*; *vice versa* if the degree of deacetylation is lower, the degradation increases [207]. Recent studies have shown that the degradation of chitosan films placed in solution with lysozyme can be controlled by N-acetylation based on measurements of weight loss [202]. Chitosan can be degraded by enzymes that hydrolyze the glucosamine-glucosamine (GlcN-GlcN), glucosamine-N-acetyl-glucosamine (GlcN-GlcNAc) and N-acetyl-glucosamine-N-acetyl glucosamine

(GlcNAc-GlcNAc) bonds [209-211]. Enzymatic degradation of chitosan scaffolds coupled with neuronal cultures (neurons and glia), by lysozyme, has led to negative outcomes inducing the lost of their functionality and the degenertion of the neuronal networks. This result suggests that other enzymatic degradation methods must be adopted, by using other types of enzymes. As it is reported n literature, chitosan can be degradate by chitinases and chitosanase. Chitosanase (EC 3.2.1.123) is the enzyme that hydrolyzes the glycosidic bonds β (1-4) of chitosan. The degradation products are called oligosaccharides which could be converted into mono-saccharides by β-Glucosidase (EC 3.2.1.21), [212,213].

5.1.1 Chitosanases

Chitosanases are specific enzymes, related to the class of hydrolases, able to hydrolyze chitosan. Chitosanases belong to the GH5, GH7, GH8, GH46, GH75 and GH80 families. In 2004 the "Enzyme Nomenclature Committee" defined the chitosanases (EC 3.2.1.132, Chitosan N-acetylglucosaminohydrolase) as the enzyme capable of carrying out endo (1 - 4) endohydrolysis between the residues GlcN (glucosamine) of chitosan partially acetylated starting from the ends [214,215]. Chitosanases are produced by plants and microbes, in which they play an important role in nutrition and defense. Chitosanases can be divided into:

- *Bacterial chitosanases*: obtained through different bacteria such as *Bacillus, Serratia, Janthinobacterium, Paenibacillus* and *Streptomyces*.
- *Fungal Chitosanase:* there is not much information about this type of chitosanase, however it has been observed that some chitosanases are produced by fungi such as *Aspergillus*, *Gorgronella*, and *Trichoderma*;
- *Cyanobacterial Chitosanase:* this is an extremely different group of photosynthetic prokaryotes that exhibit different physiological, morphological and developmental characteristics;
- *Chitosanases derived from plants.*

Chitosanases are classified into three distinct subclasses:

1. *Subclass I*: act on both the GlcN-GlcN and the GlcNAc-GlcN bonds, **figure 5.1**;
2. *Subclass II*: act only on the GlcN-GlcN bonds (most common and most constant properties), **figure 5.2**;
3. *Subclass III:* act on the GlcN-GlcN and GlcN-GlcNAc bonds;

A fourth subclass was subsequently discovered that is able to hydrolyze the GlcN-GlcN groups; GlcN-GlcNAc; GlcNAc-GlcN.

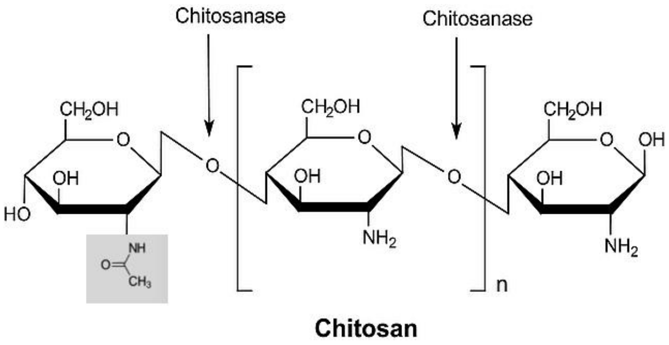
Chitosanase
Chitosanase
CH2OH
CH2OH
CH2OH
O
O
O
OH
O
O
OH
OH
OH
HO
NH
O=
CH3
NH2
NH2
n
Chitosan

Figure 5.1 *Catalytic action of the chitosanase of subclass I*

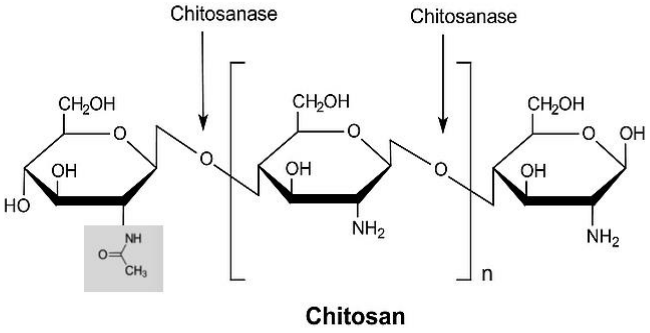
Chitosanase
Chitosanase
CH2OH
CH2OH
CH2OH
O
O
O
OH
O
O
OH
OH
OH
HO
NH
O=
CH3
NH2
NH2
n
Chitosan

Figure 5.2 *Catalytic action of the chitosanase of subclass II*

In this study, chitosanase derived from "Streptomyces coelicolor" (belonging to the GH46 family of chitosanases) has been used. Two different kinetic phases of GH46 were observed: a *first phase* of rapid degradation and a *second phase* of slower degradation [216]. In the rapid phase the GlcN-GlcN bonds are hydrolyzed; while in the slower degradation phase the bonds GlcNAc-GlcN and GlcN-GlcNAc are hydrolyzed.

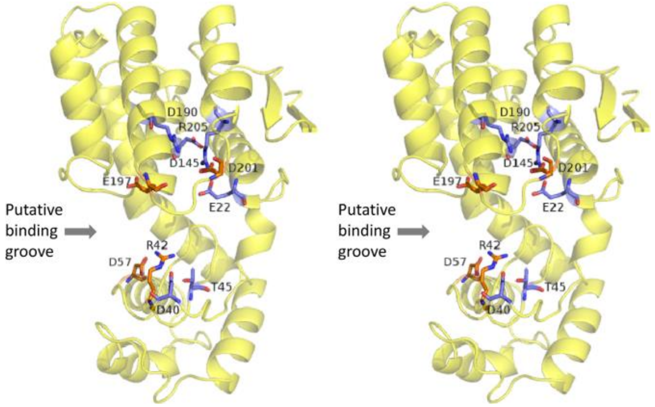
D190
R205
D145
D201
E197
E22
Putative binding groove
R42
D57
T45
D40
D190
R205
D145
D201
E197
E22
Putative binding groove
R42
D57
T45
D40

Figura 5.3 *Structure of GH46 (reprinted from Shoko Shinya et al. [215])*

The difference between chitinases (EC 3.2.1.14) and chitosanases is that chitinases are able to act on chitosan with different degrees of deacetylation (preferring the more acetylated chitosan) while chitosanases act on chitosan whit high degree of deacetylation [217-219]. The catalytic activity of chitosanases is influenced by the following factors:

- degree of deacetylation
- viscosity
- concentration of the chitosan solution
- type of acid used to dissolve chitosan
- concentration of the enzymatic solution
- pH of the buffer system
- temperature

The activity of chitosanase can be determined by measuring the viscosity reduction of the substrate, or by quantitatively estimating the reduced sugars produced by the chitosan substrates, [220]. The biochemical properties depend mainly on the source of the enzyme, [220-222]:

- *Molecular mass:* many chitosanases have an apparently low molecular mass which is in the range of 20 and 75 kDa;
- *pH and optimal temperature*: the optimal pH of chitosanases is between 4 and 8. The temperature range is from 30 ° C to 60 ° C. Many chitosanases in nature are thermolabile, however there are also those thermostables that have greater advantages in industrial applications thanks to the fact that high temperatures can accelerate reactions, decrease viscosity and increase the solubility of the raw material. The chitosanases thermostable at higher temperatures also allow to dissolve the chitosan when it is found in higher concentrations;
- *Structure of the enzyme*. The structure of the chitosanase derived from Streptomyces shows a length of about 55 Å and a secondary structure composed of 10 α-helices and 3 β-sheets. The surface of chitosanase is dominated by the appropriate electronegative slit to bind a positively charged substrate, while the analogous chitinase cleft is considerably neutral.

The degradation products of chitosanases are the COSs (**chito oligosaccharides**) which differ from the native form of chitosan due to molecular weight and solubility in water, thanks to short chains free from amino groups. In addition to having low molecular weight and being soluble in water, the COS possess bio functional properties much larger than those of chitosan, such as antimicrobials, antioxidants, lower blood cholesterol, lower blood pressure, have a protective role from infectious agents and increase the anticancer properties [212].

5.1.2 β-Glucosidase

Cellulose is one of the most important polysaccharides on earth, and is the main structural component of plants. It consists of a large number of glucose molecules (from about 300 to 3000 units) joined together by a β (1 - 4) glyosidic bond [223]. Cellulases are enzymes that belong to the family of hydrolases that catalyze the hydrolysis of the 1,4-β-D-glyosidic bonds of cellulose and cereal β-D-glucans. There are 5 classes of cellulases and the sequential action of these enzymes leads to the degradation of the polysaccharide (cellulose) in simple glucose subunits.

First, the Endocellulases break the bonds of the crystalline structure by exposing the individual chains. Then, the Esocellulases intervene which take (always through hydrolysis) from 2 to 4 units giving rise to:

- Tetrasaccharide
- Trisaccharides (Cellotriose)
- Disaccharides (Cellobiose)

Finally, Cellobiasis or β-Glucosidases, further hydrolyse the products forming single glucose monosaccharides.

β-glucosidase (β-D-glucoside glycosolase; EC 3.2.1.21) may have different origins: bacteria, animals and plants.

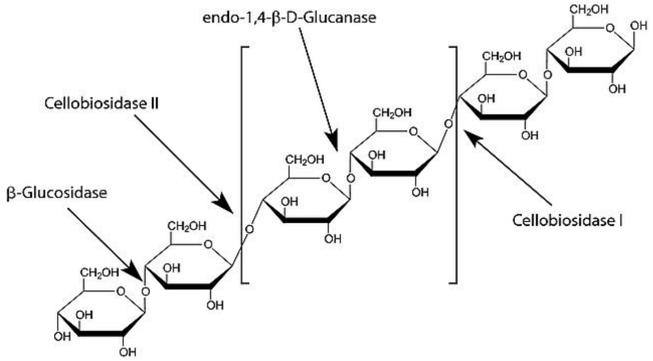

Figure 5.4 *β-Glucosidase action mechanism*

It shows high specificity to break up the β-glycosidic bonds that combine glucosides and disaccharides. Different forms of β-Glucosidase also the purification method. The most used β-Glucosidase in the degradation studies, is the one derives from the emulsin of almonds thanks to the simple extraction method. It has also been observed that the β-Glucosidase that originates from the almond emulsin has a small activity of hydrolysis on the chitin substrates, thanks to the presence of a dose of chitinase. Chitosan can be degraded by enzymes belonging to the chitinase and chitosanase families. However, chitinases and chitosanases are very expensive enzymes, and for this reason not commonly used in commercial application. So, many studies and experiments were carried out to validate the partial catalytic activity β-Glucosidase in the degradation of chitosan with different molecular weights and different degrees of deacetylation [210]. Almost all β-Glucosidases have more or less the molecular weight in a range from 55 to65 kDa and the pH optimum is between 5-6.

β-Glucosidase is also used in the synthesis of glucosides, shows potential applications in the pharmaceutical, cosmetic and detergent industries, it is also used as an aromatization of fruit and wine juices and intervenes in the biosynthesis of oligosaccharides.

5.2 Aims

The aim of this study was to define a protocol for the enzymatic degradation of chitosan –based microbeads scaffold for 3D hippocampal cultures. The degradation protocol was defined starting from studies reported in the literature: Chitosanase is the enzyme with the greatest catalytic activity on chitosan, while β-Glucosidase is an enzyme able to hydrolyzing only the disaccharides. For this reason, firstly, the chains of chitosan should be partially degraded by chitosanase, secondly they can be recognized and degraded by β-Glucosidase. Two enzymatic degradation protocols were developd and characterized.

5.3 Materials and methods

The protocol for the production of 2% CHITO microbeads and the preparation of a 3D neuronal cultures is reported in Chapter 4.

5.3.1 Optical microscopy

An inverted IX-51 Olympus microscope equipped with a DP70 digital camera coupled with CPlan 10X N.A. 0.25 PhC objective was used to acquire contrast phase images of CHI microbeads coupled with neurons. An Olympus BX-51 upright microscope was used for immunofluorescence evaluation of the biological samples and the image acquisition was done with a Hamamatsu Orca ER II digital cooled CCD camera driven by Image ProPlus software (Media Cybernetic).

5.3.2 Degradation protocols

The *first protocol* involved the application of two enzymes to 25 µl of 2% CHITO microbeads suspended in 250 µl of culture medium. The degradation test involves three phases:

- **Phase 1** (day 1): addition of the first dose of Chitosanase enzymatic solution (50 µl, 1 U / ml) to the microbeads suspension.
- **Phase 2** (day 2): change of culture medium and addition of the second dose of Chitosanase (50 µl, 1 U / ml) to the microbeads suspension.
- **Phase 3 (**day 3): change of culture medium and addition of β-Glucosidase dose (50 µl, 1 U / ml) to the microbeads suspension.

This protocol was applied also to neuronal cells cultured for 5 days to check if the enzymes trigger cell toxicity.

The *second protocol* foreseesed to put for 19 days CHITO micorbeads in incubator at 37 ° C and then exposed them to the ap two enzymes solutions. The addition of the enzymes at DIV 19 is dictated by the fact that the formation of the neuronal network occurs over a period of 19 - 21 days, only after that the degradation of the scaffold could start. The degradation test involves three phases:

- **Phase 1** (day 1): 25 µl of microbeads suspended in 250 of culture medium and placed in an incubator at 37 ° C for 19 days
- **Phase 2** (day 19): addition of the dose of enzymatic solution of Chitosanase (50 µl, 1 U / ml) to the microbeads suspension.
- **Phase 3** (day 20): addition of the 50 µl of β-Glucosidase enzyme solution (1 U / ml) to the microbeads suspension.

Finally, in order to evaluate scaffold degradation in cell culture, a preliminary study was conducted to verify the toxicity of the two enzymes for neuronal cells. The first protocol defined in the previous paragraph was applied directly onto a 2D neuronal culture and onto a 3D neuronal culture on chitosan microbeads scaffold. To demonstrate if the exposure to the enzyme triggers has a toxic effect on the neuronal cells, the first dose of Chitosanase was added at DIV 5 and maintained in culture for 24 days.

5.4 Results

Two different concentrations of chitosanase enzymatic solutions (0.5 U/ml and 1 U/ml) were evaluated to define the best concentration for the degradation of CHITO microbeads. In the first case, 25 µl of CHITO microbeads were suspended in 31 µl of enzymatic solution at 0.5 U/ml, **figure 5.5**.

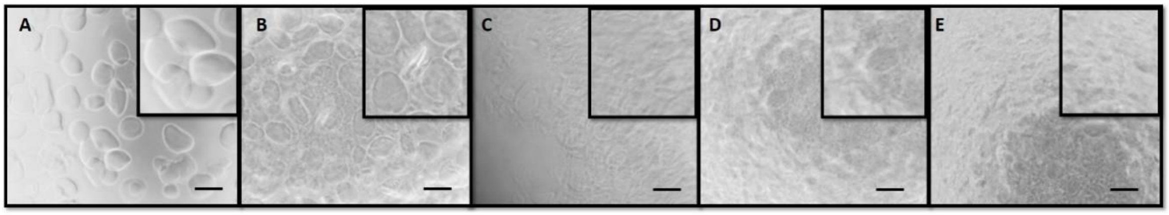

Figure 5.5 *Optical images of 2% CHITO microbeads exposed to 25 µl of Chitosanase solution at (0.5 U/ml). A) 0h, B) 6h, C) 24h, D) 48h, E) 6 days. Scale bar: 100 µm.*

Then, 25 µl of CHITO microbeads were suspended in 31 µl of enzymatic solution at 1 U/ml, **figure 5.6**. As can be seen in the **figures 5.5** and **5.6**, both concentrations of chitosanases determined the degradation of CHITO micorbeads. In particular, a completly degradation was observed after 24h h by the activity of chitosanase at 1 u/ml, **figures 5.6A-E**. From this results, all the experiments were carried out by using chitosanase solution at1 u/ml.

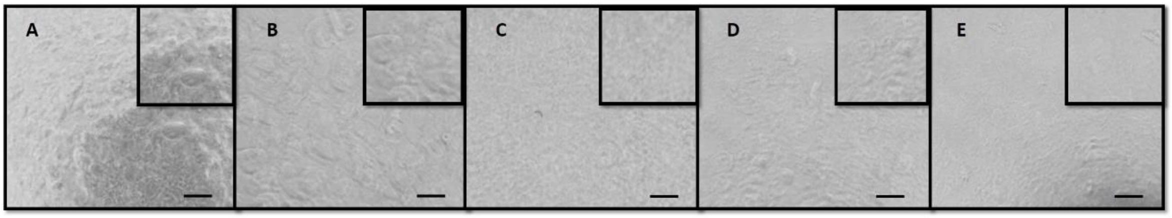

Figure 5.6 *Optical images of 2% CHITO microbeads exposed to 25 µl of Chitosanase solution at (1 U/ml). A) 0h, B) 6h, C) 24h, D) 48h, E) 6 days. Scale bar: 100 µm.*

25 µl of CHITO microbeads were suspended in 300 µl of culture medium were exposed at three different combinations of Chitosanase and β-Glucosidase solutions. The first experiment involved the addition of 50 µl of Chitosanase enzymatic solution. After 24 h, a second dose of 50 µl of Chitosanase solution was

added. After 48 h, 50 µl of β-glucosidase were added to the microbeads suspension, **figure 5.7A (1-5)**. In the second experiment, the first steps are the same of the first experiment but after 48h, the microbeads suspension were exposed at 50 µl of β-glucosidase are added + 25 µl of Chitosanase solution., **figure 5.7B (1-5)**. Finally, the third experiment involves the addition of 25 µl of Chitosanase + 25 µl of β-Glucosidase at 1 U / ml. As in experiment 1, the culture medium is changed every 24 h and degradation is monitored up to 72 h, **figure 5.7C (1-5).**

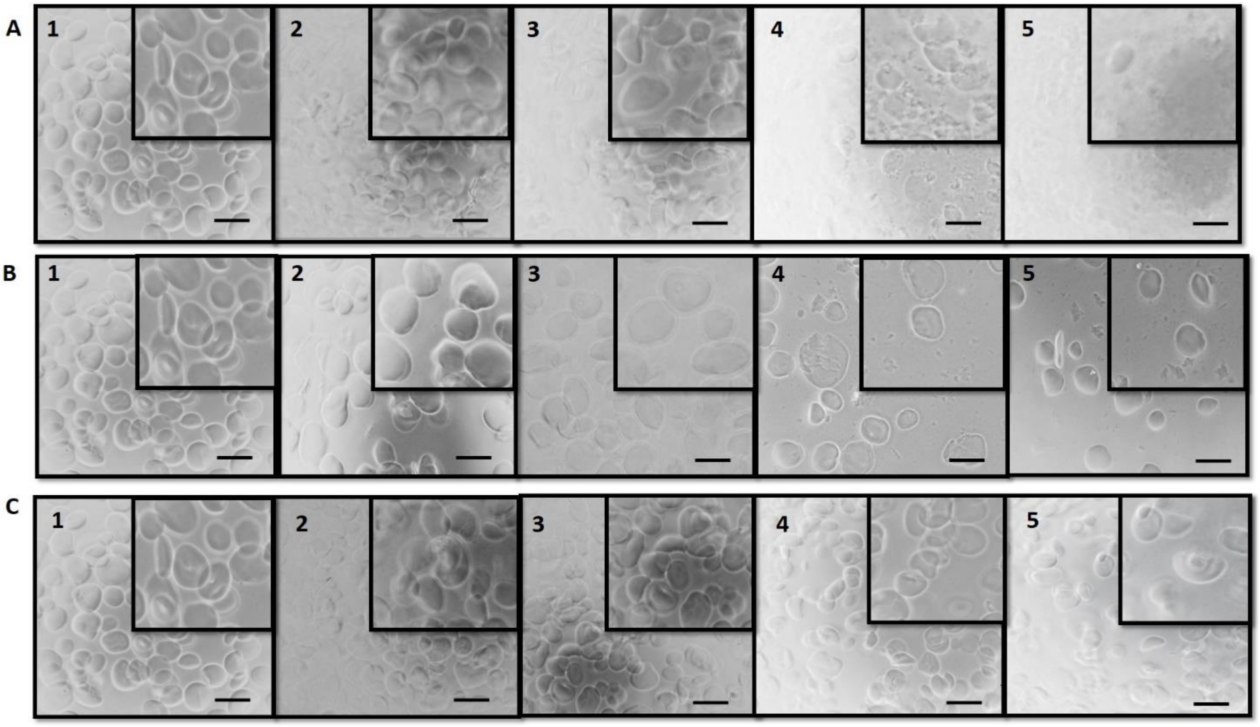

Figure 5.7 *Optical images of 2% CHITO microbeads treated following the first protocol in three different conditions at the last step of the protocol (A) β-glucosidase (50 µl), (B) β-glucosidase (50 µl) + Chitosanases (25 µl), (C) β-glucosidase (25 µl) + Chitosanases (25 µl), at different time points 1) 0h, 2) 6h, 3) 12 h, 4)24 h and 5) 48h h. Scale bar: 100 µm*

Images of CHITO microbeads trated following the first protocol, are showed in figure 5.7 It is possible to observe a degradation of micorbeads at different time points for all three experiments. The best result is observed whit the combination of 50 µl β-Glucosidase and 25 µl of Chitosanase as the last step.

The first experiment of the second protocol involved the addition of 50 µl of β-Glucosidase enzyme solution at 1 U/ml to the microbeads in the medium, **figure 5.8A (1-5**). For the second experiment, 50 µl of Chitosanase enzymatic solution was added immediately to the microbeads suspension. After 24h in incubator, 50 µl of β-glucosidase solution was added, **figure 5.8B (1-5)**. Instead, the third experiment involved the combination of both enzymes, 25 µl of β-glucosidase + 25 µl of Chitosanase added to the microbeads suspension, **figure 5.8C (1-5).**

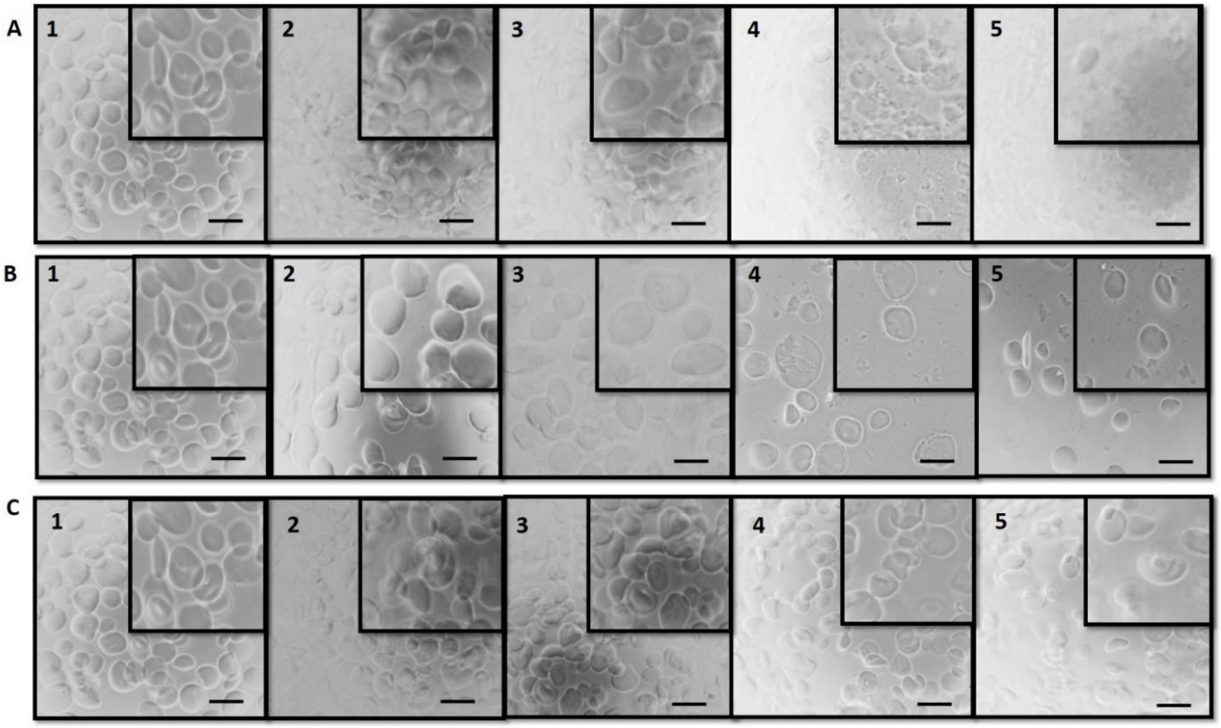

Figure 5.8 *Optical images of 2% CHITO microbeads treated following the first protocol in three different conditions*

(A) only β-glucosidase (50 µl), (B) Chitosanases (50 µl) and then β-glucosidase (50 µl), (C) β-glucosidase (25 µl) + Chitosanases (25 µl), at different time points 1) 0h, 2) 6h, 3) 12 h, 4)24 h an 5) 48h. Scale bar: 100 µm.

In order to evaluate the cytotoxicity of the Chitosanase solution on primary neuronal culture, 50 µl of Chitosanase solution (1 U/ml) was added directly onto 2D culture. The addition of Chitosanase's enzyme solution to 1 U/ml did not trigger a toxic effect on neurons and onto the neuronal network, **figure 5.9**.

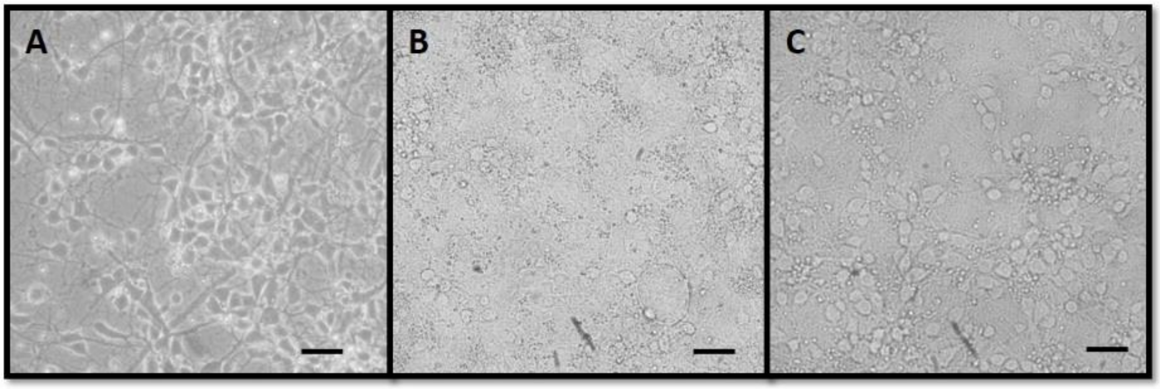

Figure 5.9 *Optical images of 2D neuronal network. A) 2D neuronal culture not exposed to enzymicatic solution; B) 2D neuronal culture immediately after the exposition to the enzymicatic solution; C) 2D neuronal culture exposed to enzymicatic solution after 20 DIV. Scale bar: 50 µm.*

The last experiment involved the addition of 50 µl of Chitosanase (1 U/ml) to 3D neuronal network developed on CHITO microbeads scaffold after DIV 19, **figure 5.10**. The enzymatic solution was added every time that the culture medium was changed. Only after the third change of medium, it was possible to observe a partially degradation of the microbeads on the edges of the scaffold, **figure 5.10D**.

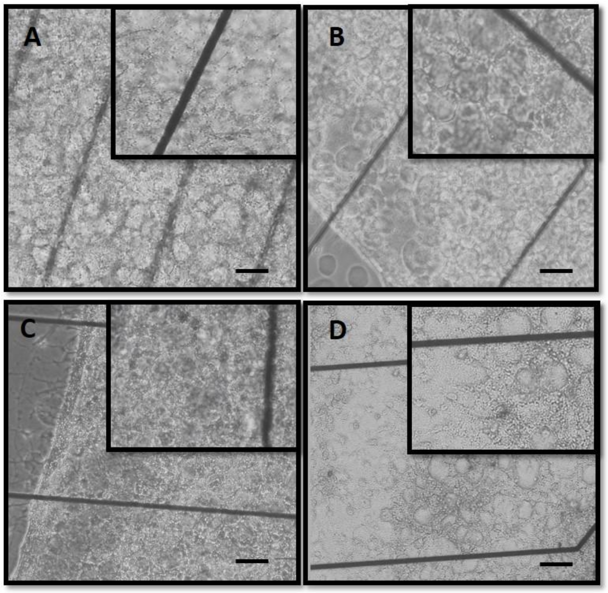

Figure 5.10 *Optical images of 3D neuronal networks on CHITO microbeads based-scaffold exposed to enzymes solutions: A) not exposed to enzymicatic solution, B) 24h after the exposition to the enzymicatic solution, C) 48h the exposition to the enzymicatic solution and D) 72 h the exposition to the enzymicatic solution. Scale bar: 100 µm.*

5.5 Discussion

For the first protocol, the percentage of not degraded microbeads was decreased very rapidly in the first 12 hours, with a further decrease from 57% of intact microbeads to 23%, especially after the addition of the second dose of Chitosanase, **figure 5.11, red line**. Adding the β-Glucosidase after 48 h, a further 17% decrease is observed. The addition of only 25 µl of Chitosanase determined a slow degradation. The addition of only the mix solution didn't show any improvements in the degradation. Observig the black line, it can be deduced that the addition of a mix of β-Glucosidase and Chitosanase had an inhibitory effect on degradation. This effect is probably due to insufficient activity of β-Glucosidase. As described in the section on β-Glucosidase, it is an enzyme that intervenes in the hydrolysis of cellulose, which differs from chitosan for the -OH groups.

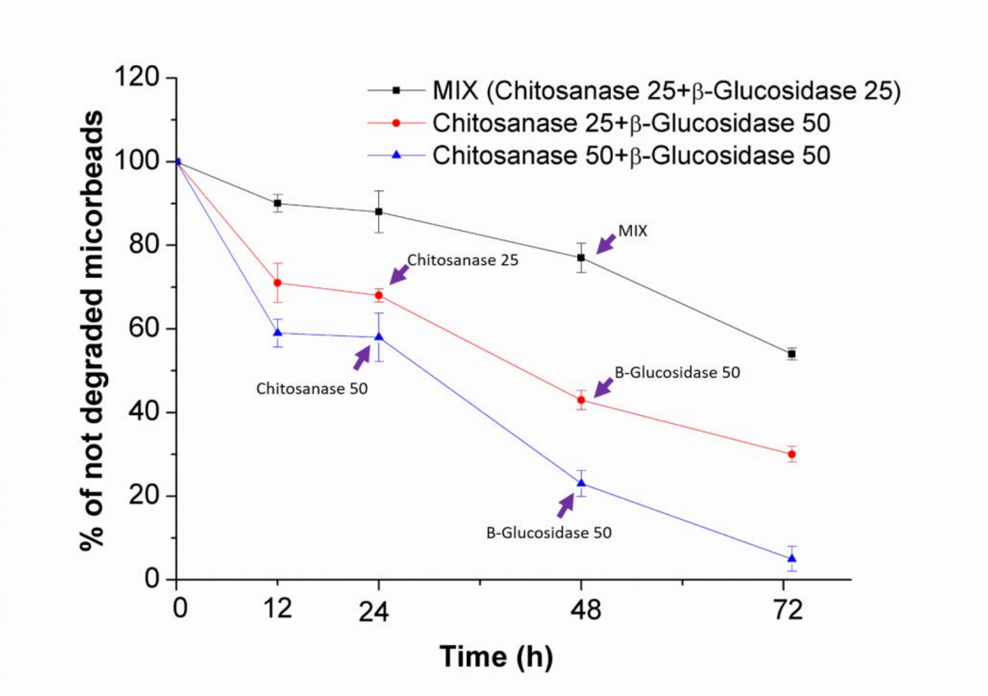

Figure 5.11 *Time dependence of the effects of Chitosanase and β-Glucosidase solutions on CHITO microbeads. Microbeads were exposed for 12, 24, 48, 72hr and the number of the microbeads not degraded was measured. Results show the effect of 50 µl of chitosanase solution after 24h and 50 µl of β-Glucosidase solution after 48h (blue line), 25 µl of chitosanase solutions after 24h and 50 µl of β-Glucosidase solution after 48h (red line), and chitosanase + β-Glucosidase solution after 48h (black line).*

As it is reported in literature, in general cellulose is degraded by the hydrolysis of cellulase, an enzyme composed of three sub-enzymes:

- *Exo glucanase or cellobiohydrolase (CBH I - CBH II)*
- *Endo glucanase*
- *β-Glucosidase*

The exo glucanases produce the cellobiose, which is the same inhibitor of CBH I and II, when it is accumulated in large quantities, the catalytic action of β-Glucosidase is not sufficient to convert dimers into monosaccharides, [225]. It is therefore assumed that β-Glucosidase added to Chitosanase inhibits the degradation of microbeads by Chitosanase. Therefore, to have an almost total degradation, it is necessary to add the Chitosanase first, which has a greater catalytic effect on the chitosan and only after 48 h, add the β-Glucosidase, which, as known from the literature, hydrolyses only the beta glycosidic bonds in disaccharides.

The second protocol, firstly, foreseesed to put in incubator CHITO micorbeads suspended in medium culture for 19 days. After that, CHITO microbeads were exposed to different enzymatic solution: forthe first experiment the starting solution was β-Glucosidase solution, for the second and the third experiment 50 μl Chitosanase solution. With the second protocol only β-Glucosidase solution (pink line) had not catalytic effect on the CHITO microbeads, due to its inabilityto hydrolyse the (1-4) glycoside bonds in the disaccharides.

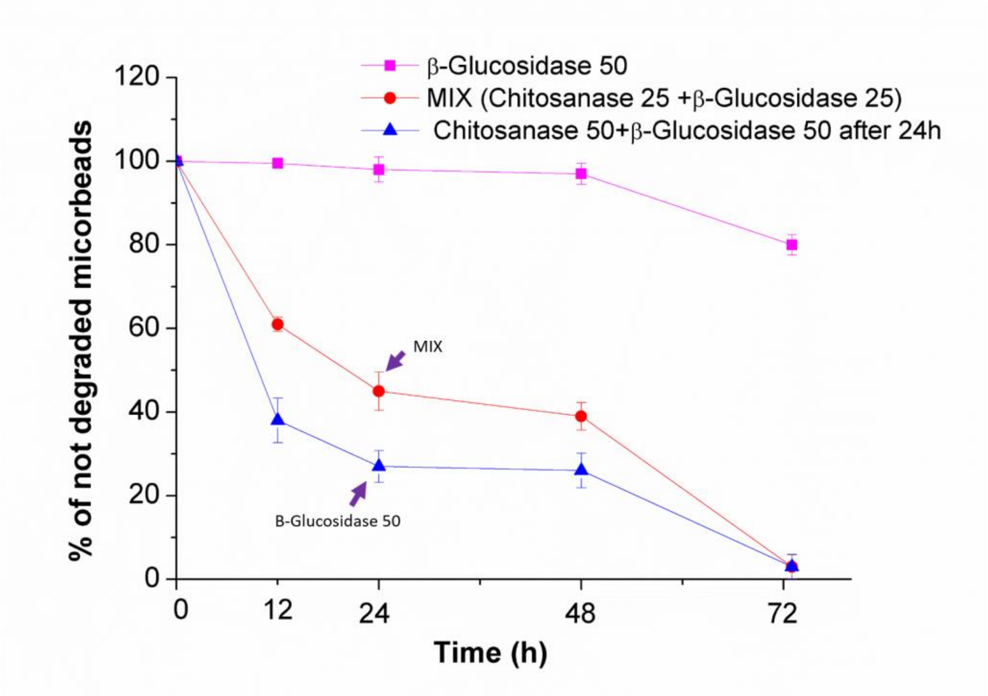

Figure 5.12 *Time dependence of the effects of Chitosanase and β-Glucosidase solutions on CHITO microbeads after 19 in incubator at 37°C. Microbeads were exposed for 12,24, 72hr and the number of the microbeads not degraded was*

measured. Results show the effect of the only 50 µl of β-Glucosidase solution (pink line), 25 µl of chitosanase + 25 µl of β-Glucosidase solutions after 24h (red line), and 50 µl of β-Glucosidase solution after 24h (blue line).

The degradation of chitosan with the addition of only β-Glucosidase could occur in the case of a very high concentrations of enzymatic solution. In accord of the results obtained, the microbeads suspension was fisrtly exposed to chitosanase and then to the chitosanase- β-Glucosidase mixed solution after 24 h for the first enimatic exposure. In the first 12 hours there was a greater catalytic effect due to the chitosanase activity, and a further degradation due to the activity of the mix of the two enzymes, **figure 5.12, red line.** The best degradation was observed with the protocol which provided the addition of only β-Glucosidase solution after 24h, **figure 5.12**, **blue line**. For both these two protocols the completely degradation was observed afetr 72h.

5.6 Conclusion

A new protocol for the degradation of 2% CHITO microbeads was developed and characterized. Chitosanase and β-Glucosidase solutions were able to degrade CHITO microbeads in 72 h a 37 ° C in incubator. The best degradtation was observed exposing firstly, the CHITO microbeads at 1 U/ml nd then to β-Glucosidase solution. However, only a partial degradation was observed onto the 3D microbeads scaffold seeded with cells, due to the fact that neuronal cells developped a dense network around the hydrogel which created obstacle shield for the homogenous diffusion of the enzyme molecules inside the scaffold. Interestingly, the two enzymes didn’t induce any toxic response onto neuronal networks.

Chapter 6

GelMA-based microbead scaffolds with tunable mechanical characteristics for different soft tissue models

This chapter was adapted from the following publication:

Sheiki A.et al., *“Microengineered Emulsion-to-Powder Technology for the High-Fidelity Preservation of Molecular, Colloidal, and Bulk Properties of Hydrogel Suspensions*.” ACS Applied Polymer Materials. 2019.

6.1 Granular hydrogel scaffold

Granular hydrogel scaffolds has opened new opportunities for overcoming some of the shortcomings of bulk hydrogels biomedical applications. These hydrogels, when decorated with physically/chemically cross-linkable moieties, provide injectable, soft platforms [225-228] that may mimic the extracellular matrix (ECM) while maintaining interconnected micrometersized pores. The injectable microporous scaffolds facilitate cell infiltration in vivo without requiring degradation, which significantly reduces inflammation and healing time. Accordingly, injectable granular hydrogels have secured an important role in accelerated wound healing and tissue regeneration. [227,229,231]. The building blocks of granular hydrogels are typically tens of micrometer-sized hydrogel particles physically and/or chemically cross-linked and suspended in an aqueous phase, such as phosphate-buffered saline (PBS) or cell culture media. Challenges associated with the sterilization of aqueous suspensions, the short lifetime of active substances in aqueous media, bacterial and viral contamination, reduced long-term stability, and the need for having an in-house microfluidic facility to produce fresh beads have limited the broad reach of such microfluidic-enabled biomaterials [231,231]. Converting a stabilized hydrogel suspension to a dried solid phase may overcome these challenges; however, current efforts for drying colloidal dispersions and suspensions mainly rely on solvent evaporation and spray-drying [233], freeze-drying [234,235], electrospinning [236], and electrospraying [237], none of which have been able to decently preserve the physical and/or chemical properties of the fragile dispersed phase upon rehydration. Importantly, cryoprotectants, e.g., polyethylene glycol (PEG), are highly prone to vitrification and have only been able to partially protect dispersed phases in a colloidal system during freeze-drying when the freezing rate is low and/or the concentration of the additive is very high, e.g., 40 wt % (14). Accordingly, fragile hydrogel particles are among the most challenging classes of materials to be converted to a dry state that can recover all physicochemical properties when rehydrated. Furthermore, separating the dispersed phase of emulsions, particularly when the particle size is small, has been extremely cumbersome [1238,239].

6.2 Aims

We introduce a novel, facile technology for the ondemand conversion of water-in-oil emulsions to fine powders with completely preserved molecular, colloidal, and bulk properties. We introduce the microengineered emulsion-topowder (MEtoP) technology to inhibit the aggregation and permanent deformation of dispersed phase drops or hydrogel particles undergoing harsh deep-freezing and low-pressure lyophilization via use of a heat-conductive, volatile oil as a continuous phase. We first convert two model microgel particle systems, gelatin methacryloyl (GelMA), to uniformly sized droplets-in-oil emulsions, followed by physical/chemical cross-linking to form hydrogel microbeads. Subsequently, we show that in contrast to the conventional lyophilization of hydrogel microbeads once phase transferred to an aqueous continuous phase, which produced permanently clumped polymer aggregates with lost functionality, the MEtoP technology is able to convert the microgels into dried and disaggregated fine particles that can be successfully resuspended in an aqueous medium. Once resuspended, the particles can regenerate their shape, size, and chemical functionality with no difference from freshly manufactured particles.

6.3 Materials and methods

Materials

Silicon wafers were purchased from University Wafer (MA, USA), negative photoresist was from KMPR 1050, MicroChem Corp. (MA, USA), and the microfluidic chips were fabricated using polydimethylsiloxane (PDMS) base/the curing agent (SYLGARD™ 184 Elastomer Kit, Dow Corning, MI, USA). The microfluidic tubing was 1569-PEEK Tubing Orange 1/32" OD x .020" ID (IDEX Corp., IL, USA) and Tygon Flexible Plastic Tubing 0.02" ID x 0.06" OD (Saint-Gobain PPL Corp., CA, USA). The microfluidic device was treated with Aquapel® Glass Treatment (Pittsburgh Glass Works LLC, PA, USA). 3M™ Novec™ 7500 Engineered Fluid (Novec 7500 oil) was purchased from 3M (MN, USA). Photoinitiator 2-hydroxy-1-(4-(hydroxyethoxy)phenyl)-2-methyl-1-propanone (Irgacure 2959), gelatin from porcine skin (type A, 300 bloom), methacrylic anhydride (MA, 94%), 1H,1H,2H,2H-perfluoro-1-octanol (97%), and fluorescein isothiocyanate (FITC)-dextran (500 kDa) were provided by Sigma-Aldrich (MO, USA). Milli-Q water (electrical resistivity ~ 18.2 MΩ cm at 25 °C) was from Millipore Corporation. Dialysis membranes (molecular weight cutoff ~ 12-14 kDa) were purchased from Spectrum Lab Inc (CA, USA). Cover slips (No. 1) and VistaVision™ Microscope Slides (Plain 3” x 1”) were provide by VWR (PA, USA), and microscope glass slides (18 mm x 18 mm x 300 µm) were purchased from Fisher Scientific (PA, USA). Pico-Surf™ 1 (5% (w/w) in Novec™ 7500) was provided by Sphere Fluidics Inc (Cambridge, UK). Dulbecco's phosphate-buffered saline (DPBS) solution (1X) was from Gibco (NY, USA).

Methods

6.3.1 Microfluidic device fabrication

To generate uniform-sized spherical microbeads, a high-throughput microfluidic water-in-oil emulsion method [240-242] was modified and used. Highly parallelized step emulsification devices were fabricated as previously reported [1243] using standard soft lithography techniques. Master molds were fabricated using a two-layer photolithography process. Mechanical grade silicon wafers (4 in) were sequentially layered with photoresist (32 um KMPR 1025, 160 um KMPR 1050) and patterned using standard photolithography techniques. At a ratio of 10 to 1, the PDMS base and the curing agent were mixed and poured onto the molds affixed to petri dishes, followed by degassing and curing in an oven

(65 °C for >4 h). The PDMS device was detached from the mold and perforated (0.8 mm holes) at the inlets and outlets. To seal the microchannels, both the device and a glass slide were activated via air plasma for 40 s (PLasma Cleaner, Harrick Plasma, NY, USA) and bonded together. To render the channel surfaces fluorophilic, the device was treated with Aquapel, followed by washing with the Novec 7500™ oil.

6.3.2 GelMA synthesis

Gelatin type A was modified with a high degree of methacryloyl substitution to synthesize GelMA following our previous protocols [244,245]. Briefly, 10 g of gelatin was dissolved in 100 mL of warm DPBS (50 °C), followed by the dropwise addition of 8 mL of MA while stirring the solution at 240 rpm. This resulted in a turbid biphasic mixture, which was allowed to react by stirring for 2 h at 50 °C. This condition prevents protein hydrolysis [246]. Upon completion of reaction duration, excessive DPBS was added to the mixture to stop the reaction. The mixture was then loaded in the dialysis membranes and stirred in DI water (40 °C) for at least seven days to remove methacrylic acid and other impurities. The result of dialysis was a clear GelMA solution, which was lyophilized and stored in room temperature before using for microgel fabrication.

6.3.3 GelMA bead fabrication

Freeze-dried GelMA was dissolved in a mixture of DPBS and the photoinitiator (0.5% w/v, Irgacure 2959) at 80 °C for ~20 min to yield GelMA solutions (7-20 % w/v). These solutions provided the dispersed (aqueous) phase in the high-throughput microfluidic device, which were injected in the pinching flow of Novec 7500 oil-surfactant (0.5 wt% PicoSurf) mixture, simultaneously introduced into the microfluidic device using syringe pumps (Harvard Apparatus PHD 2000, MA, USA) to form surfactant-stabilized 100 µm beads of GelMA in the engineered oil (continuous) phase. The microfluidic setup including the syringes and tubing were maintained at 37-40 °C to avoid GelMA sol-gel transition and device blockage. A microcentrifuge tube was used to collect the bead suspension in oil and store at 4 °C.

6.3.4 Microengineered emulsion-to-powder (MEtoP) technology

MEtoP technology is based on protecting the dispersed phase of an emulsion to preserve its physical and chemical cues during harsh freezing and lyophilization procedures. In our experiments the interface of dispersed (aqueous) phase is stabilized using an engineered oil (Novec™ 7500) including a surfactant (Pico-Surf™). The oil is highly heat conductive, volatile, and has a low freezing point. The oil/surfactant-stabilized aqueous phase is deep frozen (e.g., at -80 °C and/or -196 °C) and transferred to a lyophilizer (Labconco FreeZone Benchtop Freeze Dry System) to sublimate the ice and remove the volatile oil under vacuum (e.g., 0.06 mbar) for at least 6 h. This process results in a one-step conversation of emulsions to powders made up of microengineered particles with preserved properties

.

6.3.5 Conventional lyophilization of hydrogel microbeads

The hydrogel microbead-in-oil emulsions were pulse centrifuged (6300 rpm, 10 s, GmCLab mini centrifuge, Gilson, France), and the excess oil was removed using a pipette. To break the emulsion, a perfluorooctanol solution (20%) in Novec™ 7500 oil was added to the bead suspension (1:1 volume ratio), which removed the surfactant. The GelMA beads were always maintained at 4 °C and the PEG-VS beads were at 25 °C. The suspension was diluted in a DPBS solution, and the physically-crosslinked

(GelMA) or chemically-crosslinked (PEG-VS) microbeads were pulse centrifuged and the supernatant was removed. The beads were transferred to another microcentrifuge tube using a positive-displacement pipette (MICROMAN® E, Gilson, WI, USA) and always maintained in DPBS. The tubes were frozen at -80 °C overnight, followed by lyophilization at ~0.06 mbar bar for at least 24 h. The process was conducted in a way that the frozen samples never melted and always remained frozen until competing the ice sublimation process.

6.3.6 Beaded hydrogel powder imaging and rehydration

Powders were transferred onto a cover gas and imaged using a camera (Axio cam 503 mono, 60N-C 1” 1,0X). The microstructures of powders were visualized using dark or bright filed microscopy (Axio Observer 5, Zeiss, Germany). The rehydration (swelling) of powder GelMA beads was investigated by suspending them in cold DPBS (1X, 4°C). Similar experiment was conducted with PEG-VS at room temperature. Brightfield microscopy at predefined time intervals was conducted to image the beads and measure their size via image analysis using ImageJ (Version 1.52e, National Institute of Health, USA).

6.3.7 Fabrication of beaded GelMA (B-GelMA) scaffolds

To evaluate the properties of beads produced using the MEtoP technology and compare them with the freshly-prepared beads as well as the conventionally-lyophilized ones, the oil-free microbeads were suspended in DPBS (4 °C) containing the photoinitiator (0.5% w/v, Irgacure 2959), followed by pulse centrifugation for 10 s to pack the bead at the bottom of container. Using a positive displacement pipette, the concentrated microbeads suspension was transferred into a PDMS mold (diameter ~ 8 mm, height ~ 1 mm) and incubated for a desired period (to investigate the effect of packing), followed by UV light

(360-480 nm, Omnicure, Excelitas, CA, USA) exposure (intensity ~ 10 mW cm^{-2}) for 2 min, yielding chemically-crosslinked and possibly annealed microbeads.

6.3.8 Characterization of GelMA microbeads

6.3.8.1 Pore size analysis

Chemically-crosslinked hydrogel scaffolds were incubated in a FITC-dextran solution (15 mM) to fill the void space in the scaffolds with the dye. The large molecular size of dextran prevents its diffusion into the beads, enabling us to visualize the void spaces. The dye-infused scaffolds were imaged using a Leica inverted SP5 confocal microscope (Germany) at the California NanoSystems Institute (CNSI). For each sample, 77 *z*-slices were captured to cover total height of ~150 µm, and at least 3 samples per condition were analyzed. Median pore diameter and void space fraction were measured using a custom-developed Matlab code (Matlab, version 2017b). The stacked images were converted into discrete regions using an Reprintedive thresholding, and the void space fraction was calculated based on the voxel volume of void space regions. Average pore diameter was calculated based on a previously-published method [8].

6.3.8.2 Mechanical analyses (compression tests)

Crosslinked beaded GelMA samples (UV intensity ~ 10 mW cm^{-2}, exposure time ~ 2 min) in PDMS molds (diameter ~ 8 mm and height ~ 1 mm) were transferred to the Instron mechanical tester (Instron 5542, Norwood, MA, USA) and compressed at a rate ~ 1 mm min^{-1}. The linear stress-strain region was fitted with the best line (0-10% strain) and the slope was registered as the compression modulus (= stress/strain).

6.3.8.3 Statistical analysis

Measurements were performed at least in triplicate. The data were reported as mean values ± standard deviation. The one-way analysis of variance (ANOVA) was carried out followed by Tukey's multiple comparisons. Statistically significant differences were identified when p-values were lower than 0.05 (*$p<0.05$), 0.01 (**$p<0.01$), 0.001 (***$p<0.001$), and 0.0001 (****$p<0.0001$).

6.4 Results

The principles of MEtoP technology is based on protecting the dispersed phase of an emulsion during harsh freezing and lyophilization steps using an engineered oil that (i) has a decent heat conductivity, (ii) is easily removed under vacuum during lyophilization, (iii) preferably has a very low freezing point, and (iv) is well mixed with a surfactant to stabilize the oil-water interfaces. The heat conductivity of the oil (continuous phase) facilitates the deep freezing of the dispersed phase, while the oil remains unfrozen, followed by the vacuum-mediated removal during lyophilization. We selected the mixture of Novec™ 7500 oil with a surfactant (PicoSurf, 0.5 wt%), which satisfies all of our design criteria. Many other oils can potentially be used for this purpose. To evaluate the capability of MEtoP technology in converting an aqueous dispersed phase to a powder with preserved molecular, colloidal, and bulk properties, the uniformly-sized microspheres of hydrogels (e.g., GelMA) were produced using a high-throughput step emulsification microfluidic device, shown in Figure 1a, in which varying concentrations of GelMA dissolved in an aqueous solution were injected along with the engineered oil mixture (continuous phase) to generate hydrogel microbeads with a diameter of ~100 µm.

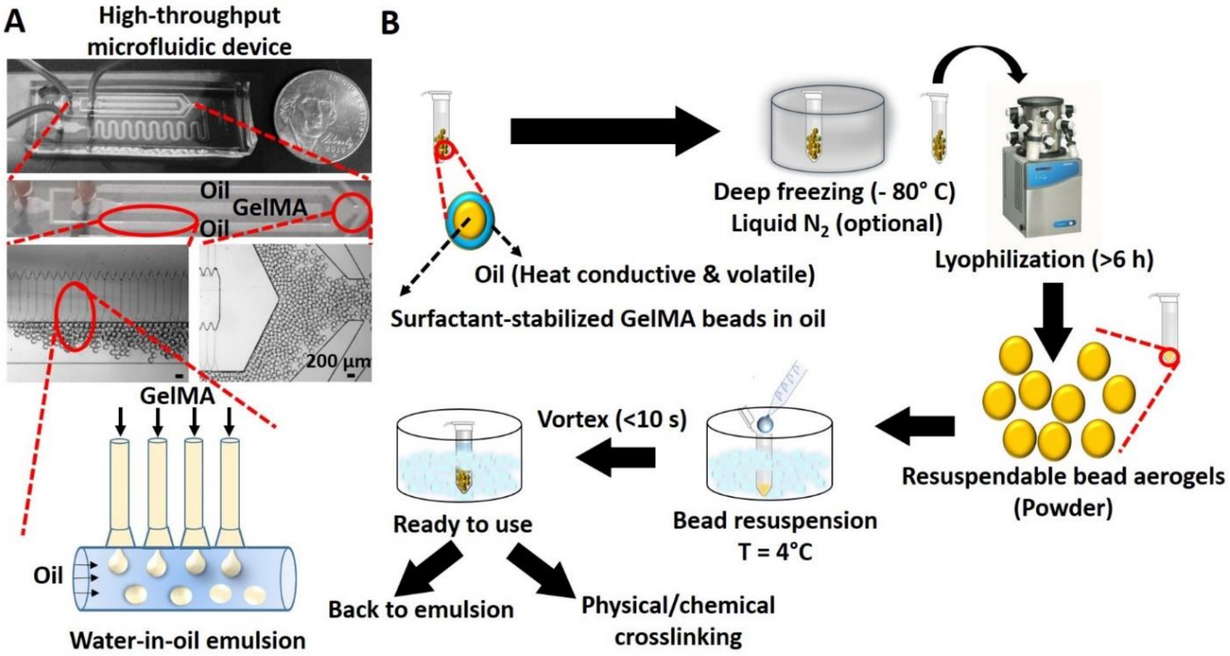
A
High-throughput microfluidic device
Oil
GelMA
Oil
200 µm
GelMA
Oil
Water-in-oil emulsion
B
Oil (Heat conductive & volatile)
Surfactant-stabilized GelMA beads in oil
Deep freezing (- 80° C)
Liquid N₂ (optional)
Lyophilization (>6 h)
Resuspendable bead aerogels
(Powder)
Bead resuspension
T = 4°C
Vortex (<10 s)
Ready to use
Back to emulsion
Physical/chemical crosslinking

Figure 6.1 *MEtoP technology to convert microfluidic-enabled hydrogel particle emulsions to powders. A) parallelized step emulsification device was used for the high-throughput fabrication of GelMA polymer microbeads. B) Procedure to convert emulsion microbeads in powder.*

Droplet generation is driven by a sudden expansion at the end of each of the droplet generation channels. As the dispersed phase reaches the end of the channel, the expansion induces an instability that drives uniform drop formation [44]. The surfactant-stabilized hydrogel beads were deep-frozen at -80 °C as presented in **Figure 6.1B**, leaving the oil phase as a liquid with a pour (melting) point of ~ -100 °C liquid. The partially-frozen samples were transferred to a lyophilizer and maintained under vacuum for at least 6 h. We have also frozen both the hydrogel particles and the oil using liquid N_2, which resulted in the formation of all-frozen samples undergoing oil melting within a few minutes during lyophilization. Regardless of the freezing method, the MEtoP process results in the formation of fine powders that can readily be resuspended or converted to an aqueous suspension.

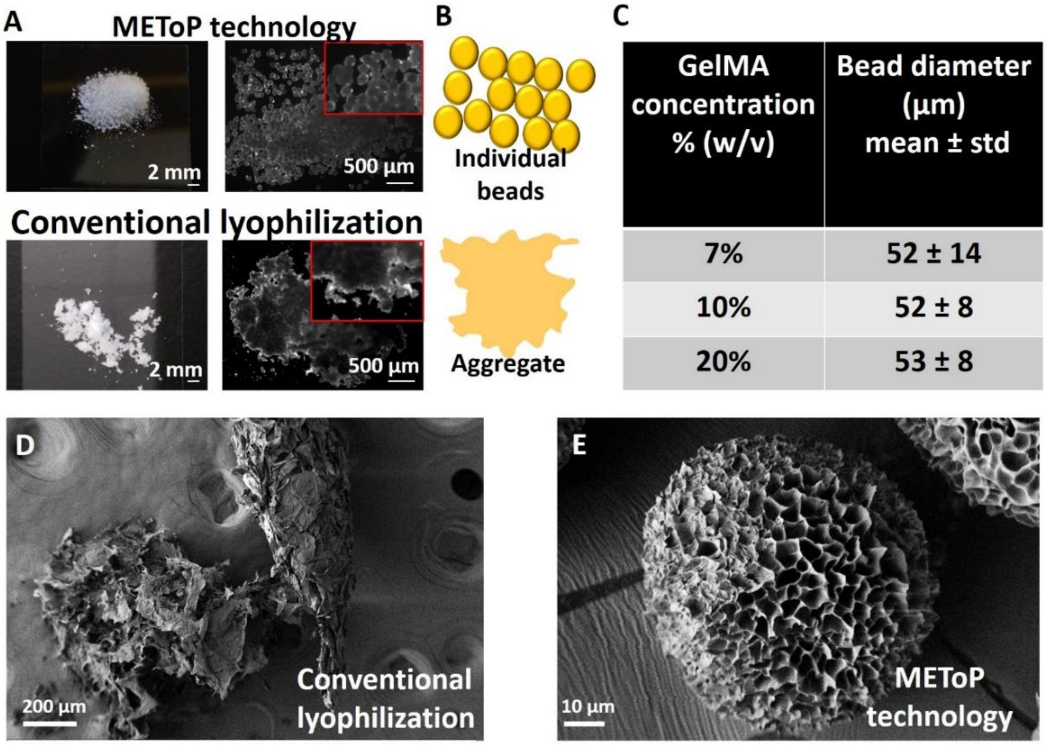
A
METoP technology
2 mm
500 µm
Conventional lyophilization
2 mm
500 µm
B
Individual beads
Aggregate
C
D
200 µm
Conventional lyophilization
E
10 µm
METoP technology

GelMA concentration % (w/v)	Bead diameter (µm) mean ± std
7%	52 ± 14
10%	52 ± 8
20%	53 ± 8

Figure 6.2 *Comparison between the powders produced via the MEtoP technology and conventional freeze-drying. A) Schematic of individual beads produced via the MEtoP technology compared to those yielded through the conventional freeze-drying. C) The average size of GelMA aerogel beads obtained from the MEtoP technology showing that regardless of polymer concentration (7−20%), the bead size is uniform and depends only on the initial microgel size. SEM images of GelMA beads post conventional lyophilization (D) and MEtoP processing (E).*

In **Figure 6.2**, the powder generated using the MEtoP technology is compared with the powder produced by freeze-drying the GelMA beads once exchanged into an aqueous phase (conventional lyophilization). At the macro-scale, the powder that was produced using the MEtoP technology had very fine particles as shown in **Figure 6.2A**, whereas the conventional lyophilization yielded large aggregated clumps. At the micro-scale, the dark field optical images of powders show that the microengineered powder was made up of extremely fine, segregated particles while the conventional method resulted in the aggregated particles often difficult to be individually distinguish. The products of these two methods are schematically shown in **Figure 6.2B**. The particle size of bead powders including 7%, 10%, and 20% of GelMA, presented in **Figure 6.2C**, shows that independent of the biopolymer concentration, the dried beads have an average particle diameter of ~ 50 µm. This is almost half of the freshly-prepared beads as a result of water removal and biopolymer shrinkage. Images of GelMA (7-20%) powders and their constituent beads are presented in **Figure 6.3**.

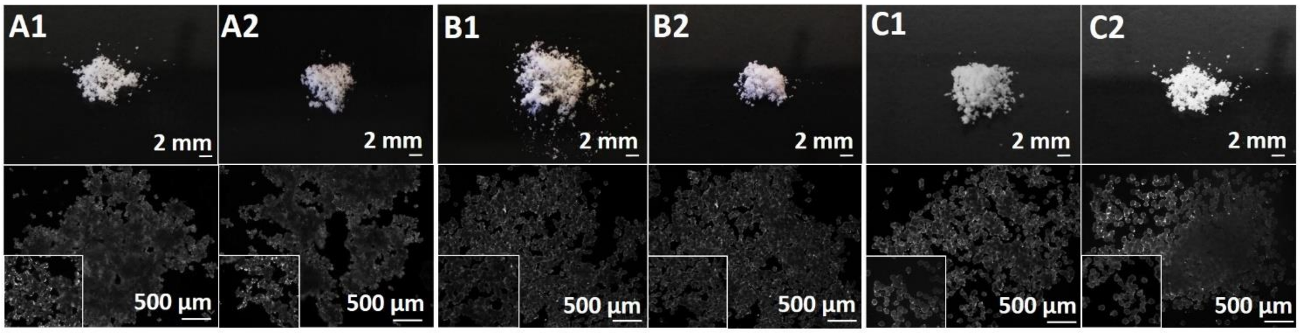

Figure 6.3 *Effect of freeze-drying on GelMA microbeads converted to powders via the MEtoP method. Powder GelMA obtained from microgels including (A) 7% w/v, (B) 10% w/v, and (C) 20% w/v of polymer. The freezing process was conducted (1) at -80 °C followed by 5 min of liquid N_2-assisted freezing or (2) without the liquid N_2 freezing step.*

As can be seen in the figure, there is no significant difference between the powders prepared via an extended liquid N_2 freezing compared to the ones that were only frozen at -80 °C. Accordingly, even the temporary freezing of oil does not have any effect on the outcome of MEtoP technology, attesting to its robustness in producing fine, segregated beads. To assess the capability of lyophilized powders in recuperating their original shape and size, the time evolution of their diameter upon resuspension in DPBS was measured using optical microscopy. **Figure 6.4** shows that the dry microbeads produced via the MEtoP method swell to ~80% of their original (in-emulsion) size almost immediately after introducing them into the aqueous phase. The swelling of the microengineered beaded powder completes in less than 10 min, resulting in fully swollen beads with sizes similar to the freshly-prepared beads (**Figure 6.4B**).

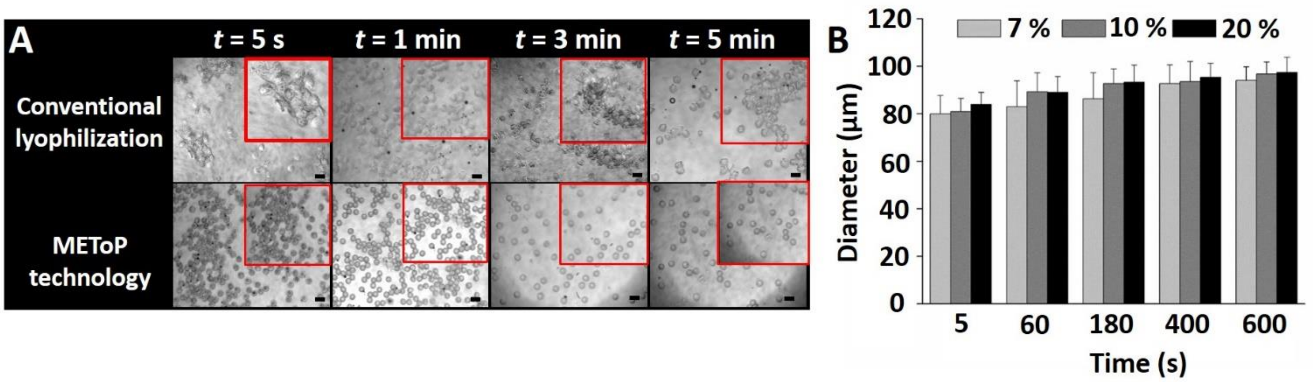

Figure 6.4 *Swelling recovery of beaded GelMA powders produced via the MEtoP technology compared with the conventional method. (A) The swelling time-lapse of powder particles obtained from the MEtoP and conventional methods. (B) The diameter of GelMA beads produced via the MEtoP method undergoing swelling in cold DI water versus incubation time.*

In the contrary, the powder produced via the conventional method does not yield individual beads and remain permanently aggregated in the aqueous medium. This attests to the promising potential of MEtoP in providing an infrastructure for preserving the macro- and microscale properties of lyophilized substances. Images of the rehydration of beads produced via the MEtoP technology (with or without the liquid N_2 freezing step) are presented in **Figure 6.5**. As can be seen in this figure, the beads regain their original shape and size within a few minutes regardless of the freezing method and biopolymer concentration.

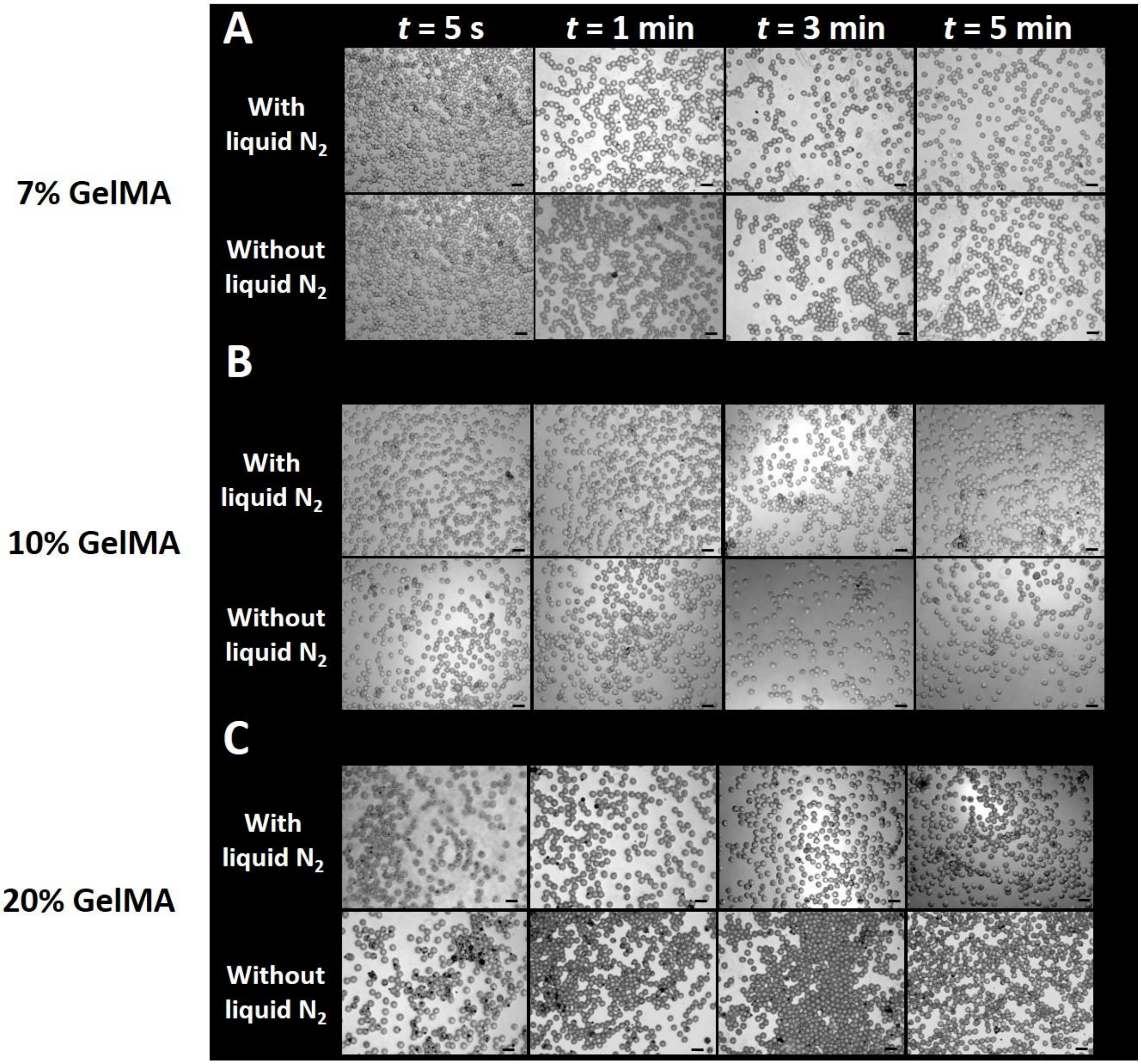
A
t = 5 s
t = 1 min
t = 3 min
t = 5 min
With liquid N_2
Without liquid N_2
7% GelMA
B
With liquid N_2
Without liquid N_2
10% GelMA
C
With liquid N_2
Without liquid N_2
20% GelMA

Figure 6.5 *Effect of freeze-drying on the swelling recovery of GelMA microbeads prepared via the MEtoP method. Panels show the rehydration dynamics of powder GelMA obtained from microgels including (A) 7% w/v, (B) 10% w/v, and (C) 20% w/v of polymer. The freezing process was conducted with or without liquid N_2-assisted post-freezing.*

The preservation of chemical cues in photoactive hydrogels, such as GelMA, during MEtoP processing was compared with the hydrogels underwent the conventional lyophilization method. To this end, hydrated powders, shown in **Figure 6.6A**, were resuspended in a solution of DPBS including a UV-active photoinitiator. The resuspended beads were exposed to UV light to initiate the chemical crosslinking of methacryloyl or vinylsulfone groups. **Figure 6.6B** shows the crosslinked scaffolds post-UV light exposure. The scaffolds that were constructed from the beads produced via the conventional method were not able to hold their shape due to the lack of effective bead-bead chemical conjugation. Interestingly, the crosslinking of beads prepared via the MEtoP method formed self-standing hydrogel constructs, which implies that the photoactivated bead-bead annealing has taken place successfully.

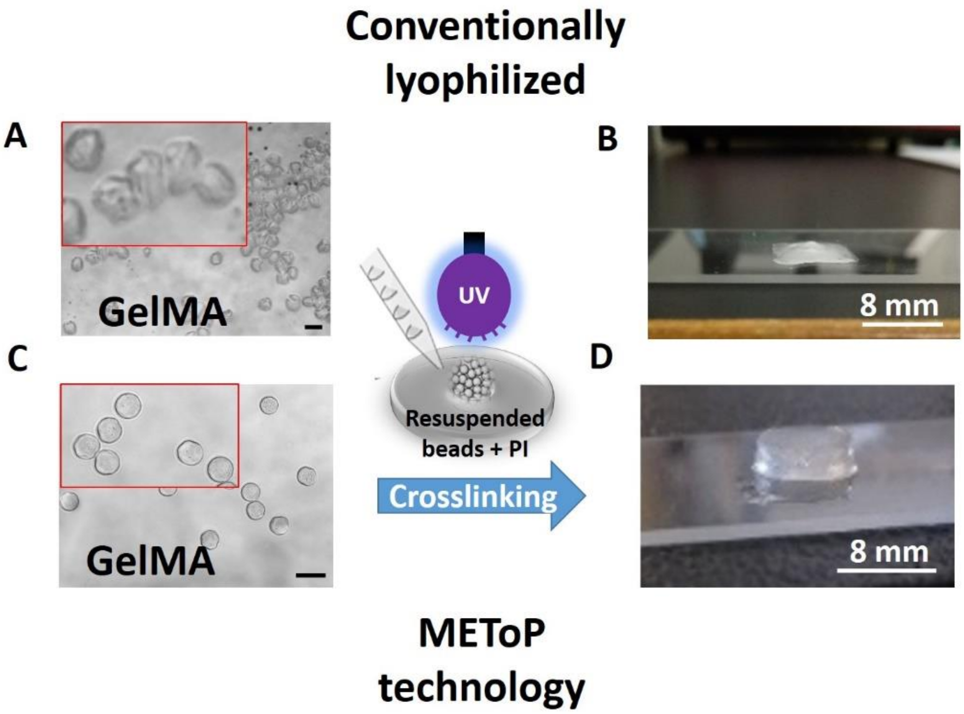

Figure 6.6 A*nnealing capability of hydrogel beads (GelMA) prepared using the MEtoP technology or conventional lyophilization. (A and C) Optical images of hydrogel beads prepared via the conventional method and MEtoP technology*. *(B- D) Exposure to UV light in the presence of a photoinitiator (PI).*

The properties of annealed scaffolds were evaluated to investigate the differences between the hydrogels prepared from the MEtoP beads compared to the freshly-prepared microgels. **Figure 6.7** presents the macro-scale and micro-scale properties of the annealed scaffolds. Optical images of annealed GelMA scaffolds made up of MEtoP beads including 7% (**Figure 6.7A**), 10% (**Figure 6.7B**), and 20% (**Figure 6.7C**) GelMA show that even at low concentrations of GelMA (i.e., soft beads), MEtoP beads are able to form a self-standing hydrogel construct. At the microscale, all these hydrogels are made up of annealed microspheres that form a packed structure with permanent micropores (**Figure 6.7 (G-I)**). Infusing a large fluorescent dye (FITC-dextran) in the pores of hydrogels enabled us to image layers of these constructs. **Figures 7** G-I show examples of *z*-stacks obtained from confocal microscopy of hydrogels constructed from MEtoP GelMA beads with 7%, 10%, and 20% biopolymer, respectively. The images were processed using a custom-built Matlab code in which the fluorescent-labeled spaces were filled with varying diameters of spheres. The processed void spaces (examples shown in **Figures 6.7 J-L** from 70 stacks (height ~150 µm) provided the median pore diameter and void space fraction of annealed hydrogels. **Figure 6.7M** presents the median pore dimeter of hydrogels prepared via crosslinking the MEtoP beads (7-20 %) immediately, after 5 min, or after 10 min post-transferring to a PDMS mold. Regardless of the GelMA concentration, all the hydrogel samples attain a similar median pore diameter, which is almost independent of the incubation time. The pore dimeter of hydrogels fabricated from freshly-prepared GelMA microbeads is ~ 20 µm [30], which is almost identical to the MEtoP beaded gels. The median pore diameters of beaded scaffolds constructed from the freshly-prepared beads were similar to the MEtoP-based scaffolds (~18±2 µm). **Figure 6.7N** shows the void space fraction of annealed hydrogels. Similar to the pore dimeter, the void space is neither affected by the GelMA concentration nor it varies with the incubation time.

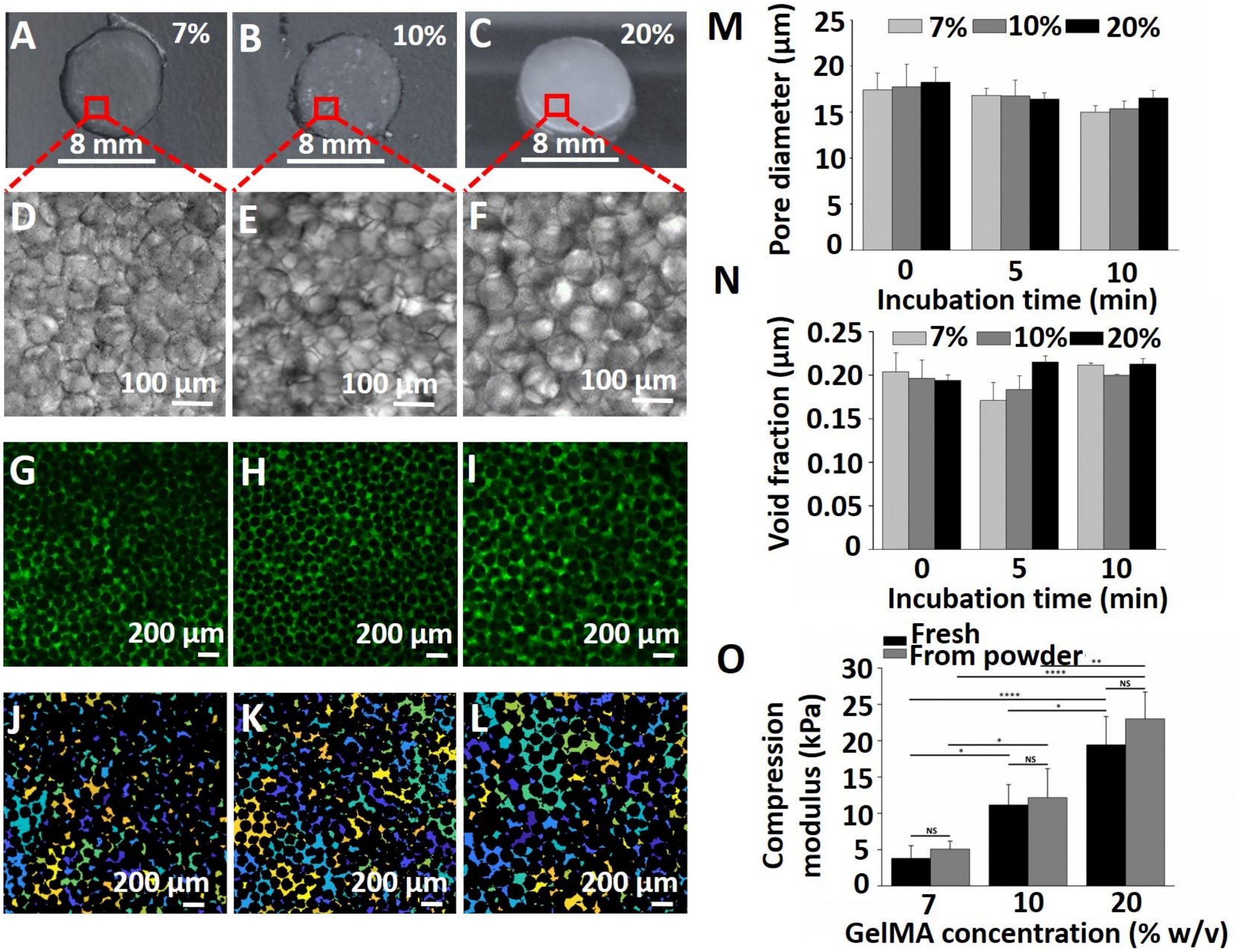

Figure 6.7 *Microstructure and mechanical strength of annealed hydrogels obtained from the MEtoP powders. Self-standing hydrogels may readily be constructed by annealing resuspended (A) 7, (B) 10, or (C) 20% GelMA beads, obtained from the METoP technology. Bright-field images of hydrogels in panels A−C are presented in panels D−F, respectively, which show packed structures made up of spherical beads. Two-dimensional (2D) slices of annealed beaded hydrogels obtained from confocal fluorescence microscopy show that regardless of the polymer concentrations (G: 7%, H: 10%, and I: 20%), the beads are able to make microporous structures. Analysis of 2D slices among the annealed beads with GelMA concentrations (J) ~7, (K) 10, and (L) 20%. (M) Median pore diameter of annealed beaded GelMA scaffolds versus pre-UV exposure incubation time. (N) Void space fraction for beaded GelMA scaffolds prepared using varying biopolymer concentration and precross-linking incubation time. (O) The compression moduli of beaded scaffolds. pValues lower than 0.05 (*p < 0.05), 0.01 (**p < 0.01), 0.001 (***p < 0.001), and 0.0001 (****p < 0.0001) indicated statistically significant differences.*

Such an excellent similarity between the MEtoP-based beaded hydrogels and the freshly-prepared ones attests to the unique capability of MEtoP in preserving the original properties of colloidal particles and macromolecules undergoing harsh lyophilization. To evaluate the strength of hydrogel constructs, compression tests were conducted. **Figure 6.7O** presents the compression modulus of annealed beaded hydrogels fabricated from MEtoP (powder) or freshly-prepared beads. Increasing the biopolymer concentrating increases the compression modulus; however, there is no significant difference between the compression modulus of beaded hydrogels fabricated from the fresh or MEtoP beads. The independency of porosity and void fraction has been shown for the microporous beaded GelMA hydorgels prepared from fresh beads [30]. **Figures 6.7 M-O** show that the MEtoP technology can provide powders that can generate swollen microbeads with identical physical and chemical properties to the freshly-prepared, never dried microgels.

6.5 Conclusion

Preserving the physical and chemical properties of macromolecules and colloids post-drying is of utmost importance in a broad range of application in order to avoid contamination, to allow stability and a to find proprer method for storage and shipment. We have invented a method called the MEtoP (microengineered emulsion-to-powder) technology involving the stabilization of a dispersed phase using an engineered oil, which acts as a protective layer and preserves the properties of dispersed phase during lyophilization. The engineered oil phase is heat conductive and can readily be evaporated, which provides a physical barrier among the dispersed phase components while permitting proper heat and mass transfer. For the first time, we show that, within a few hours, emulsions can be readily converted to powders that can be resuspended and gain their original properties. As a model system, we show that MEtoP was able to convert functionalized gelatin (GelMA) hydrogel microbeads into finely-separated spherical particles that regain their physical and chemical properties within minutes’ post-suspension.

Chapter 7

General Conclusion

Cells in the body perform bioactivities in response to the stimulation from a highly complex 3D microenvironment. Introduction of 3D cell culture approaches, aiming to model the *in vivo* interactions of tissues, has opened new possibilities for morphological and functional characterizations. Hydrogels are commonly chosen and adapted for use as support matrices for 3D cell cultures. Many different techniques have been used to add microstructure to hydrogels for various biomedical applications.

The aim of this thesis is to fabricate and characterize biopolimeric microbeads by dripping and microfluidic techniques to be applied in soft tissue engineering. To these purpose microbeads should be biocompatible, stable, injectable, and should demonstrate desired and predictable degradation kinetics.

In particular, in this thesis, microbeads are used as a micro-unit to construct a modular (granular) scaffold for soft tissue engineering, focusing on CNS tissue.

Firstly, the ability of chitosan to favor spontaneous neuronal adhesion is shown; the bioadhesive and bioactivity properties lead these material to be considered as an alternative biopolymer to the standard and expensive adhesion factors used in neurobiology, supporting a natural development of neuronal cells and a homogeneous and highly connected network, reducing laboratory reagents costs. Chitosan possesses excellent processability properties to be used by different techniques (spray coating, dip coating) for coating thin layers onto any kind of substrates and producing a desired micropattern through the use of stencil masks.

The stability and ability Chitosan microbeads, obtained by dripping technique, to sustain neuronal cells are demonstrated. Due to their mechanical properties, porosity, and availability of functional groups, these microbeads are a promising scaffold for the development of 3D neuronal networks towards the design and implementation of brain-on-a-chip microsystems for research into basic neuroscience and drug screening.

Different protocols for the enzymatic degradation chitosan microbeads have been developed. Specifically, the degradation can be controlled by using two enzymes, Chitosanase and β-Glucosidase.

The microbeads can be completely degraded by two enzymes when cells are not present. However, it is hard to observe a complete degradation of the 3D microbeads scaffold seeded with cells, due to the fact that neuronal cells develop a dense and huge network around the scaffold that tend to create a mask which prevent the homogenous diffusion of the enzyme molecules inside the hydrogel. Interestingly, the two enzymes do not induce any toxic response onto neuronal networks

Finally, GelMA microbeads have been obtained by a microfluidic device and an innovative and fast method to convert emulsion to powder has been developed. MEtoP (microengineered emulsion-to-powder) technology is based on the stabilization of the dispersed phase in an engineered oil/surfactant continuous phase, followed by the deep-freezing and lyophilization. This technology decreases the risk of contamination, degradation, facilitating shipment and decrease processing energy and cost, preserving physical and chemical properties of the systems.

All microbeads based-models proposed in this thesis, offer a higher reproducibility and the ability to support cells culture. These granular systems convey further advantages. Microbeads hydrogel fluidize when compressed, this is a property known as shear thinning, that increases the injectability property of these systems.

Furthermore, cells can be mixed homogeneously with microbeads enabling the adhesion of the cells directly on their surface, this method can avoid the effect of settling following mixing. The engineered microbeads with controlled sizes, monodispersity, diverse morphologies, and specific functions are gain an important role in biomedical fields. Microbeads systems could be considered for their shear thinning properties as an alternative ink for 3D bioprinters and moreover, could facilitate cell infiltration promoting, *in vitro* vascularization.

Finally, the microbeads -models developed in this thesis can found application as microsystems to model disease and for drug screening.

Chapter 8

Bibliography

1. *Langer R, Vacanti JP. Tissue engineering. Science. 1993 May 14;260(5110):920-6.*

2. *T. Dvir, et al., Nanotechnological strategies for engineering complex tissues, Nat. Nanotechnol. 6 (1) (2011) 13e22.*

3. *E. Cukierman, et al., Taking cell-matrix adhesions to the third dimension, Science 294 (5547) (2001) 1708e1712*

4. *Kim, K., and Evans, G. (2005). "Tissue engineering: the future of stem cells," in Topics in Tissue Engineering, eds N. Ashammakhi and R. L. Reis, Vol. 2, Chap. 13.*

5. *F. Pampaloni, E.G. Reynaud, E.H. Stelzer, The third dimension bridges the gap between cell culture and live tissue, Nat. Rev. Mol. Cell Biol. 8 (10) (2007) 839e845.*

6. *D.B. Kolesky, et al., 3D bioprinting of vascularized, heterogeneous cell-laden tissue constructs, Adv. Mater. 26 (19) (2014) 3124e3130.*

7. *K.H. Benam, et al., Engineered in vitro disease models, Annu. Rev. Pathol. 10 (2015) 195e262.*

8. *D. Huh, et al., Microfabrication of human organs-on-chips, Nat. Protoc. 8 (11) (2013) 2135e2157.*

9. *B. Weigelt, C.M. Ghajar, M.J. Bissell, he need for complex 3D culture models to unravel novel pathways and identify accurate biomarkers in breast cancer, Adv. Drug Deliv. Rev. 69e70 (2014) 42e51.*

10. *J. Lee, et al., In vitro toxicity testing of nanoparticles in 3D cell culture, Small 5 (10) (2009) 1213e1221.*

11. *M.W. Tibbitt, K.S. Anseth, Hydrogels as extracellular matrix mimics for 3D cell culture, Biotechnol. Bioeng. 103 (4) (2009) 655e663.*

12. *S. Breslin, L. O'Driscoll, Three-dimensional cell culture: the missing link in drug discovery, Drug Discov. Today 18 (5e6) (2013) 240e249.*

13. *A. Roth, T. Singer, The application of 3D cell models to support drug safety assessment: opportunities & challenges, Adv. Drug Deliv. Rev. 69e70 (2014) 179e189.*

14. *Nichol, J. W., and Khademhosseini, A. (2009). Modular tissue engineering: engineering biological tissues from the bottom up. Soft Matter 5, 1312–1319.*

15. *Causa, F., Netti, P. A., and Ambrosio, L. (2007). A multi-functional scaffold for tissue regeneration: the need to engineer a tissue analogue. Biomaterials 28, 5093–5099.*

16. *Mattei, G., Giusti, S., and Ahluwalia, A. (2014). Design criteria for generating physiologically relevant in vitro models in bioreactors. Processes 2, 548–569.*

17. *Griffith, L. G., and Swartz, M. A. (2006). Capturing complex 3D tissue physiology in vitro. Nat. Rev. Mol. Cell Biol. 7, 211–224.*

18. *Raimondi, M. T. (2006). Engineered tissue as a model to study cell and tissue function from a biophysical perspective. Curr. Drug Discov. Technol. 3, 245–268.*

19. *Martini, L., Fini, M., Giavaresi, G., and Giardino, R. (2001). Sheep model in orthopedic research: a literature review. Comp. Med. 51, 292–299.*

20. *Massai, D., Cerino, G., Gallo, D., Pennella, F., Deriu, M. A., Rodriguez, A., et al. (2013). Bioreactors as engineering support to treat cardiac muscle and vascular disease. J. Healthc. Eng. 4, 329–370.*

21. *D. J. Mooney, D. F. Baldwin, N. P. Suh, J. P. Vacanti, R. Langer, Biomaterials 1996, 17, 1417.*

22. *L. D. Harris, B. S. Kim, D. J. Mooney, J. Biomed. Mater. Res. 1998, 42, 396.*
23. *A. G. Mikos, Y. Bao, L. G. Cima, D. E. Ingber, J. P. Vacanti, R. Langer, J. Biomed. Mater. Res. 1993, 27, 183.*

24. *DW Hutmacher, Scaffolds in tissue engineering bone and cartilage. The biomaterials: Silver jubilee compendium, 2000 – Elsevier*

25. *Ch. Schugens, V. Maquet, C. Grandfils, R. Jerome, Ph. Teyssie, Biodegradable and macroporous polylactide implants for cell transplantation: 1. Preparation of macroporous polylactide supports by solid-liquid phase separation, Polymer, olume 37, Issue 6,1996,*

26. *Nam, Y.S. and Park, T.G. (1999), Porous biodegradable polymeric scaffolds prepared by thermally induced phase separation. J. Biomed. Mater. Res., 47: 8-17.*

27. *K. Whang, C.H. Thomas, K.E. Healy, G. Nuber, A novel method to fabricate bioabsorbable scaffolds, Polyme, Volume 36, Issue 4, 1995*

28. *, Antonios G Mikos, Amy J Thorsen, Lisa A Czerwonka, Yuan Bao, Robert Langer, Douglas N Winslow, Joseph P Vacanti, Preparation and characterization of poly (l-lactic acid) foams, Polymer, Volume 35, Issue 5,1994,*

29. *Antonios G. Mikos, Georgios Sarakinos, Susan M. Leite, Joseph P. Vacant, Robert Langer, Laminated three-dimensional biodegradable foams for use in tissue engineering, Biomaterials, Volume 14, Issue 5, 1993.*

30. *Yuana, B.M. Chesnutta, G. Utturkara, W.O. Haggarda, Y. Yangb, J.L. Ongb, J.D. Bumgardner; The effect of cross-linking of chitosan microspheres with genipin on protein release. Carbohydrate Polymers Volume 68, Issue 3, 5 April 2007, Pages 561-567*

31. *C.A. Custodio, et al., Functionalized microparticles producing scaffolds in combination with cells, Adv. Funct. Mater. 24 (10) (2014) 1391e1400.*

32. *Jaiswal, N., Haynesworth, S.E., Caplan, A.I. and Bruder, S.P. (1997), Osteogenic differentiation of purified, culture-expanded human mesenchymal stem cells in vitro. J. Cell. Biochem., 64: 295-312.*

33. *Schnaper, H.W., Kleinman, H.K. Regulation of cell function by extracellular matrix. Pediatr Nephrol 7, 96–104 (1993)*

34. *F Grinnell, J R Head, J Hoffpauir; Fibronectin and cell shape in vivo: studies on the endometrium during pregnancy. J Cell Biol 1 September 1982; 94 (3): 597–606.*

35. *M A Hadley, S W Byers, C A Suárez-Quian, H K Kleinman, M Dym; Extracellular matrix regulates Sertoli cell differentiation, testicular cord formation, and germ cell development in vitro. J Cell Biol 1 October 1985; 101 (4): 1511–1522.*

36. *Watt, F., Huck, W. Role of the extracellular matrix in regulating stem cell fate. Nat Rev Mol Cell Biol 14, 467–473 (2013)*

37. *Samuel Schmidt, Peter Friedl, Interstitial cell migration: integrin-dependent and alternative adhesion mechanisms, Cell and Tissue Research January 2010, 339:83*

38. *Christian Frantz, Kathleen M. Stewart, Valerie M. Weaver, The extracellular matrix at a glance, Journal of Cell Science 2010 123: 4195-4200; N. Zagris, Micron 2001, 32, 42.*

39. *N. H. Brown, Cold Spring Harb. Perspect. Biol. 2011, 3, 1.*

40. *Andrew Latimer, Jason R. Jessen, Extracellular matrix assembly and organization during zebrafish gastrulation, Matrix Biology, Volume 29, Issue 2, 2010.*

41. *Tania Rozario, Douglas W. De Simone, The extracellular matrix in development and morphogenesis: A dynamic view, Developmental Biology, Volume 341, Issue 1, 2010.*

42. *Sakai, T., Larsen, M. & Yamada, K. Fibronectin requirement in branching morphogenesis. Nature 423, 876–881 (2003).*

43. *S. Stahl, S. Weitzman, J.C. Jones, The role of laminin-5 and its receptors in mammary epithelial cell branching morphogenesis, Journal of Cell Science 1997 110: 55-63; M.-H. Barcellas-Hoff, M. J. Bissell, J. Cell Sci. 1987, 8, 327.*

44. *Mirren Charnley, Marcus Textor, Ali Khademhosseini, Matthias P. Lutolf, Integration column: microwell arrays for mammalian cell culture, Integrative Biology, Volume 1, Issue 11-12, December 2009, Pages 625–634,*

45. *Yukiko Tsuda, Yuya Morimoto, and Shoji Takeuch, Monodisperse Cell-Encapsulating Peptide Microgel Beads for 3D Cell Culture, Langmuir 2010 26 (4), 2645-2649.*

46. *Baker, B. M. & Chen, C. S. Deconstructing the third dimension – how 3D culture microenvironments alter cellular cues. J. Cell Sci. 125, 3015–3024 (2012).*

47. *H.J. Häuselmann, M.B. Aydelotte, B.L. Schumacher, K.E. Kuettner, S.H. Gitelis, E. J.-M.A. Thonar, Synthesis and Turnover of Proteoglycans by Human and Bovine Adult Articular Chondrocytes Cultured in Alginate Beads, Matrix, Volume 12, Issue 2, 1992.*

48. *J. Kisiday, M. Jin, B. Kurz, H. Hung, C. Semino, S. Zhang, A. J. Grodzinsky, Self-assembling peptide hydrogel fosters chondrocyte extracellular matrix production and cell division: Implications for cartilage tissue repair PNAS July 23, 2002 99 (15) 9996-10001; Proc. Natl. Acad. Sci. USA 2002, 99, 9996.*

49. *S S Mok, K Masuda, H J Häuselmann, M B Aydelotte and E J Thonar Aggrecan synthesized by mature bovine chondrocytes suspended in alginate. Identification of two distinct metabolic matrix pools. 1994. The Journal of Biological Chemistry 269, 33021-33027.*

50. *Shulamit Levenberg, Ngan F. Huang, Erin Lavik, Arlin B. Rogers, Joseph Itskovitz-Eldor, and Robert Lange. Differentiation of human embryonic stem cells on three-dimensional polymer scaffolds. PNAS October 28, 2003 100 (22) 12741-12746*

51. *Aja Aravamudhan, Daisy M. Ramos, Ahmed A. Nada, Sangamesh G. Kumbar, Chapter 4 - Natural Polymers: Polysaccharides and Their Derivatives for Biomedical Applications, Natural and Synthetic Biomedical Polymers, Elsevier, 2014, Pages 67-89.*

52. *Kristi S. Anseth, Christopher N. Bowman, Lisa Brannon-Peppas, Mechanical properties of hydrogels and their experimental determination, Biomaterials, 1996, Pages 1647-1657.*

53. *Ahmed EM. Hydrogel: Preparation, characterization, and applications: A review. J Adv Res. 2015;6(2):105–121.*

54. *Yeung T, Georges PC, Flanagan LA, Marg B, Ortiz M, Funaki M, Zahir N, Ming W, Weaver V, Janmey PA. Effects of substrate stiffness on cell morphology, cytoskeletal structure, and adhesion. Cell Motil. Cytoskelet. 2005; 60(1):24–34.*

55. *Smith Callahan LA, Ganios AM, Childers EP, Weiner SD, Becker ML. Primary human chondrocyte extracellular matrix formation and phenotype maintenance using RGD-derivatized PEGDM hydrogels possessing a continuous Young's modulus gradient. Acta BioMater. 2013; 9(4):6095–6104.*

56. *Lee C, Grodzinsky A, Spector M. The effects of cross-linking of collagen-glycosaminoglycan scaffolds on compressive stiffness, chondrocyte-mediated contraction, proliferation and biosynthesis. Biomaterials. 2001 Dec; 22(23):3145–3154.*

57. *Mih JD, Marinkovic A, Liu F, Sharif AS, Tschumperlin DJ. Matrix stiffness reverses the effect of actomyosin tension on cell proliferation. J. Cell Sci. 2012 Dec; 125(Pt 24):5974–5983.*

58. *Provenzano PP, Keely PJ. Mechanical signaling through the cytoskeleton regulates cell proliferation by coordinated focal adhesion and Rho GTPase signaling. J. Cell Sci. 2011 Apr; 124(Pt 8):1195–1205.*

59. *Tan PS, Teoh SH. Effect of stiffness of polycaprolactone (PCL) membrane on cell proliferation. Mater. Sci. Eng. C. 2007 Mar; 27(2):304–308.*

60. *Banerjee S, Marchetti MC. Controlling cell-matrix traction forces by extracellular geometry. New J. Phys. 2013; 15(3):35015.*

61. *Park JS, Chu JS, Tsou AD, Diop R, Tang Z, Wang A, Li S. The effect of matrix stiffness on the differentiation of mesenchymal stem cells in response to TGF-β. Biomaterials. 2011; 32:3921–3930.*

62. *Ren K, Crouzier T, Roy C, Picart C. Polyelectrolyte multilayer films of controlled stiffness modulate myoblast cells differentiation. Adv. Funct. Mater. 2008 Jan; 18(9):1378–1389.*

63. *V Shih Y-R, Tseng K-F, Lai H-Y, Lin C-H, Lee OK. Matrix stiffness regulation of integrin-mediated mechanotransduction during osteogenic differentiation of human mesenchymal stem cells. J. Bone Miner. Res. 2011 Apr; 26(4):730–738.*

64. *153. Wang L-S, Boulaire J, Chan PPY, Chung JE, Kurisawa M. The role of stiffness of gelatin-hydroxyphenylpropionic acid hydrogels formed by enzyme-mediated crosslinking on the differentiation of human mesenchymal stem cell. Biomaterials. 2010 Nov; 31(33):8608–8616.*

65. *Wasupalli, Geeta K., and Devendra Verma. "Polysaccharides as biomaterials." Fundamental Biomaterials: Polymers. Woodhead Publishing, 2018. 37-70.*

66. *Ashley R. Murphy, Andrew Laslett, Carmel M. O'Brien, Neil R. Cameron, Scaffolds for 3D in vitro culture of neural lineage cells, Acta Biomaterialia, Volume 54, 2017, 1-20.*

67. *Sheikhi A., de Rutte J, Haghniaz R, Akouissi O, Sohrabi A, Di Carlo D, Khademhosseini A., Microfluidic-enabled bottom-up hydrogels from annealable naturally-derived protein microbeads, Biomaterials, Volume 192, 2019.*

68. *Julian George, Chia-Chen Hsu, Linh Thuy Ba Nguyen, Hua Ye, Zhanfeng Cui, Neural tissue engineering with structured hydrogels in CNS models and therapies, Biotechnology Advances, 2019.*

69. *Velasco D, Tumarkin E, Kumacheva E Microfluidic encapsulation of cells in polymer microgels. Small. 2012 Jun 11; 8(11):1633-42.*

70. *Shum HC, Kim JW, Weitz DA Microfluidic fabrication of monodisperse biocompatible and biodegradable polymersomes with controlled permeability. J Am Chem Soc. 2008 Jul 23; 130(29):9543-9.*

71. *Griffin DR, Weaver WM, Scumpia PO, Di Carlo D, Segura T. Accelerated wound healing by injectable microporous gel scaffolds assembled from annealed building blocks. Nat Mater. 2015 Jul; 14(7):737-44.*

72. *Li W, Zhang L, Ge X, et al. Microfluidic fabrication of microparticles for biomedical applications. Chem Soc Rev. 2018;47(15):5646–5683.*

73. *Munmaya Mishra. Chapter 9 Microencapsulation by Dripping and Jet Break-Up. Handbook of Encapsulation and Controlled Release. November 2015.*

74. *Duncanson WJ, Lin T, Abate AR, Seiffert S, Shah RK, Weitz DA Microfluidic synthesis of advanced microparticles for encapsulation and controlled release. Lab Chip. 2012 Jun 21; 12(12):2135-45.*

75. *Wang W, Zhang MJ, Chu LY. Functional polymeric microparticles engineered from controllable microfluidic emulsions. Acc Chem Res. 2014 Feb 18; 47(2):373-84*

76. *Liu D, Zhang H, Fontana F, Hirvonen JT, Santos HA. Microfluidic-assisted fabrication of carriers for controlled drug delivery. Lab Chip. 2017 May 31; 17(11):1856-1883.*

77. *Jiang W, Li M, Chen Z, Leong KW. Cell-laden microfluidic microgels for tissue regeneration. Lab Chip. 2016 Nov 15; 16(23):4482-4506.*

78. *Simone Allazetta, Matthias P Lutolf, Stem cell niche engineering through droplet microfluidics, Current Opinion in Biotechnology, Volume 35, 2015, Pages 86-93.*

79. *Zhi Zhu, Chaoyong James Yan, Hydrogel Droplet Microfluidics for High-Throughput Single Molecule/Cell Analysis, Acc. Chem. Res. 2017, 50, 1, 22-31.*

80. *Tatiana Trantidou, Mark Friddin, Yuval Elani, Nicholas J. Brook, Robert V. Law, John M. Seddon, Oscar Ces, Engineering Compartmentalized Biomimetic Micro- and Nanocontainers, ACS Nano 2017, 11, 7, 6549-6565.*

81. *Koki Kamiya and Shoji Takeuchi, Giant liposome formation toward the synthesis of well-defined artificial cells, J. Mater. Chem. B, 2017, 5, 5911-5923*

82. *Tae Yong Lee a, Tae Min Choi a, Tae Soup Shim bc, Raoul A. M. Frijns ad and Shin-Hyun Kim, Microfluidic production of multiple emulsions and functional microcapsules, Lab Chip, 2016, 16, 3415-3440.*

83. *Ju Hyeon Kim, Tae Yoon Jeon, Tae Min Choi, Tae Soup Shim, Shin-Hyun Kim, Seung-Man Yang, Droplet Microfluidics for Producing Functional Microparticles, Langmuir 2014, 30, 6, 1473-1488.*

84. *Heida, T., Neubauer, J. W., Seuss, M., Hauck, N., Thiele, J., Fery, A., Mechanically Defined Microgels by Droplet Microfluidics, Macromol. Chem. Phys. 2017, 218, 1600418.*

85. *J. Thiele, Polymer Material Design by Microfluidics Inspired by Cell Biology and Cell-Free Biotechnology, Macromol. Chem. Phys., 2017, 218, 1600429*

86. *Maitra, Jaya & Shukla, Vivek. (2014). Cross-linking in hydrogels - a review. Am J Polym Sci. 4. 25-31.*

87. *Zhu J, Marchant RE. Design properties of hydrogel tissue-engineering scaffolds. Expert Rev Med Devices. 2011;8(5):607–626. doi:10.1586/erd.11.27*

88. *Pasco S, Ramont L, Maquart FX, Monboisse JC. Biological effects of collagen I and IV peptides. J. Soc. Biol. 2003; 197: 31–9.*

89. *Akiyama SK. Integrins in cell adhesion and signaling. Hum. Cell 1996; 9:181–6.5.*

90. *Sephel GC, Kennedy R, Kudravi S. Expression of capillary basement membrane components during sequential phases of wound angiogenesis. Matrix Biol. 1996; 15: 263–79.*

91. *Raman R, Sasisekharan V, Sasisekharan R. Structural insights into biological roles of protein-glycosaminoglycan interactions. Chem. Biol. 2005; 12: 267–77.*

92. *Olutoye OO, Barone EJ, Yager DR, Uchida T, Cohen IK, Diegelmann RF. Hyaluronic acid inhibits fetal platelet function: implications in scarless healing. J. Pediatr. Surg. 1997; 32: 1037–40.*

93. *Tabibzadeh S. Homeostasis of extracellular matrix by TGF-beta and lefty. Front. Biosci. 2002; 7: d1231–46.*

94. *Inkinen K, Wolff H, Lindroos P, Ahonen J. Connective tissue growth factor and its correlation to other growth factors in experimental granulation tissue. Connect. Tissue Res. 2003; 44: 19–29.*

95. *Presta M, Dell'era P, Mitola S, Moroni E, Ronca R, Rusnati M. Fibroblast growth factor/fibroblast growth factor receptor system in angiogenesis. Cytokine Growth Factor Rev. 2005; 16: 159–78.*

96. *Yamaguchi Y, Mann DM, Ruoslahti E. Negative regulation of transforming growth factor-beta by the proteoglycan decorin. Nature 1990; 346: 281–4.*

97. *Burridge K, Chrzanowska-Wodnicka M. Focal adhesions, contractility, and signaling. Annu Rev Cell Dev Biol 1996; 12:463-518;*

98. *Mege RM, Gavard J, Lambert M. Regulation of cellcell junctions by the cytoskeleton. Curr Opin Cell Biol 2006; 18:541-8;*

99. *Handorfab A.M, Zhouab Y, Halanskia M.A & Liab WL. Tissue Stiffness Dictates Development, Homeostasis, and Disease Progression. Organogenesis 11(1):1-15, January 2015*

100. *Cox TR, Erler JT. Remodeling and homeostasis of the extracellular matrix: implications for fibrotic diseases and cancer. Dis Models Mechanisms 2011; 4:165-78.*

101. *Bonneh-Barkay D, Wiley CA. Brain extracellular matrix in neurodegeneration. Brain Pathol. 2009;19(4):573–585. doi:10.1111/j.1750-3639.2008.00195.*

102. *Bandtlow CE, Zimmermann DR. Proteoglycans in the developing brain: new conceptual insights for old proteins. Physiol Rev. 2000; 80:1267–1290.*

103. *Kim Y, Meade S.M., Chen K., Feng H., Rayyan J., Hess-Dunning A. and Ereifej E.S., Nano-Architectural Approaches for Improved Intracortical Interface Technologies. Evon S. Front. Neurosci., 2018.*

104. *George N, Geller HM. Extracellular matrix and traumatic brain injury. J Neurosci Res. 2018;96(4):573–588. doi:10.1002/jnr.24151.*

105. *Plantman S. Proregenerative properties of ECM molecules. BioMed research international. 2013; 2013:981695.*

106. *Letourneau PC, Madsen AM, Palm SL, Furcht LT. Immunoreactivity for laminin in the developing ventral longitudinal pathway of the brain. Dev Biol. 1988; 125:135–144.*

107. *Yao Y, Chen ZL, Norris EH, Strickland S. Astrocytic laminin regulates pericyte differentiation and maintains blood brain barrier integrity. Nature communications. 2014; 5:3413.*

108. *Wei YT, Tian WM, Yu X, Cui FZ, Hou SP, Xu QY, Lee IS. Hyaluronic acid hydrogels with IKVAV peptides for tissue repair and axonal regeneration in an injured rat brain. Biomedical materials (Bristol, England) 2007;2: S142–146.*

109. *Giblin SP, Midwood KS. Tenascin-C: Form versus function. Cell Adh Migr. 2015; 9:48–82.*

110. *Zhang Y, Anderson PN, Campbell G, Mohajeri H, Schachner M, Lieberman AR. Tenascin-C expression by neurons and glial cells in the rat spinal cord: changes during postnatal development and after dorsal root or sciatic nerve injury. J Neurocytol. 1995; 24:585–601.*

111. *Pesheva P, Probstmeier R. The yin and yang of Tenascin-R in CNS development and pathology. Prog Neurobiol. 2000; 61:465–493.*

112. *Cui H, Freeman C, Jacobson GA, Small DH. Proteoglycans in the central nervous system: role in development, neural repair, and Alzheimer's disease. IUBMB life. 2013; 65:108–120.*

113. *Miller GM, Hsieh-Wilson LC. Sugar-dependent modulation of neuronal development, regeneration, and plasticity by chondroitin sulfate proteoglycans. Exp Neurol. 2015; 274:115–125.*

114. *Tan CL, Kwok JC, Patani R, Ffrench-Constant C, Chandran S, Fawcett JW. Integrin activation promotes axon growth on inhibitory chondroitin sulfate proteoglycans by enhancing integrin signaling. J Neurosci. 2011; 31:6289–6295.*

115. *Thelin MA, Bartolini B, Axelsson J, Gustafsson R, Tykesson E, Pera E, Oldberg A, Maccarana M, Malmstrom A. Biological functions of iduronic acid in chondroitin/dermatan sulfate. The FEBS journal. 2013; 280:2431–2446.*

116. *Hikino M, Mikami T, Faissner A, Vilela-Silva AC, Pavao MS, Sugahara K. Oversulfated dermatan sulfate exhibits neurite outgrowth-promoting activity toward embryonic mouse*

hippocampal neurons: implications of dermatan sulfate in neuritogenesis in the brain. J Biol Chem. 2003; 278:43744–43754.

117. *Nandini CD, Itoh N, Sugahara K. Novel 70-kDa chondroitin sulfate/dermatan sulfate hybrid chains with a unique heterogeneous sulfation pattern from shark skin, which exhibit neuritogenic activity and binding activities for growth factors and neurotrophic factors. J Biol Chem. 2005;*

118. *Qiao D, Meyer K, Mundhenke C, Drew SA, Friedl A. Heparan sulfate proteoglycans as regulators of fibroblast growth factor-2 signaling in brain endothelial cells. Specific role for glypican-1 in glioma angiogenesis. J Biol Chem. 2003; 278:16045–16053.*

119. *Barnett MW, Fisher CE, Perona-Wright G, Davies JA. Signalling by glial cell line-derived neurotrophic factor (GDNF) requires heparan sulphate glycosaminoglycan. J Cell Sci. 2002; 115:4495–4503.*

120. *Kantor DB, Chivatakarn O, Peer KL, Oster SF, Inatani M, Hansen MJ, Flanagan JG, Yamaguchi Y, Sretavan DW, Giger RJ, Kolodkin AL. Semaphorin 5A is a bifunctional axon guidance cue regulated by heparan and chondroitin sulfate proteoglycans. Neuron. 2004; 44:961–975.*

121. *Yayon A, Klagsbrun M, Esko JD, Leder P, Ornitz DM. Cell surface, heparin-like molecules are required for binding of basic fibroblast growth factor to its high affinity receptor. Cell. 1991; 64:841–848.*

122. *Vlodavsky I, Miao HQ, Medalion B, Danagher P, Ron D. Involvement of heparan sulfate and related molecules in sequestration and growth promoting activity of fibroblast growth factor. Cancer Metastasis Rev. 1996; 15:177–186.*

123. *Neufeld G, Cohen T, Gengrinovitch S, Poltorak Z. Vascular endothelial growth factor (VEGF) and its receptors. FASEB J. 1999; 13:9–22.*

124. Dotti CG, Sullivan CA, Banker GA. The establishment of polarity by hippocampal neurons in culture. J Neurosci 1988, 8:1454 –1468.

125. Cecchelli R, Aday S, Sevin E, Almeida C, Culot M, Dehouck L, Coisne C, Engelhardt B, Dehouck MP, Ferreira L. A stable and reproducible human blood-brain barrier model derived from hematopoietic stem cells. PloS One. 2014; 9: e99733.

126. Blain, M.; Miron, VE.; Lambert, C.; Darlington, PJ.; Cui, Q-L.; Saikali, P.; Yong, VW.; Antel, JP. Isolation and culture of primary human CNS neural cells. In: Doering, LC., editor. Protocols for Neural Cell Culture. Humana Press; 2010. p. 87-104.

127. Hopkins AM, De Laporte L, Tortelli F, Spedden E, Staii C, Atherton TJ, Hubbell JA, Kaplan DL. Silk hydrogels as soft substrates for neural tissue engineering. Adv. Funct. Mater. 2013; 23:5140–5149.

128. Kay AR, Wong RK. Isolation of neurons suitable for patch-clamping from adult mammalian central nervous systems. J. Neurosci. Methods. 1986; 16:227–238.

129. S. Alagapan, E. Franca, L. Pan, S. Leondopulos, B. C. Wheeler, and T. B. DeMarse, "Structure, Function, and Propagation of Information across Living Two, Four, and Eight Node Degree Topologies," Front Bioeng Biotechnol, vol. 4, p. 15, 2016.

130. M. Frega, K. Linda, J. M. Keller, G. Gumus-Akay, B. Mossink, J. R. van Rhijn, et al., "Neuronal network dysfunction in a model for Kleefstra syndrome mediated by enhanced NMDAR signaling," Nat Commun, vol. 10, p. 4928, Oct 30 2019.

131. A. Vassallo, M. Chiappalone, R. De Camargos Lopes, B. Scelfo, A. Novellino, E. Defranchi, et al., "A multi-laboratory evaluation of microelectrode array-based measurements of neural network activity for acute neurotoxicity testing," Neurotoxicology, vol. 60, pp. 280-292, May 2017.

132. Hatten M., et al. Binding of developing mouse cerebellar cells to fibronectin: a possible mechanism for the formation of the external granular layer. J Neurosci. 1982 Sep;2(9):1195-206.

133. Stewart GR, Pearlman AL. Fibronectin-like immunoreactivity in the developing cerebral cortex. J Neurosci. 1987 Oct;7(10):3325-33.

134. Chun JJ, Shatz CJ. A fibronectin-like molecule is present in the developing cat cerebral cortex and is correlated with subplate neurons. J Cell Biol. 1988 Mar;106(3):857-72.

135. Liesi P, Silver J. Is astrocyte laminin involved in axon guidance in the mammalian CNS? Dev Biol. 1988 Dec;130(2):774-85.

136. Hagg T, Muir D, Engvall E, Varon S, Manthorpe M. Laminin-like antigen in rat CNS neurons: distribution and changes upon brain injury and nerve growth factor treatment. Hoffman, A.S., Hydrogels for biomedical applications. Ann N Y Acad Sci, 2001. 944: p. 62-73. Neuron. 1989 Dec;3(6):721-32.

137. Lochter A, Schachner M. Tenascin and extracellular matrix glycoproteins: from promotion to polarization of neurite growth in vitro. J Neurosci. 1993 Sep;13(9):3986-4000.

138. Banker G.m. The Development of Neuronal Polarity: A Retrospective View. J Neurosci. 2018 Feb 21;38(8):1867-1873.

139. Yavin E, Yavin Z. Attachment and culture of dissociated cells from rat embryo cerebral hemispheres on polylysinecoated surface. J Cell Biol. 1974 Aug;62(2):540-6.

140. Caceres A, Banker GA, Binder L. Immunocytochemical localization of tubulin and microtubule-associated protein 2 during the development of hippocampal neurons in culture. J Neurosci, 1986, 6:714 –722.

141. Letourneau PC. Possible roles for cell-to-substratum adhesion in neuronal morphogenesis. Dev Biol. 1975 May;44(1):77-91.

142. Letourneau PC. Cell-to-substratum adhesion and guidance of axonal elongation. Dev Biol. 1975 May;44(1):92-101.

143. Manthorpe M, Engvall E, Ruoslahti E, Longo FM, Davis GE, Varon S. Laminin promotes neuritic regeneration from cultured peripheral and central neurons. J Cell Biol. 1983 Dec;97(6):1882-90.

144. Buettner HM1, Pittman RN. Quantitative effects of laminin concentration on neurite outgrowth in vitro. Dev Biol. 1991 Jun;145(2):266-76.

145. Goslin K, Schreyer DJ, Skene JHP, Banker G (1990) Changes in the distribution of GAP-43 during the development of neuronal polarity. J Neurosci 10:588-602.

146. Davis L, Banker G, Steward 0 (1987) Selective dendritic transport of RNA in hippocampal neurons in culture. Nature 330:477+79.

147. Lochter A and Schachner M., Tenascin and Extracellular Matrix Glycoproteins: From Promotion to Polarization of Neurite Growth in vitro. The Journal of Neuroscience, September 1993, 13(g): 3988-4000.

148. Baas PW, Deitch JS, Black MM, Banker GA (1988) Polarity orientation of microtubules in hippocampal neurons: uniformity in the axon and nonuniformity in the dendrites. Proc Nat1 Acad Sci USA 85:8335-8339.

149. S. Das, A. Carnicer-Lombarte, J. W. Fawcett and U. Bora, Bio-inspired nano tools for neuroscience, Prog. Neurobiol., 2016, 142,1 –22. 7.

150. *P. Hao, H. Duan, F. Hao, L. Chen, M. Sun, K. S. Fan, et al., Neural repair by NT3-chitosan via enhancement of endogenous neurogenesis after adult focal aspiration brain injury, Biomaterials, 2017, 140, 88 –102. 8*

151. *E. Aurand, J. Wagner, C. Lanning and K. Bjugstad, Building Biocompatible Hydrogels for Tissue Engineering of the Brain and Spinal Cord, J. Funct. Biomater., 2012, 3(4), 839–863.*

152. *C. Davoust, B. Plas, A. Béduer, B. Demain, A.-S. Salabert, J. C. Sol, et al., Regenerative potential of primary adult human neural stem cells on micropatterned bio-implants boosts motor recovery, Stem Cell Res. Ther., 2017, 8(1), 253.*

153. *10 J. T. S. Pettikiriarachchi, C. L. Parish, M. S. Shoichet, J. S. Forsythe and D. R. Nisbet, Biomaterials for brain tissue engineering, Aust. J. Chem., 2010, 63, 1143–1154.*

154. *Mahumane G.D., Kumar P., du Toit L C, Choonaraa Y.E. and Pillay V. .3D scaffolds for brain tissue regeneration: architectural challenges. Biomater. Sci., 2018,6, 2812-2837.*

155. *Ilya Levental a, Penelope C. Georges and Paul A. Janmey, Soft biological materials and their impact on cell function, Soft Matter, 2007, 3, 299-306.*

156. *Amit Gefen, Susan S Margulies, Are in vivo and in situ brain tissues mechanically similar? Journal of Biomechanics, Volume 37, Issue 9, 2004.*

157. *Nic D. Leipzig, Molly S. Shoichet, The effect of substrate stiffness on adult neural stem cell behavior, Biomaterials, Volume 30, Issue 36, 2009,*

158. *A.P. Balgude, X. Yu, A. Szymanski, R.V. Bellamkonda, Agarose gel stiffness determines rate of DRG neurite extension in 3D cultures, Biomaterials, Volume 22, Issue 10, 2001.*

159. *Kamali-Zare, P., Nicholson, C., 2013. Brain extracellular space: geometry, matrix and physiological importance. Basic Clin. Neurosci. 4, 282–286.*

160. Asakawa, N., Shimizu, T., Tsuda, Y., Sekiya, S., Sasagawa, T., Yamato, M., Fukai, F., Okano, T., 2010. Pre-vascularization of in vitro three-dimensional tissues created by cell sheet engineering. Biomaterials 31, 3903–3909.

161. Mealy, J.E., Chung, J.J., Jeong, H.-H., Issadore, D., Lee, D., Atluri, P., Burdick, J.A., 2018. Injectable granular hydrogels with multifunctional properties for biomedical applications. Adv. Mater. 30 e1705912.

162. Skop, N.B., Calderon, F., Cho, C.H., Gandhi, C.D., Levison, S.W., 2016. Optimizing a multifunctional microsphere scaffold to improve neural precursor cell transplantation for traumatic brain injury repair. J. Tissue Eng. Regen. Med. 10, E419–E432.

163. Chedly, J., Soares, S., Montembault, A., von Boxberg, Y., Veron-Ravaille, M., Mouffle, C., Benassy, M.-N., Taxi, J., David, L., Nothias, F., 2017. Physical chitosan microhydrogels as scaffolds for spinal cord injury restoration and axon regeneration. Biomaterials 138, 91–107.

164. Nih, L.R., Sideris, E., Carmichael, S.T., Segura, T., 2017. Injection of microporous annealing particle (MAP) hydrogels in the stroke cavity reduces gliosis and inflammation and promotes npc migration to the lesion. Adv. Mater. 29.

165. Kandalam, S., Sindji, L., Delcroix, G.J.-R., Violet, F., Garric, X., André, E.M., Schiller, P.C., Venier-Julienne, M.-C., des Rieux, A., Guicheux, J., Montero-Menei, C.N., 2017. Pharmacologically active microcarriers delivering BDNF within a hydrogel: novel strategy for human bone marrow-derived stem cells neural/neuronal differentiation guidance and therapeutic secretome enhancement. Acta Biomater. 49, 167–180.

166. Jgamadze, D., Liu, L., Vogler, S., Chu, L.-Y., Pautot, S., 2015. Thermo switching microgel carriers improve neuronal cell growth and cell release for cell transplantation. Tissue Eng. Part C Methods 21, 65–76.

167. *Smith, A.W., Segar, C.E., Nguyen, P.K., MacEwan, M.R., Efimov, I.R., Elbert, D.L., 2012. Long-term culture of HL-1 cardiomyocytes in modular poly (ethylene glycol) microsphere- based scaffolds crosslinked in the phase-separated state. Acta Biomater. 8,31–40.*

168. *Allazetta, S., Kolb, L., Zerbib, S., Bardy, J., Lutolf, M.P., 2015. Cell-instructive microgels with tailor-made physicochemical properties. Small 11, 5647–5656.*

169. *C. Chatelet, O. Damour, A. Domard, "Influence of the degree of acetylation on some biological properties of chitosan films" Biomaterials, 22 (2000), pp. 261-268.*

170. *N. Acosta, C. Jimenez, V. Borau, A. Heras "Extraction and characterization of chitin from crustaceans" Biomass Bioenergy, 5 (1993), pp. 145-153.*

171. *Christine Jérôm, Florence Croisier. "Chitosan-based biomaterials for tissue engineering". European Polymer Journal, April 2013: 780-792.*

172. *M. Dash, F. Chiellini, R.M. Ottenbrite, E. Chiellini, "Chitosan – a versatile semi-synthetic polymer in biomedical applications". Prog Polym Sci, 36 (2011), pp. 981-1014.*

173. *Kean T, Thanou M., "Chitin and chitosan: sources, production and medical applications." In: Williams PA, editor. Renewable resources for functional polymers and biomaterials. Polysaccharides, proteins and polyesters. 1st ed. London: Royal Society of, Chemistry; 2011. p. 292–318.*

174. *Q. He, et al., Preparation of chitosan films using different neutralizing solutions to improve endothelial cell compatibility, J. Mater. Sci. Mater. Med. 22 (12) (2011) 2791e2802.*

175. *Y. Yuana, B.M. Chesnutta, G. Utturkara, W.O. Haggarda, Y. Yangb, J.L. Ongb, J.D. Bumgardner; The effect of cross-linking of chitosan microspheres with genipin on protein release. Carbohydrate Polymers Volume 68, Issue 3, 5 April 2007.*

176. L.L. Bologna, et al., Investigating neuronal activity by SPYCODE multi-channel data analyzer, Neural Netw. 23 (6) (2010) 685e697.

177. A. Maccione, et al., A novel algorithm for precise identification of spikes in extracellularly recorded neuronal signals, J. Neurosci. Methods 177 (1) (2009) 241e249.

178. V. Pasquale, S. Martinoia, M. Chiappalone, A self-adapting approach for the detection of bursts and network bursts in neuronal cultures, J. Comput. Neurosci. 29 (1) (2010) 213e229.

179. Mealy, J.E., Chung, J.J., Jeong, H.-H., Issadore, D., Lee, D., Atluri, P., Burdick, J.A., 2018. Injectable granular hydrogels with multifunctional properties for biomedical applications. Adv. Mater. 30 e1705912.

180. Skop, N.B., Calderon, F., Cho, C.H., Gandhi, C.D., Levison, S.W., 2016. Optimizing a multifunctional microsphere scaffold to improve neural precursor cell transplantation for traumatic brain injury repair. J. Tissue Eng. Regen. Med. 10, E419–E432.

181. Chedly, J., Soares, S., Montembault, A., von Boxberg, Y., Veron-Ravaille, M., Mouffle, C., Benassy, M.-N., Taxi, J., David, L., Nothias, F., 2017. Physical chitosan microhydrogels as scaffolds for spinal cord injury restoration and axon regeneration. Biomaterials 138, 91–107.

182. Oliveira BF, Santana MHA, Ré MI (2005) Spray-dried chitosan microspheres cross-linked with d, l-glyceraldehyde as a potential drug delivery system: preparation and characterization. Braz J Chem Eng 22:353–360.

183. Torres MA, Vieira RS, Beppu MM, Arruda EJ, Santana CC (2007) Production of chemically modified chitosan microspheres by a spraying and coagulation method. Mater Res 10:347–352.

184. Dhawan S, Singla AK (2003) Nifedipine loaded chitosan microspheres prepared by emulsification phase-separation. Biotech Histochem 78:243–254.

185. *Akamatsu K, Kaneko D, Sugawara T, Kikuchi R, Nakao SI (2010) Three Preparation Methods for Monodispersed Chitosan Microspheres Using the Shirasu Porous Glass Membrane Emulsification Technique and Mechanisms of Microsphere Formation. Ind Eng.*

186. *Ribeiro AJ, Silva C, Ferreira D, Veiga F (2005) Chitosan-reinforced alginate microspheres obtained through the emulsification/internal gelation technique. Eur J Pharm Sci 25:31–40.*

187. *M. Frega, et al., Network dynamics of 3D engineered neuronal cultures: a new experimental model for in-vitro electrophysiology, Sci. Rep. 4 (2014) 5489.*

188. *G.M. Pharr, W.C. Oliver, F.R. Brotzen, On the generality of the relationship among contact stiffness, contact area, and elastic modulus during indentation, J. Mater. Res. 7 (3) (2011) 613e617.*

189. *E. Defranchi, et al., Imaging and elasticity measurements of the sarcolemma of fully differentiated skeletal muscle fibres, Microsc. Res. Tech. 67 (1) (2005) 27e35.*

190. *A.J. Engler, et al., Matrix elasticity directs stem cell lineage specification, Cell 126 (4) (2006) 677e689.*

191. *L.A. Flanagan, et al., Neurite branching on deformable substrates, Neuroreport 13 (18) (2002) 2411e2415.*

192. *A.L. Placone, et al., Human astrocytes develop physiological morphology and remain quiescent in a novel 3D matrix, Biomaterials 42 (2015) 134e143.*

193. *C.M. Valmikinathan, et al., Photocrosslinkable chitosan based hydrogels for neural tissue engineering, Soft Matter. 8 (6) (2012) 1964e1976.*

194. *Z. Cao, R.J. Gilbert, W. He, Simple agarose-chitosan gel composite system for enhanced neuronal growth in three dimensions, Biomacromolecules 10 (10) (2009) 2954e2959.*

195. *V.I. Scanga, et al., Biomaterials for neural-tissue engineering d chitosan supports the survival, migration, and differentiation of adult-derived neural stem and progenitor cells, Can. J. Chem. 88 (3) (2010) 277e287.*

196. *Dabiri, Seyed Mohammad Hossein, et al., New in-situ synthetized hydrogel composite based on alginate and brushite as a potential pH sensitive drug delivery system, Carbohydr. Polym. 177 (2017) 324e333.*

197. *Seung G. Lee, et al., Molecular dynamics simulation study of P (VP-co-HEMA) hydrogels: effect of water content on equilibrium structures and mechanical properties, Biomaterials 30.30 (2009) 6130e6141.*

198. *N. Garcia-Giralt, et al., Chitosan microparticles for "in vitro" 3D culture of human chondrocytes 3 (2013) 6362e6368.*

199. *T.B. Puschmann, et al., A novel method for three-dimensional culture of central nervous system neurons, Tissue Eng. Part C Methods 20 (6) (2014) 485e492.*

200. *P.M.D. Watson, et al., Bioengineered 3D glial cell culture systems and applications for neurodegeneration and neuroinflammation, SLAS Discov. 22 (5) (2017) 583e601.*

201. *I. Smith, et al., Neuronal-glial populations form functional networks in a biocompatible 3D scaffold, Neurosci. Lett. 609 (2015) 198e202.*

202. *S.J. Hollister, Porous scaffold design for tissue engineering, Nat. Mater 4 (2005) 518e524.*

203. *Cohen S, Bano MC, Cima LG et al (1993) Design of synthetic polymeric structures for cell transplantation and tissue engineering. Clin Mater 13:3–10.*

204. *Qasim S.B, Husain S, Huang Y, Pogorielov M, Deineka V., Lyndin M., Rawlinson A, Rehman I.U., In-vitro and in-vivo degradation studies of freeze gelated porous chitosan composite scaffolds for tissue engineering applications, Polymer Degradation and Stability, 2017.*

205. *Prerana Sensharma, G. Madhumathi, Rahul D. Jayant, Amit K. Jaiswal. Biomaterials and cells for neural tissue engineering: Current choices. Materials Science and Engineering C.*

206. *Dongwen Ren, Hongfu Yi, Wei Wang and Xiaojun Ma. The enzymatic degradation and swelling properties of chitosan matrices with different degrees of N-acetylation. Carbohydrate Research 340 (2005) 2403-2410.*

207. *Stephanie Knowlton, Yongku Cho, Xue-Jun Li, Ali Khademhosseini and Savas Tasoglu. Utilizing stem cells for three – dimensional neurale tissue engineering. Biomaterial Science – Royal Society of Chemistry.*

208. *Yong Kim, Seog-Jin Seo, Hyun-Seuk Moon, Mi-Kyong Yoo, In-Young Park, Bom-Chol Kim, Chong-Su Cho. Chitosan and its derivatives for tissue engineering applications. Biotechnology Advances 26 (2008) 1-21.*

209. *T. Kean, M. Thanou, Biodegradation, biodistribution and toxicity of chitosan, Advanced Drug Delivery Reviews, Volume 62, Issue 1, 2010.*

210. *Hua Zhang, Steven H. Neau, In vitro degradation of chitosan by a commercial enzyme preparation: effect of molecular weight and degree of deacetylation, Biomaterials, Volume 22, Issue 12, 2001.*

211. *Sophanit Mekasha, Hana Toupalová, Eka Linggadjaja, Harish A. Tolani, Ladislav Anděra, Magnus Ø. Arntzen, Gustav Vaaje-Kolstad, Vincent G.H. Eijsink, Jane W. Agger, A novel analytical method for d-glucosamine quantification and its application in the analysis of chitosan degradation by a minimal enzyme cocktail, Carbohydrate Research, Volume 433, 2016.*

212. *Gregor Tegl, Christoph Öhlknecht, Robert Vielnascher, Alexandra Rollett, Andreas Hofinger-Horvath, Paul Kosma, Georg M. Guebitz, Cellobiohydrolases Produce Different Oligosaccharides from Chitosan. Biomacromolecules 2016, 17, 6, 2284-2292.*

213. Pu Zheng, Jie Wang, Chan Lu, Yan Xu, Zhihao Sun, Immobilized β-glucosidase on magnetic chitosan microspheres for hydrolysis of straw cellulose, Process Biochemistry, Volume 48, Issue 4, 2013.

214. Ellinor B., Heggset, Anette I. Dybvik, Ingunn A. Hoell, Anne Line Norberg, Morten Sorlie, Vincent G. H. Eijsink, and ljell M. Varum. Degradation of Chitosan with a Family 46 Chitosanase from Streptomyces coelicolor. Biomacromolecules 2010, 11, 9, 2487-2497.

215. Ya-Li-Liu, Shu Jiang, Zu-Min Ke, Hai-Shui Wu, Cheng-Wu Chif, Zhan-Yu Guo. Recombinant expression of a chitosanase and its application in chitosan oligosaccharide production, Carbohydrate Research, Volume 344, Issue 6, 2009.

216. D. Somasheker & Richard Joseph. Chitosanases – properties and applcations: A review. Bioresource Technology, Volume 55, Issue 1, 1996.

217. Yuying Sun, Jiquan Zhang, Shengjun Wu, Shujun Wang. Praparation of D-glucosamine by hydrolysis of chitosan with chitosanase and β-D-glucosaminidase. International Journal of Biological Macromolecules, Volume 61, 2013.

218. Pascal Viens, Marie-Eve Lacombe_Harvey and Ryszard Brzezinski. Chitosanases from Family 46 of Glycoside Hydrolases: From Proteins to Phenotypes. Mar. Drugs 2015, 13(11), 6566-6587.

219. Nidheesh Thadthil, Suresh Puthanveetil Velappan. Recent developments in chitosanase research and its biotechnological applications: A review. Food Chemistry, Volume 150, 2014.

220. Shijia Liu, Shangjin Shao, Linlin Li, Zhi Cheng, Peji Gao, Lushan Wang. Substrate-binding specific of chitinase and chitosanase as revealed by active-site architecture analysis. Carbohydrate Research, Volume 418, 2015.

221. Shoko Shinya, Tamo Fukamizo. Interaction between chitosan and its related enzymes: A review. International Journal of Biological Macromolecules, Volume 104, Part B,2017.

222. Ellinor B. Heggset, Tina R. Tuveng, Ingunn A. Hoell, Zhanliang Liu, Vincent G. H. Eijsink and Kjell M. Varum. Mode of Action of a Family 75 Chitosanase from Streptomyces avermitilis. Biomacromolecules 2012, 13, 6, 1733-1741

223. Steffen Luck, René Schubel, Jannick Rub, Dominik Hahn, Evelien Mathieu, Heike Zimmermann, Dieter Scharnweber, Carsten Werner, Sophie Pautot, Rainer Jordan. Teilored and biodegradable poly(2-oxazoline) microbeads as 3D marices for stem cell culture in regenerative therapies. Biomaterials, Volume 79,2016.

224. Madze D, Bergen J, Stone D, Jang J-H, Schaffer DV, Isacoff EY, et al. (2012) Colloids as Mobile Substrates for the Implantation and Integration of Differentiated Neurons into the Mammalian Brain. PLoS ONE 7(1): e30293.

225. Sideris, E.; Griffin, D. R.; Ding, Y.; Li, S.; Weaver, W. M.; Di Carlo, D.; Hsiai, T.; Segura, T. Particle Hydrogels Based on Hyaluronic Acid Building Blocks. ACS Biomater. Sci. Eng. 2016, 2 (11), 2034−2041.

226. Sheikhi, A.; de Rutte, J.; Haghniaz, R.; Akouissi, O.; Sohrabi, A.; Di Carlo, D.; Khademhosseini, A. Microfluidic-Enabled Bottom-up Hydrogels from Annealable Naturally-Derived Protein Microbeads. Biomaterials 2019, 192, 560−568.

227. Mealy, J. E.; Chung, J. J.; Jeong, H. H.; Issadore, D.; Lee, D.; Atluri, P.; Burdick, J. A. Injectable Granular Hydrogels with Multifunctional Properties for Biomedical Applications. Adv. Mater. 2018, 30 (20), 1−7.

228. de Rutte, J. M.; Koh, J.; Di Carlo, D. Scalable High-Throughput Production of Modular Microgels for in Situ Assembly of Microporous Tissue Scaffolds. Adv. Funct. Mater. 2019, 1900071.

229. Griffin, D. R.; Weaver, W. M.; Scumpia, P. O.; Di Carlo, D.; Segura, T. Accelerated Wound Healing by Injectable Microporous Gel Scaffolds Assembled from Annealed Building Blocks. Nat. Mater. 2015, 14 (7), 737−744.

230. Nih, L. R.; Sideris, E.; Carmichael, S. T.; Segura, T. Injection of Microporous Annealing Particle (MAP) Hydrogels in the Stroke Cavity Reduces Gliosis and Inflammation and Promotes NPC Migration to the Lesion. Adv. Mater. 2017, 29 (32), 1606471.

231. Floyd, A. G. Top Ten Considerations in the Development of Parenteral Emulsions. Pharm. Sci. Technol. Today 1999, 2 (4), 134− 143.

232. Ganta, S.; Talekar, M.; Singh, A.; Coleman, T. P.; Amiji, M. M. Nanoemulsions in Translational Research Opportunities and Challenges in Targeted Cancer Therapy. AAPS PharmSciTech 2014, 15 (3), 694−708.

233. Deshmukh, R.; Wagh, P.; Naik, J. Solvent Evaporation and Spray Drying Technique for Micro- and Nanospheres/Particles Preparation: A Review. Drying Technol. 2016, 34 (15), 1758−1772.

234. (22) do Vale Morais, A. R.; do Nascimento Alencar, É.; Júnior, F. H. X.; de Oliveira, C. M.; Marcelino, H. R.; Barratt, G.; Fessi, H.; do Egito, E. S. T.; Elaissari, A. Freeze-Drying of Emulsified Systems: A Review. Int. J. Pharm. 2016, 503 (1−2), 102−114.

235. Kasper, J. C.; Winter, G.; Friess, W. Recent Advances and Further Challenges in Lyophilization. Eur. J. Pharm. Biopharm. 2013, 85 (2), 162−169.

236. Zhang, C.; Feng, F.; Zhang, H. Emulsion Electrospinning: Fundamentals, Food Applications and Prospects. Trends Food Sci. Technol. 2018, 80, 175−186.

237. *Gómez-Mascaraque, L. G.; López-Rubio, A. Protein-Based Emulsion Electrosprayed Micro- and Submicroparticles for the Encapsulation and Stabilization of Thermosensitive Hydrophobic Bioactives. J. Colloid Interface Sci. 2016, 465, 259−270.*

238. *Lee, M. K.; Kim, M. Y.; Kim, S.; Lee, J. Cryoprotectants for Freeze Drying of Drug Nano-Suspensions: Effect of Freezing Rate. J. Pharm. Sci. 2009, 98 (12), 4808−4817.*

239. *Guha, I. F.; Varanasi, K. K. Separating Nanoscale Emulsions: Progress and Challenges to Date. Curr. Opin. Colloid Interface Sci. 2018, 36, 110−117.*

240. *T. Kawakatsu, Y. Kikuchi, M. Nakajima, Regular-sized cell creation in microchannel emulsification by visual microprocessing method, J. Am. Oil Chem. Soc. 74 (1997) 317–321.*

241. *E. Amstad, M. Chemama, M. Eggersdorfer, L.R. Arriaga, M.P. Brenner, D.A. Weitz, Robust scalable high throughput production of monodisperse drops, Lab Chip. 16 (2016) 4163–4172.*

242. *S. Sugiura, M. Nakajima, S. Iwamoto, M. Seki, Interfacial tension driven monodispersed droplet formation from microfabricated channel array, Langmuir. 17 (2001) 5562–5566.*

243. *J.M. de Rutte, J. Koh, D. Di Carlo, Scalable high-throughput production of modular microgels for in situ assembly of microporous tissue scaffolds, Submitted. (2019).*

244. *S.F. Wong, J.S. Lim, S.S. Dol, Crude oil emulsion: a review on formation, classification and stability of water-in-oil emulsions, J. Pet. Sci. Eng. 135 (2015) 498–504.*

245. *D.J. McClements, Food emulsions: principles, practices, and techniques, CRC press, 2015.*

246. *L. Mao, Y.H. Roos, C.G. Biliaderis, S. Miao, Food emulsions as delivery systems for flavor compounds: A review, Crit. Rev. Food Sci. Nutr. 57 (2017) 3173–3187*

List of Publications

- *Microengineered Emulsion-to-Powder Technology for the High-Fidelity Preservation of Molecular, Colloidal, and Bulk Properties of Hydrogel Suspensions.* Sheikhi A, **Di Lisa D**, de Rutte J, Akouissi O, Di Carlo D, Khademhosseini A. ACS Applied Polymer Materials. 2019 July 5; 10.1021/acsapm.9b00265

- *Soft chitosan microbeads scaffold for 3D functional neuronal networks.* Tedesco MT*, **Di Lisa** D*, Massobrio P, Colistra N, Pesce M, Catelani T, Dellacasa E, Raiteri R, Martinoia S, Pastorino L. Biomaterials. 2017 Nov 28; 156:159-171

- *Coherent X-ray diffraction imaging of nanoengineered polymeric capsule.* S. Erokhina, L. Pastorino, **D. Di Lisa**, A. G. Kiiamov, A. R. Faizullina, D. A. Tayurskii, S. Iannotta, V. Erokhin. Jetp Lett. (2017*).*

Poster presentations

- Poster presentation: **Di Lisa D**, Tedesco MT, Massobrio P, Colistra N, Pesce M, Catelani T, Dellacasa E, Raiteri R, Martinoia S, Pastorino. *Chitosan biopolymer: alternative adhesion factor and scaffold matrix for 2D and 3D neuronal cultures*. 2nd Centro 3R Annual Meeting, 3Rs in Italian University, June 20-21 2019, Genova, Italy.

- Poster presentation: **Di Lisa D**, Tedesco MT, Massobrio P, Colistra N, Pesce M, Catelani T, Dellacasa E, Raiteri R, Martinoia S, Pastorino. *A novel in vitro model of neuronal cultures based on 3D chitosan scaffold*. EUSAAT 2018, 21st European Congress on Alternatives to Animal Testing & 18th Annual Congress of EUSAAT, Linz September 23-26, 2018

- Poster Presentation: **Di Lisa D**, Tedesco MT, Massobrio P, Colistra N, Pesce M, Catelani T, Dellacasa E, Raiteri R, Martinoia S, Pastorino. *Biomimetic 3D scaffold for neuronal culture*. First Annual Meeting, COST Action CA16119 CellFit, "In vitro 3D- total cell guidance and fitness, Albena Resort, Varna.

Talk

- Oral presentation: *Three-dimensional scaffold based on chitosan microbeads for 3D neuronal culture*. GNB 2018 - VI National Congress of Bioengineering. June 27nd 2018, Milan, Italy

Patent

- "*Procedimento per il trattamento delle superfici di supporti o contenitori per colture neuronali bidimensionali mediante chitosano quale fattore di adesione cellulare"*

Award

- November 2018 – StartCup competition organised by Università degli Studi di Genova.